

Diss. ETH No. 19181

Metallic and Mott-insulating phases  
in fermionic quantum gases

A dissertation submitted to the  
ETH Zürich

for the degree of  
Doctor of Sciences

presented by

Robert Jördens

Dipl. Phys. ETH  
born 8. December 1981  
Germany

accepted on the recommendation of  
Prof. Dr. Tilman Esslinger, examiner  
Prof. Dr. Frédéric Merkt, co-examiner

2010

To my family.

## *Zusammenfassung*

In der hier vorgelegten Arbeit wird über Experimente berichtet, in denen mit ultrakalten fermionischen Atomen in optischen Gittern das Hubbardmodell erforscht wird.

Die Kontrolle der Modellparameter, insbesondere der Tunnelstärke und der Wechselwirkung, eröffnet den Zugang zum Regime starker Korrelationen. Hier kommt es infolge der abstossenden Wechselwirkung zum Übergang vom Metall zum Isolator. Das Mott-isolierende Verhalten des Kerns der Wolke kann anhand dreier Merkmale identifiziert werden: die Doppelbesetzung von Gitterplätzen ist stark unterdrückt, der Kern wird zunehmend inkompressibel, und es bildet sich eine charakteristische Mode aus, die der Anregung von Doppelbesetzungen mit wohldefinierter Energie entspricht.

Durch den Vergleich präziser Messungen der Doppelbesetzung mit numerischen Resultaten über einen grossen Bereich verschieden starker Wechselwirkung und Gitterfüllung kann ein Mass für die Entropie des Systems im Gitter entwickelt werden. Sowohl die Hochtemperaturentwicklung des Hamilton-Operators, wie auch die dynamische Molekularfeldtheorie (DMFT) stimmen mit den experimentellen Beobachtungen überein. Der Einfluss systematischer Fehler auf die beobachtete Entropie kann mittels einer umfassenden Analyse der Kalibration der Modellparameter eingegrenzt werden. Im Mott-isolierenden Zentrum der Wolke beträgt die Entropie pro Teilchen das Doppelte der kritischen Entropie in der antiferromagnetischen Phase.

Die niedrige Temperatur ultrakalter Quantengase macht die intrinsischen Energieskalen experimentell zugänglich und ermöglicht es, dynamische Prozesse zu untersuchen. Da die Bewegung der atomaren Wolke nach einer Auslenkung zeitlich aufgelöst werden kann, liefert sie Einblicke in das Verhalten auf der Skala der kinetischen Energie und Aufschluss über die Transporteigenschaften. Während nicht-wechselwirkende Wolken schwach gedämpft in der Falle schwingen, wird diese Oszillation mit zunehmender Anziehung zwischen den Atomen durch die Bildung lokalisierter Paare unterdrückt. Aufgrund der stark reduzierten Tunnelrate dieser Paare wird aus der Schwingung eine langsame, relaxationsartige Driftbewegung. Die Modifikation der Wechselwirkung in Echtzeit während der Evolution erlaubt die dynamische Kontrolle des Transportverhaltens.

Anhand von Doppelbesetzungen mit Wechselwirkungsenergien, die weit höher sind als die Bewegungsenergie, wird der Zerfall hochenergetische Anregungen untersucht. Die durch Gittermodulation induzierten Doppelbesetzungen

gen zerfallen auf Zeitskalen, die über mehrere Größenordnungen variieren und stark von der Tunnelrate und Wechselwirkung abhängen. In Einheiten der Tunnelzeit skaliert die Lebensdauer exponentiell mit dem Verhältnis von Wechselwirkungsenergie zu Bandbreite. Der Zerfallsprozess wird von simultanen Vielkörperstößen höherer Ordnung mit einzelnen Fermionen dominiert.

## *Abstract*

In this thesis the Hubbard model is explored with ultracold fermionic atoms in an optical lattice.

Access to the strongly correlated regime of repulsive interaction and the metal-insulator transition is gained by exploiting the control over tunneling and interaction energy. The emergence of a Mott-insulating core is identified by three features: the strong suppression of doubly occupied lattice sites, a vanishing core compressibility, and the emergence of an excitation mode at the on-site interaction energy corresponding to the creation of double occupancies.

The entropy of the system is determined by comparing accurate measurements of the equilibrium double occupancy with theoretical calculations over a wide range of parameters. Both, the high-temperature series expansion of the Hubbard model and dynamical mean-field theory, are in quantitative agreement with the experimental data. A comprehensive analysis of all systematic errors confirms the reliability of the entropy determination. In the Mott-insulating center of the atomic cloud we obtain an entropy per atom which is about twice as large as the critical entropy of the antiferromagnetic phase.

The small energy scales in quantum gases make the intrinsic dynamics experimentally accessible. The kinetic energy scale and the mass transport properties are explored by resolving the center of mass motion of the atoms after displacement. With increasingly strong attractive interactions the weakly damped oscillations, most pronounced for the half-filled non-interacting case, turn into a slow relaxational drift due to the formation of localized pairs with a reduced tunneling rate. By tuning the interaction strength during the evolution, the transport behavior can be controlled dynamically.

To access the regime of high energy excitations, double occupancies with a repulsive interaction energy much larger than the kinetic energy are studied. In the equilibrium state of suppressed double occupancy, additional excitations are created by lattice modulation and their subsequent decay is monitored over time. The measured absolute lifetime of double occupancies covers two orders of magnitude and in units of the tunneling time it is found to depend exponentially on the ratio of on-site interaction energy to kinetic energy. The dominant mechanism for the relaxation is a simultaneous many-body process involving several single fermions as scattering partners.



## *Contents*

<i>1</i>	<i>Introduction</i>	<i>1</i>
<i>2</i>	<i>A brief introduction to the Hubbard model</i>	<i>7</i>
<i>3</i>	<i>Constructing the Hubbard model for fermionic atoms</i>	<i>13</i>
<i>4</i>	<i>The experimental apparatus</i>	<i>53</i>
<i>5</i>	<i>Exploring the Mott insulator</i>	<i>73</i>
<i>6</i>	<i>Approaching quantum magnetism</i>	<i>85</i>
<i>7</i>	<i>Controlling transport by interaction</i>	<i>97</i>
<i>8</i>	<i>Observing elastic doublon decay</i>	<i>107</i>
<i>9</i>	<i>Outlook</i>	<i>119</i>
	<i>Bibliography</i>	<i>123</i>
	<i>Acknowledgments</i>	<i>140</i>
	<i>Curriculum vitæ</i>	<i>143</i>





## 1 Introduction

New solid materials with intriguing mechanical, electrical, optical, and thermodynamical properties are at the center of many important advances in technology. However, the understanding of their macroscopic features is a challenge since they emerge as a result of complex quantum many-body behavior at the microscopic scale. For example, several physical principles govern the movement and the interaction of electrons in matter and their combination leads to distinct material classes such as insulators, semiconductors, metals, and superconductors.

Solid state physics has succeeded in extracting the fundamental physical principles responsible for many of these effects. The principles have then been incorporated into models that provide insight into the workings of the interaction in electron gases in the context of Fermi liquid theory [1] or the Bardeen-Cooper-Schrieffer mechanism of low temperature superconductivity [2], for example. Many solid state models, however, are exceedingly hard to analyze due to the large number of particles involved. Despite reducing the description to a small subset of physical effects, these simple models frequently pose big challenges and can not even be treated numerically.

Experiments with ultracold atoms can approach the framework of solid state theory from a different angle. In 1998 a conceptual link was established [3] between atoms in an optical lattice and a solid state model for interacting bosonic particles on a crystalline surface [4]. It is now clear that several important model Hamiltonians can in principle be realized accurately using optical lattices and alkali atoms [5]. Answers to long-standing questions of solid state physics can hence be found experimentally. This approach has been termed *quantum simulation* [6, 7].

An important candidate among these conceptually simple but numerically challenging models is the one proposed by J. Hubbard in 1963 for the behavior of electrons in certain types of solids. It interpolates between two other approximative models: the free gas description for weakly interacting electrons in wide energy bands on one hand and the fully atomistic description of strongly correlated and thus localized electrons on the other hand. Hubbard's approach connects "the ordinary band model and the atomic model" [8] in a "highly oversimplified" [9] way. His choice to include just two processes is one of the simplest treatments of the peculiar interplay of kinetic and interaction energy in interacting fermions on a lattice, as outlined in chapter 2.

Despite the apparent simplicity the Hubbard model acquires broad applicability as well as a peculiar complexity. It encompasses the physics of models like the Heisenberg or the  $t$ - $J$  Hamiltonian which emerge as its limiting cases. The Hubbard model is also widely considered a promising contender to capture the fundamentals of high temperature superconductivity [10], an effect that was discovered more than 20 years ago in the cuprates [11]. The advocacy of this position is manifest [12] as is the condensed matter community's tendency to declare a lack of consensus and to "justify ... yet another implausible conjecture as to some aspect of the phenomenon" [13].

While already Hubbard's paper offers several approaches to shed light on limiting cases of his model, almost 50 years of intense research by significant parts of the condensed matter community leave many questions unanswered [14]. The nature of the ground-state of the two- and three-dimensional Hubbard model remains elusive — even on a qualitative level.

While theoretical physics struggles to implement and understand the Hubbard model using numeric and analytic methods, important progress has been made with ultracold atoms. A landmark result was the observation of the superfluid to Mott insulator transition using bosonic atoms trapped in an optical lattice [15]. Yet it is the fermionic character combined with repulsive interactions which provides the fundamental link to the questions in strongly correlated electron systems.

Ultracold atoms can be manipulated and trapped using light forces. This effect has led to the realization of the periodic potential of a crystalline lattice using the interference pattern of laser beams. Due to the small temperatures, the atoms can be loaded into the lowest energy band of such an optical lattice. Exploiting the external control over the intensity of the beams, the tunneling rate between the sites can be tuned. Moreover, the back-action of the atoms on the light potential is negligible and the lattice does not source or sink energy as is the case in many solid materials. This decoupling of lattice and atomic degrees of freedom is a prerequisite of the Hubbard model where a static lattice is assumed.

Collisions among the atoms in ultracold quantum gases provide the tools to implement an analog to the Coulomb repulsion between electrons. Often, the scattering can be treated as a contact interaction potential. Such a  $\delta$ -shaped tunable interaction is the optimal tool to simulate the on-site interaction of electrons in a lattice as it has the shortest possible range and hence reduces parasitic off-site interactions which are not part of the Hubbard model. Feshbach resonances, which are controlled via the magnetic field, give access to the regimes of attractive, vanishing, or repulsive interactions. Combining the physics of optical lattices and Feshbach resonances, the Hubbard Hamiltonian can be constructed for fermionic atoms with tunable parameters that are derived from microscopic principles, as detailed in chapter 3.

Within the context of the three-dimensional Fermi-Hubbard model, research has so far focused on the non-interacting and attractively interacting cases [16, 17, 18, 19]. Other experimental studies of the equilibrium properties have been concerned with exotic non-Hubbard effects such as the influence of reduced dimensionality [20, 21],  $p$ -wave scattering [22], mixtures of bosonic and fermionic atoms [23, 24, 25, 26], or physics beyond the single-band description [27]. The observation of the strongly correlated phases in the regime of repulsive interactions, which provide the link to electron systems, was an unresolved challenge.

In order to gain access to the repulsive Fermi-Hubbard model and to perform quantitative experimental simulations, probes have to be developed, that signal the state of the system in the lattice. Measures for the density, that are sensitive to fluctuations or thermal excitations, or a scheme to determine the temperature in the lattice, for example, could not be demonstrated so far. Furthermore, samples of ultracold quantum gases are confined in a trap in contrast to homogeneous systems. This leads to a coexistence of different phases and requires observables that can distinguish among them. Additionally, the parameters of the model need to be calibrated independently and with sufficient accuracy to facilitate comparison with theoretical predictions.

In this thesis we implement the repulsive Hubbard model with ultracold fermionic Potassium atoms in a three-dimensional optical lattice and study its metallic and insulating phases both in equilibrium and out-of-equilibrium. The properties of the apparatus and some experimental techniques are reviewed in chapter 4. The work presented in this thesis was carried out in collaboration with Niels Strohmaier, Kenneth Günter, Daniel Greif, Thomas Uehlinger, Yosuke Takasu, Michael Köhl, Leticia Tarruell, and Henning Moritz.

In chapter 5 we report on the first observation of the characteristic signature of strong correlations, the Mott-insulating phase, where insulating behavior and incompressibility emerge not as a result of a filled lattice but rather due to localization by repulsion. The direct control of the interaction strength allows comparing the Mott-insulating and the non-interacting regime without changing other parameters such as filling or tunneling energy. The double occupation of lattice sites is identified as a characteristic excitation in the Mott-insulating phase and used to develop a measure for the compressibility of a trapped inhomogeneous system that is insensitive to the influence of metallic edges.

In order to investigate the role of the harmonic confinement on the nature of thermal excitations, the two regimes of thermal creation and thermal dissociation of double occupancies are identified in chapter 6. While the former is a natural consequence of large repulsive interaction in a homogeneous system, the later is unique to a trapped system. Here, the combination of the density of states in the trap and the resulting temperature behavior of the chemical potential favors the depletion of doubly occupied states despite the associated release of repulsive interaction energy.

By developing and implementing improved calibration methods, the model parameters can be determined with an accuracy that is suitable for quantitative comparison with theoretical models. The calibration of the interaction strength leads to an improvement in the knowledge of the Feshbach resonance parameters. Since mutually independent methods are employed for calibration, they permit a comprehensive error analysis and yield systematic bounds for the experimental observables and the derived quantities. By combining measurements of the double occupancy in a wide range of interaction strengths and fillings with two different *ab initio* numerical methods, a novel measure for the entropy and the temperature in the lattice is developed. This determination of temperature and Hubbard parameters leads to the first quantitative simulation of the repulsive Fermi-Hubbard model with ultracold atoms and provides insight into the microscopic properties of the system. In particular, the unequal entropy distribution in the trap and the intriguing buffering effect of low density metallic shells can be identified.

Current experiments intend to decrease the temperature in the lattice to observe the antiferromagnetically (AFM) ordered phase which is considered the next step towards quantum simulation of the Hubbard model. The AFM emerges below the Néel temperature where virtual tunneling mediates a Heisenberg-like spin interaction between neighboring sites and leads to long-range order with alternating magnetization. The results presented in chapter 6 determine the position of the present experimental parameters in the phase diagram. In order to locate the antiferromagnetic phase boundary, new numerical data on the critical temperature and entropy at the point of optimal interaction are supplied. Combining the current experimental parameters with the data of the critical point, a measure of the proximity to quantum magnetism is provided showing that the local entropy in the lattice is a factor of two above the critical entropy.

In the second group of experiments we leave behind the regime of thermal equilibrium and observe the dynamics of mass transport and high-energy excitations. The study of charge transport and excitations in electronic systems has received much attention in solid state physics as it determines the conductive behavior and many electronic properties of the material. For example, the metal-insulator phase transition could be triggered using femtosecond electromagnetic pulses and its ultrafast dynamics could be resolved [28]. In cold atom experiments, the small energies associated with the low temperature lead to a reduction of the intrinsic timescales and a slow-down of the dynamics compared to solid matter. As a result, the parameters can be altered or quenched at a high rate. This opens up the possibility of exploring “ultrafast” physics where excitations are created and monitored quasi-instantaneously.

While previous studies of the dynamics of fermionic atoms in optical lattices have focused on one-dimensional geometries [29, 30], the transport properties

of an interacting Fermi gas in the three-dimensional optical lattice are explored in chapter 7. The center of mass dynamics of the atoms after a sudden displacement of the trap minimum is monitored for different interaction strengths and lattice fillings. While dipole oscillations are observed for a non-interacting cloud, the different effective masses in the optical lattice and the localized states in the trap perimeter lead to a rapid dephasing even in the absence of collisions. With increasingly strong attractive interactions the damped oscillations turn into a slow relaxational drift due to the formation of localized pairs with a strongly reduced pair tunneling rate. Tuning the interaction strength during the evolution allows us to dynamically control the transport behavior and to switch between oscillatory and drift motion.

In the experiments described in chapter 8, the large range of the Hubbard parameters and the good time resolution are used to investigate the decay of highly excited states in the Fermi-Hubbard model. Starting in the equilibrium state of a repulsively interacting system, double occupancies are induced quasi-instantaneously and their lifetime is determined. It varies over two orders of magnitude and exhibits a strong dependence on both kinetic and interaction energy. In order to derive a universal scaling, we scan tunneling and interaction and show that the lifetime scales exponentially with the ratio of on-site repulsion to kinetic energy. The interpretation in terms of virtual many-body scattering with single fermions is corroborated by a diagrammatic analysis that confirms the observed scaling exponent.

The dynamics of excitations in optical lattices are important for the understanding of the preparation of states with ultracold atoms. If a change in parameters requires the decay of excitations or mass transport, the rate of change must be reduced to prevent heating. The results presented here impose limits on the speed of adiabatic parameter sweeps.

The results pave the way for further studies of the Mott insulator and the crossover between insulating and metallic behavior, including spin ordering and, ultimately, the question of *d*-wave superfluidity [5, 31]. Future avenues in the exploration of new many-body Hamiltonians can be found by adapting experimental methods developed in atom physics that are conceptually orthogonal to traditional solid state experiments. The detailed control over the lattice potential should allow the study of mesoscopic lattice systems and the crossover between exactly solvable quantum systems of a few sites and large systems in the thermodynamic limit. A further promising field are polar molecules in Hubbard-like systems [32, 33] where long-range interactions can lead to supersolid behavior.



## 2 A brief introduction to the Hubbard model

### The Hamiltonian

The Hubbard model includes just three fundamental processes that govern the behavior of the electrons: they move, they interact, and they have a fermionic spin.

$$H_{\text{FH}} = -t \sum_{\sigma, \langle ij \rangle} c_{i\sigma}^\dagger c_{j\sigma} + U \sum_i n_{i\uparrow} n_{i\downarrow}. \quad (2.1)$$

The Hamiltonian is a sum of the tunneling term that drives the hopping of fermions between neighboring sites  $\langle ij \rangle$  with an amplitude  $t$  and the interaction term with an on-site energy  $U$ . Figure 2.1 sketches these processes. The operators  $c_{i\sigma}$  and  $c_{i\sigma}^\dagger$  act on the occupation basis with site index  $i$  and spin  $\sigma = \uparrow, \downarrow$ . They obey the fermionic commutation rules,  $[c_{i\sigma}^\dagger, c_{j\sigma'}] = \delta_{ij} \delta_{\sigma\sigma'}$  and  $[c_{i\sigma}^\dagger, c_{j\sigma'}^\dagger] = [c_{i\sigma}, c_{j\sigma'}] = 0$ .

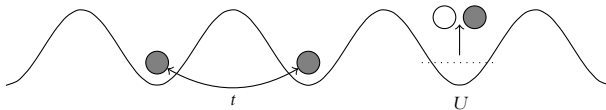


Figure 2.1: Sketch of the quantum mechanical processes described by the Hubbard Hamiltonian. The tunneling term drives hopping between neighboring sites with an amplitude  $t$  and corresponds to the kinetic energy that delocalizes the particles over the lattice. The on-site repulsion  $U$  counteracts the delocalization and favors non-overlapping wavefunctions that are localized on individual lattice sites.

### The double well

Already the analysis of the smallest non-trivial problem, a system of two sites, is sufficient to derive the basic physics contained in the Hubbard model such as bandwidth, double occupancy, and antiferromagnetism. The problem is analogous to the electron configurations of the Hydrogen molecule [34, 35].

As the Hamiltonian conserves the overall particle number per spin it can be solved separately on each subspace of a given total number of spin-ups and spin-downs. Four of the 16 states that comprise the complete Hilbert space, belong

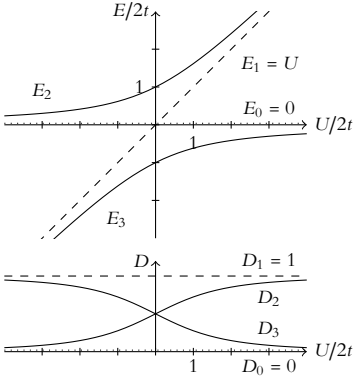


Figure 2.2: Eigenenergies and double occupancy in the half-filled two-site Hubbard model. The four eigenstates are: the delocalized singly occupied triplet  $E_0 = 0$ ,  $D_0 = 0$  (dotted), the doubly occupied singlet  $E_1 = U$ ,  $D_1 = 1$  (dashed), and the mixed singlet  $E_{2,3}$ ,  $D_{2,3}$  (solid curves).

to the sector with one spin-up and one spin-down fermion:  $|\uparrow\downarrow, 0\rangle$ ,  $|\uparrow, \downarrow\rangle$ ,  $|\downarrow, \uparrow\rangle$ , and  $|0, \uparrow\downarrow\rangle$ . The Hamiltonian in matrix form restricted to this subspace is:

$$H_{\text{FH}} = \begin{pmatrix} U & -t & -t & 0 \\ -t & 0 & 0 & -t \\ -t & 0 & 0 & -t \\ 0 & -t & -t & U \end{pmatrix}. \quad (2.2)$$

The eigenvalues (also depicted in Figure 2.2) and eigenvectors are:

- $E_0 = 0$  for the singly occupied spin triplet  $|\uparrow, \downarrow\rangle - |\downarrow, \uparrow\rangle$ ,
- $E_1 = U$  for the spin singlet superposition of the two doubly occupied states  $|\uparrow\downarrow, 0\rangle - |0, \uparrow\downarrow\rangle$ , and
- $E_{2,3} = U/2 \pm \sqrt{(U/2)^2 + (2t)^2}$  for the two other singlets that mix the two different occupancies,

$$2t(|\uparrow\downarrow, 0\rangle + |0, \uparrow\downarrow\rangle) + (U/2 \mp \sqrt{(U/2)^2 + (2t)^2})(|\uparrow, \downarrow\rangle + |\downarrow, \uparrow\rangle).$$

The normalization prefactors of the different eigenvectors have been omitted for brevity. The terms singlet and triplet refer to the symmetry of the spin wavefunction.

For vanishing interactions,  $U = 0$ , the last two states reproduce the bandwidth  $4t$  of the Bloch band in the corresponding infinite system. Each Fermion is symmetrically or antisymmetrically delocalized over the lattice. corresponding



to minimal or maximal momentum. The probability of finding a site doubly occupied in these two states is

$$D_{2,3} = \frac{1}{1 + \left( U/4t \pm \sqrt{(U/4t)^2 + 1} \right)^2}. \quad (2.3)$$

The energetically lower one of the two states is the ground state. For large negative  $U$  it is highly doubly occupied with energy  $U - 4t^2/U$ . For strong repulsion and large positive  $U$  it is a localized antiferromagnetic singlet. Its eigenenergy  $-4t^2/U < 0$  reveals the energy scale of the Heisenberg exchange interaction. It is a characteristic quantity for the antiferromagnetically ordered ground state of the positive- $U$  infinite Hubbard model at half filling.

The two triplet eigenstates of the spin-polarized ferromagnetic occupation manifolds  $|\uparrow, \uparrow\rangle$  and  $|\downarrow, \downarrow\rangle$  have zero energy and are thus disfavored against the antiferromagnetic singlet state which has a strictly negative energy.

Such a detailed analytic treatment of the generic Hubbard model without the use of approximations is limited to a handful of particles and sites. Already for four sites, the basis contains the  $4^4 = 256$  elements shown in Figure 2.3. The commonly available computational power limits the maximum size of a system to about four-by-four sites for exact diagonalization. Here the basis already contains more than a billion elements.

### *The phase diagram*

A rough sketch of the alleged phases in the three-dimensional Hubbard model with repulsive interactions is presented in Figure 2.4 and discussed in the following. The other side of the phase diagram where the particles interact attractively is known to contain superfluid BCS-like phases. These are reviewed in [36].

The regime of antiferromagnetism has been described most accurately with quantum Monte-Carlo (QMC) [37, 38] and dynamical mean field theoretical (DMFT) methods [39]. Antiferromagnetic behavior relies on both strong hopping and strong correlations and emerges when bandwidth and interaction are of comparable size. Correctly predicting the phase boundary in a numerical analysis is considered a benchmark problem due to the difficulty of treating both parts of the Hamiltonian correctly and simultaneously. While the antiferromagnetic phase boundary is the only quantity that can be considered known to a certain extent, the question as to whether a phase transition between the Fermi liquid and Mott insulator is masked by the Antiferromagnet remains unanswered. Such a phase transition could be observed if magnetism is explicitly excluded by geometric frustration.

The situation becomes even more complex away from half filling when the particle-hole symmetry is broken by doping the system. Evidence indicates the

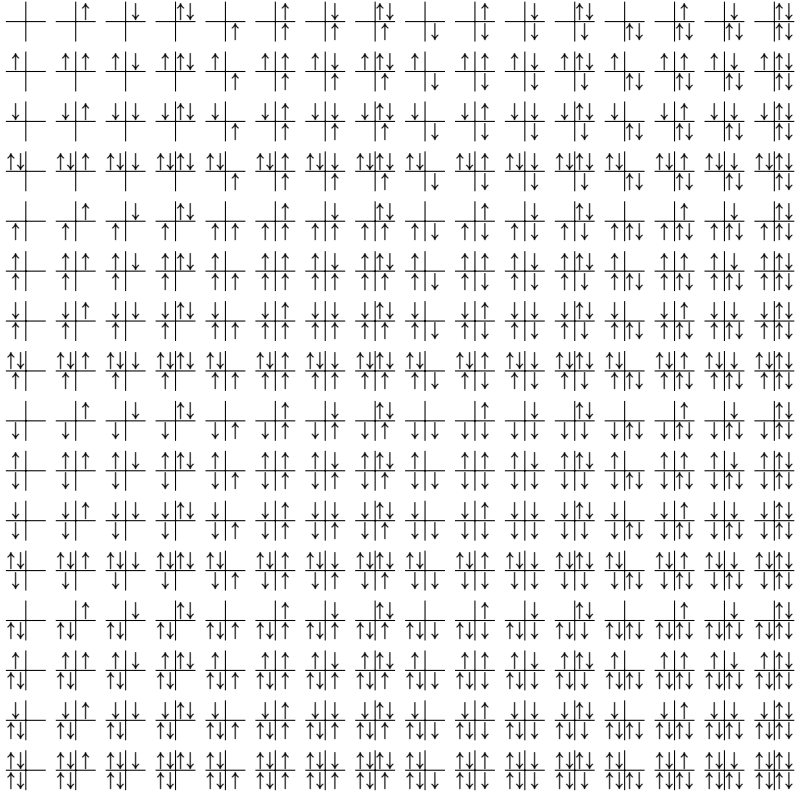


Figure 2.3: The basis states of the four-site Hubbard model. On a two-by-two square plaquette each of the four sites has four possible occupations: empty, spin up  $\uparrow$ , spin down  $\downarrow$ , and doubly occupied  $\uparrow\downarrow$ . The Hilbert space is spanned by these  $4^4 = 256$  configurations.

possibility that at some doping the system could develop a ground state with a  $d$ -wave symmetric wavefunction [40] and superfluid behavior.

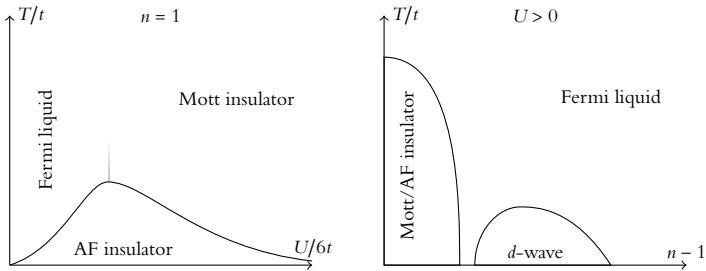


Figure 2.4: Schematic phase diagram of the Hubbard model. In the interaction-temperature plane (left) and in the doping-temperature plane (right) the different widely postulated and expected phases of the three dimensional Hubbard model can be identified. The antiferromagnetic phase boundary at  $n = 1$  in the  $T/U$  plane has only recently been explored numerically. In the repulsive regime  $U > 0$ , a  $d$ -wave symmetric state at some dopings  $n - 1$  is believed to be located close to the antiferromagnetic insulator. The shapes of the phase boundaries in the doped case remain hypothetical.



### 3 Constructing the Hubbard model for fermionic atoms

Some of the ingredients and necessary steps to perform a quantum simulation of the Hubbard model with ultracold fermionic atoms are described in this chapter. First, the physics of ultracold Fermi gases in harmonic traps and their manipulation using optical potentials is reviewed. Then, the use of optical lattices as well as the interaction between ultracold atoms in free space and in the lattice is analyzed. A central aspect is the microscopic derivation of the Hamiltonian and all the parameters from first principles [41, 42]. Finally, some numerical approaches that allow simulation of the system in certain limiting regimes are presented.

#### *Fermi gases*

A corner stone of quantum mechanics is the non-classical behavior of indistinguishable particles. In general, the many-body wavefunction of an ensemble of identical particles always obeys the quantum statistics of the spin of the particles. This spin statistics theorem by Pauli [43] assigns a well defined symmetry to the wavefunction. The wavefunction of particles with a bosonic integer spin is symmetric under the exchange of any two particles while in an ensemble of fermionic particles with half-integer spin the exchange of any two particles inverts the sign of the wavefunction. These statistical rules are not a postulate but can be derived within the more fundamental framework of relativistic quantum field theory [44, 45].

The various phenomena arising from the quantum statistics of indistinguishable particles are closely related to their wave-like attributes. The de Broglie relation associates a wavelength  $\lambda$  to a particle with momentum  $p$  via Planck's constant  $h$ :

$$\lambda = h/p. \tag{3.1}$$

As is commonly shown in wave mechanics and optics, phenomena like diffraction, interference and wave-like effects involve scales, particle distances, and structures  $d$  of the order of the wavelength or smaller,

$$d \lesssim \lambda. \tag{3.2}$$

In thermal equilibrium a temperature can be associated with the ensemble and the average momentum of a particle depends only on the mass  $m$  and the tem-

perature  $T$  via Boltzmann's constant  $k_B$ ,

$$p \sim \sqrt{mk_B T}. \quad (3.3)$$

From these estimates, a boundary between classical mechanics and quantum mechanics can be expected to be located roughly at

$$mk_B T \sim n^{2/3} h^2 \quad (3.4)$$

where  $n^{1/3} = d$  is the average density of particles in the ensemble. The regime of quantum mechanics where the left hand side of Equation 3.4 is smaller than the right hand side, appears unreachable when the variables and constants are expressed in SI units where  $h \sim 10^{-33} \text{ kg m}^2 \text{ s}^{-1}$ . Only low temperatures, light particles and high densities can allow the observation of quantum mechanical effects in matter. Yet there are common systems that are deep within this regime of quantum degeneracy: electrons in solids generally resemble such a quantum degenerate state already at temperatures far above room temperature owing to their light mass and high density. Due to their large mass, atomic ensembles at typical densities of liquids and solids, however, are usually not quantum degenerate even at low temperatures of a few Kelvin. A notable exception here are the various quantum liquids and solids of the light isotopes of Helium,  $^4\text{He}$  and  $^3\text{He}$ .

When bringing a gaseous atomic ensemble into the regime of quantum degeneracy the density has to be kept low enough to prevent the aggregation into molecules and clusters and ultimately to suppress the tendency of the ensemble to form a liquid or solid. The sample is frequently a million times thinner than air and consequently quantum degeneracy only sets in at extremely cold temperatures, typically in the range of  $10^{-7}$  K.

### *The ideal harmonically trapped Fermi gas*

To review the thermodynamics of a trapped ideal Fermi gas, we restrict ourselves to a harmonic trap. This approximation applies to most experimental situations where the typical kinetic energies of the ultracold atomic gas are kept much smaller than the trap depth to suppress atom loss. The sample is therefore confined to a small region around the trap minimum where the potential is a nearly harmonic function of the three spatial directions  $\mathbf{x} = (x, y, z)$ ,

$$V(\mathbf{x}) = \frac{1}{2} m \left( \omega_x^2 x^2 + \omega_y^2 y^2 + \omega_z^2 z^2 \right). \quad (3.5)$$

The steepness of the potential in the three directions is parametrized by the trapping frequencies  $\omega_{x,y,z}$ . The characteristic mean trapping frequency is  $\omega =$

$(\omega_x \omega_y \omega_z)^{1/3}$ . The Hamiltonian for the potential of Equation 3.5 is a three-dimensional harmonic oscillator.

The quantum mechanical eigenstates of a single particle are products of Gauss-Hermite functions with the quantum numbers  $\mathbf{n} = (n_x, n_y, n_z)$  and the eigenenergies

$$E_{\mathbf{n}} = \left(\frac{1}{2} + n_x\right) \hbar \omega_x + \left(\frac{1}{2} + n_y\right) \hbar \omega_y + \left(\frac{1}{2} + n_z\right) \hbar \omega_z. \quad (3.6)$$

The approximation of a locally constant density (LDA) is invoked [46, 47] to derive the desired quantities from the many-body system. It assumes that in an environment around each point  $\mathbf{x}$  the system can be described as a homogeneous system in the grand canonical ensemble. The local properties such as density or specific entropy are then determined via the global parameters temperature  $T$  and chemical potential  $\mu$ . The chemical potential is shifted to  $\mu_{\text{LDA}}(\mathbf{x}) = \mu - V(\mathbf{x})$  to account for the spatially varying trapping potential. In most experiments, the temperature exceeds the energy level spacing of the harmonic oscillator at the chemical potential by far, and the discrete energies  $E_{\mathbf{n}}$  can be replaced by a smooth density of states if  $k_B T \gg 1/\rho(\mu)$  with [48]

$$\rho(E) = \frac{E^2}{2(\hbar\omega)^3}. \quad (3.7)$$

The probability that a state at an energy  $E$  is occupied by a particle is given by the Fermi distribution function

$$n(E) = \frac{1}{e^{(E-\mu)/k_B T} + 1}. \quad (3.8)$$

It is unity for states deep in the Fermi sea with energies much smaller than the chemical potential and vanishes for energies much above the chemical potential. The width of the Fermi edge at  $E \sim \mu$  is determined by the temperature.

All information about the system is now contained in the grand canonical potential and its derivatives,

$$\Omega = k_B T \int_0^\infty \rho(E) \ln(1 - n(E)) dE = -\frac{1}{6(\hbar\omega)^3} \int_0^\infty \frac{E^3}{e^{(E-\mu)/k_B T} + 1} dE. \quad (3.9)$$

The inverse temperature and the characteristic energy scale of the trap are abbreviated by

$$\beta = \frac{1}{k_B T}, \quad A = (\hbar\omega)^{-3}. \quad (3.10)$$

The integral that appears in the grand canonical potential belongs to the class of complete Fermi-Dirac integrals,

$$F_s(x) = \frac{1}{\Gamma(1+s)} \int_0^\infty \frac{t^s}{e^{t-x} + 1} dt, \quad (3.11)$$

which can be expressed in terms of an analytic continuation of the polylogarithm  $\text{Li}_s(z) = \sum_k z^k/k^s$ ,

$$-\text{Li}_{s+1}(-z) = \frac{1}{\Gamma(1+s)} \int_0^\infty \frac{t^s}{e^t/z + 1} dt. \quad (3.12)$$

The polylogarithm has a convenient recursive relation between its derivatives:

$$\frac{\partial}{\partial \mu} \text{Li}_s(e^\mu) = \text{Li}_{s-1}(e^\mu). \quad (3.13)$$

From the grand canonical potential the physical quantities of the system can be extracted as partial derivatives keeping the other parameters constant [49]. One obtains for the particle number and the entropy:

$$\Omega = -A\beta^{-4} F_3(\beta\mu) = A\beta^{-4} \text{Li}_4(-e^{\beta\mu}) \quad (3.14)$$

$$N = - \left. \frac{\partial}{\partial \mu} \right|_{T,\omega} \Omega = \int_0^\infty \rho(E)n(E) dE = -A\beta^{-3} \text{Li}_3(-e^{\beta\mu}) \quad (3.15)$$

$$S = - \left. \frac{\partial}{\partial T} \right|_{\mu,\omega} \Omega = A\beta^{-2}\mu \text{Li}_3(-e^{\beta\mu}) - 4A\beta^{-3} \text{Li}_4(-e^{\beta\mu}) \quad (3.16)$$

Experimentally, it is the particle number rather than the chemical potential that is adjusted and measured directly. The temperature can be measured directly by releasing the gas from a harmonic trap and recording and analyzing the kinetic energy of the atoms in time of flight images. To derive the chemical potential from the measured atom number and temperature, Equation 3.15 is solved numerically with respect to  $\mu$ .

While the entropy is — strictly speaking — an extensive property of the full system, it is more conveniently expressed as an average entropy per particle,

$$s = \frac{S}{N} = -\beta\mu + 4 \frac{\text{Li}_4(-e^{\beta\mu})}{\text{Li}_3(-e^{\beta\mu})}. \quad (3.17)$$

For low temperatures the entropy and the particle number can be expanded in powers of  $1/\beta\mu$  using the Sommerfeld expansion,

$$\int_0^\infty \frac{E^n}{e^{\beta(E-\mu)} + 1} dE = \mu^{n+1} \left( \frac{1}{n+1} + \frac{\pi^2 n}{6} (\beta\mu)^{-2} + \mathcal{O}(\beta\mu)^{-4} \right). \quad (3.18)$$

The full numerical solutions for  $s(T/T_F)$  and  $\mu(T/T_F)/T_F$  along with the first non-vanishing corrections to the  $T = 0$  results are shown in Figure 3.1. Close



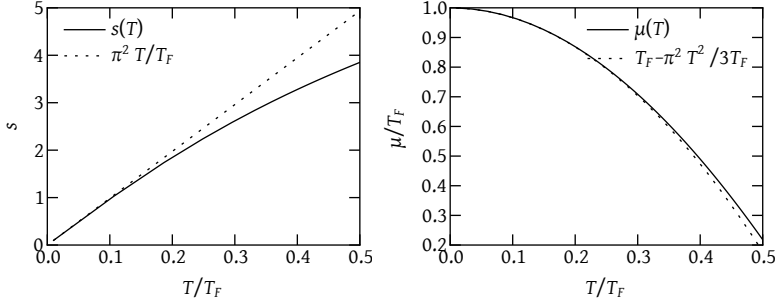


Figure 3.1: The relation between temperature  $T$ , specific entropy  $s$ , and chemical potential  $\mu$  in the local density approximation for a degenerate Fermi gas in a three-dimensional harmonic trap. In the deeply degenerate regime the temperature in units of the Fermi temperature  $T/T_F$  and the entropy per particle  $s = S/N$  (setting  $k_B = 1$ ) are proportional:  $T/T_F \approx s/\pi^2$ . Already at  $T/T_F = 0.5$ , the deviation from this linear term of the Sommerfeld expansion amounts to more than 20%. At  $T = 0$ , the chemical potential  $\mu$  equals the Fermi energy. It decreases for finite temperature as the density of states is quadratic and therefore always higher above the Fermi energy than below it.

to  $T = 0$  the specific entropy is proportional to the temperature in units of the Fermi temperature with a proportionality factor  $\pi^2 \approx 10$ . The chemical potential equals the Fermi energy at  $T = 0$  and decreases quadratically with temperature.

Entropy and particle number are both constant under all transformations of the system that are thermodynamically adiabatic and lossless. They can be regarded as invariants and will provide the input to a determination of temperature and chemical potential when loading the fermionic atoms from the harmonic trap into an optical lattice.

### Optical potentials

In the physics of ultracold atoms and molecules different aspects of their interaction with light have been used in the past. The earliest ideas were probably those by Letokhov published in 1968 [50, 51] who proposed to use a standing light wave to narrow the Doppler width of lines in atomic spectra. More recently and more prominently, the dissipative forces in near resonant electromagnetic field have allowed to cool and trap atoms at extremely low temperatures [52]. Lately, the conservative forces and potentials of light beams have received a lot of interest. Here, potentials with a depth proportional to the intensity of the electromagnetic field and varying shapes are now routinely used to trap and manipulate quantum gases [53]. The potential landscapes can be shaped on scales

of the optical wavelength using standard optical elements such as microscopes, holographic techniques, or optical masks.

Moreover, if several laser beams are brought to interference, the potential due to their fringe pattern can be treated analogously to the periodic potential of crystalline lattice structures [54]. With the use of a fermionic quantum gas, a system resembling an interacting electron gas can be created in a well controlled way. The parameters of this optical crystal, however, can be adjusted much more freely and dynamically compared to solid materials. Fundamental models from solid state theory can be tested and simulated with fermionic atoms in optical lattices in a fully synthetic fashion.

### *The dipole force*

The first successful experiments to trap atoms in mostly conservative potentials were performed by Steven Chu and collaborators in 1986 [55]. After cooling the atomic samples to  $240\ \mu\text{K}$  using the dissipative forces in a near resonant optical molasses setup, several hundred atoms could be trapped in a single tightly focused Gaussian laser beam that was detuned some  $10^4$  linewidths below the atomic resonance. Far off-resonant dipole traps (FORT) like Chu's have since become a workhorse in trapping and cooling atoms. Subsequently, bosonic alkali atoms were cooled evaporatively to achieve Bose-Einstein condensation [56] and the regime of quantum degeneracy was explored with fermionic atoms [57]. Far off-resonant optical traps are independent of the magnetic state of the atoms and can therefore be employed for atoms in states that are inaccessible using magnetic traps. The independence from magnetic fields is particularly welcome since the latter can then be used exclusively to alter and adjust the interaction between the atoms via magnetic Feshbach resonances. Evaporation and manipulation in optical traps can also be frequently achieved much more rapidly than in magnetic traps due to the larger densities and larger scattering rates.

The effect of a far-detuned monochromatic electromagnetic field on a two-level atom is most easily explained in the dressed-state picture [58]. Its experimental details and different methods of application are discussed in [53].

Neglecting spontaneous emission of photons, the Hamiltonian of the light-atom system is written as

$$H = H_0 + H_{\text{dip}} = \frac{\hbar}{2} \begin{pmatrix} -\delta_L & \Omega_1(\mathbf{x}) \\ \Omega_1(\mathbf{x}) & \delta_L \end{pmatrix}. \quad (3.19)$$

It acts on the basis of the two unperturbed states  $|g, N\rangle$  and  $|e, N-1\rangle$  which correspond to the atom in the ground state with  $N$  photons in the light field and the excited atom with one photon less in the field. All other states with more or less excitations are discarded in the rotating wave approximation. If the

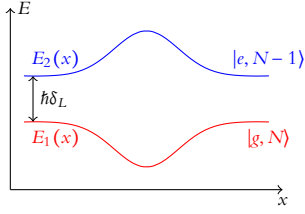


Figure 3.2: Energies of the two dressed atomic states in a Gaussian shaped laser beam. The laser is far red-detuned by  $\delta_L < 0$ .

energy difference between ground and excited state of the atom is denoted as  $\omega_0$ , the laser beam is detuned by  $\delta_L$  so that its frequency becomes  $\omega_L = \omega_0 + \delta_L$ . The zero of the energy scale is chosen to lie symmetrically between the two states resulting in  $\langle g, N | H_0 | g, N \rangle = -\hbar\delta_L/2$  and  $\langle e, N-1 | H_0 | e, N-1 \rangle = +\hbar\delta_L/2$  for the unperturbed Hamiltonian. The original states are perturbed and coupled by the electric dipole-field interaction  $H_{\text{dip}} = -\mathbf{d} \cdot \mathbf{E}(\mathbf{x})$  with the electric field operator  $\mathbf{E}(\mathbf{x})$  and the dipole operator  $\mathbf{d} = e\mathbf{r}$ . The atoms typically possess no static dipole moment but receive an induced one due to the electric field  $\mathbf{d} \propto \mathbf{E}$ . The off-diagonal elements of the coupling Hamiltonian are the Rabi energies  $\hbar\Omega_1(\mathbf{x}) = 2|\langle e, N | H_{\text{dip}}(\mathbf{x}) | g, N-1 \rangle|$ . The two eigenvectors of the complete Hamiltonian  $H$  are

$$|1\rangle = \sin\theta(\mathbf{x})|g, N\rangle + \cos\theta(\mathbf{x})|e, N-1\rangle \quad (3.20)$$

$$|2\rangle = \cos\theta(\mathbf{x})|g, N\rangle - \sin\theta(\mathbf{x})|e, N-1\rangle \quad (3.21)$$

where  $\tan 2\theta(\mathbf{x}) = -\Omega_1(\mathbf{x})/\delta_L$  is the mixing angle and

$$E_{1,2}(\mathbf{x}) = \mp\hbar\Omega(\mathbf{x}) = \mp\hbar\sqrt{\Omega_1(\mathbf{x})^2 + \delta_L^2} \quad (3.22)$$

are the energies of the two mixed — or dressed — states. The shift relative to the bare state is the so-called ac-Stark shift or light-shift. The two energies are schematically plotted in Figure 3.2 for a Gaussian laser beam.

If the laser can be far-detuned such that  $\delta_L \gg \Omega_1$ , the spontaneous emission due to the admixture of the upper state can be neglected and the energy shift of the ground state can be written as a conservative potential proportional to the light intensity:

$$V_{\text{dip}}(\mathbf{x}) \approx \frac{\hbar\Omega_1(\mathbf{x})^2}{2\delta_L} = \frac{3\pi c^2 \Gamma}{2\omega_0^3 \delta_L} I(\mathbf{x}) \quad (3.23)$$

where  $\Gamma = \omega_L^3/3\pi\epsilon_0\hbar c^3|\langle e|\mathbf{d}|g\rangle|^2$  is the decay rate of the excited state,  $c$  is the speed of light and  $I(\mathbf{x}) = 2\epsilon_0 c|\mathbf{E}(\mathbf{x})|^2$  is the local light intensity, and  $\epsilon_0$  is the dielectric constant. The dipole potential thus has the same sign as  $\delta_L$  and acts as an attractive potential for red detuning and as a repulsive potential for blue detuning.

### Scattering and heating

The treatment of the heating rate due to spontaneous emission is slightly more complex. If there are no intensity gradients and the condition of far detuning  $\delta_L \gg \Omega_1$  is fulfilled, the scattering rate of an atom is given by [53]:

$$\Gamma_{\text{sc}}(\mathbf{x}) \approx \frac{3\pi c^2 \Gamma^2}{2\hbar \omega_0^3 \delta_L^2} I(\mathbf{x}) \quad (3.24)$$

which is inversely proportional to the square of the detuning. Spontaneous emission leads to decoherence and due to the recoil energy to a continuously increasing temperature of the sample. The scaling behavior is frequently exploited to reduce the heating to negligible values. If the potential depth  $V_{\text{dip}}$  is kept constant by increasing the intensity while the laser is simultaneously farther detuned, the scattering rate drops as the inverse of the detuning.

Naively one would expect configurations using blue detuned laser light for trapping of atoms to be preferable over red detuning. The repulsive potential should lead to less heating since the atoms reside close to the intensity minima instead of close to the intensity maxima. The scattering rate of Equation 3.24 would then be minimal. A more thorough treatment of the heating in optical potentials also includes the gradient of the intensity and the electric field and the resulting micromotion of the atom [59, 58, 60]. The surprising result is that heating due to large intensities in the maxima and heating due to micromotion and large field gradients in the minima add up to the same rate independent of the detuning.

Blue detuned potentials have an additional disadvantage. They have the tendency to photoassociate atoms to molecules. The corresponding release of large amounts of kinetic energy causes heating and loss of atoms. Red detuned light can only photoassociate atoms if it is resonant with an allowed transition to a bound electronically excited state [61, 62]. It is therefore relatively easy to select a wavelength where no transition is resonant [63]. Blue detuned light, however, can couple close atom pairs to unbound electronically excited molecular states which form a continuum. The only way to circumvent this effect is to choose a wavelength where the Franck-Condon factor of the transition is small [64].

Dipole potentials can be superimposed to create almost arbitrary potentials. The most common configuration is a set of non-interfering red-detuned trapping beams to confine the atomic sample in space and a set of interfering lattice beams to impose a periodic potential onto the atoms. If the frequency difference between two beams is larger than any kinetic energy scale and not resonant with a two-photon transition to another state, the interference terms need not be considered and the potentials are simply additive.

## Dipole traps

The experiments described in the subsequent chapters make use of a crossed beam FORT consisting of two focused Gaussian beams with their waists at the position of the atoms. Their frequency difference amounts to several 100 MHz. The two beams are orthogonal and propagate horizontally in the  $x$  and  $y$  direction respectively and lead to a maximum potential depth of  $V_{Tx}$  and  $V_{Ty}$ . Their shape is given by the  $1/e^2$  intensity waists  $w_h$  and  $w_v$  in the horizontal and vertical direction, respectively. Since the waists are much larger than the wavelength, the Rayleigh range is much larger than the size of the atomic cloud and the shape change of the beams along their propagation direction can be neglected. Together with the gravitational potential the two beams form a potential

$$V_T(x, y, z) = -V_{Tx} \exp\left(-2\frac{y^2}{w_h^2} - 2\frac{z^2}{w_v^2}\right) - V_{Ty} \exp\left(-2\frac{x^2}{w_h^2} - 2\frac{z^2}{w_v^2}\right) + mgz. \quad (3.25)$$

The gravitational potential pulls the atoms downwards and leads to a sag in their equilibrium position with respect to the intensity maximum. For deep traps where the sag is small compared to the waist the new equilibrium position lies at  $z_0 \approx -m g w_v^2 / 4(V_{Tx} + V_{Ty})$ . Around the equilibrium position  $x, y, z = 0, 0, z_0$  the potential can be approximated by a three-dimensional harmonic oscillator

$$V_T(x, y, z) \approx \frac{1}{2} m \left( \omega_{Tx}^2 x^2 + \omega_{Ty}^2 y^2 + \omega_{Tz}^2 (z - z_0)^2 \right) \quad (3.26)$$

with the oscillator frequencies

$$\omega_{Tx}^2 = \frac{4V_{Ty} \exp(-2z_0^2/w_v^2)}{w_h^2 m}, \quad (3.27)$$

$$\omega_{Ty}^2 = \frac{4V_{Tx} \exp(-2z_0^2/w_v^2)}{w_h^2 m}, \quad \text{and} \quad (3.28)$$

$$\omega_{Tz}^2 = \frac{4(V_{Tx} + V_{Ty})(1 - 4z_0^2/w_v^2) \exp(-2z_0^2/w_v^2)}{w_v^2 m}. \quad (3.29)$$

## Optical lattices

If two counterpropagating far-detuned laser beams with the same polarization are focused onto the atoms, the resulting potential is a  $\cos^2$ -shaped lattice along the longitudinal propagation direction with the transverse Gaussian envelope of the original beams. The periodicity of the lattice is determined by the wavelength via  $k = 2\pi/\lambda$ . Three sets of pairwise counterpropagating beams produce a three-dimensional lattice. The potential is simply the sum of the three contributions. To suppress the effects of cross interference between the beams, the

frequencies of the three pairs are chosen to be sufficiently different.

$$\begin{aligned}
V_L(x, y, z) = & -V_{L_x} \exp\left(-2\frac{y^2 + z^2}{w_L^2}\right) \cos^2(kx) \\
& -V_{L_y} \exp\left(-2\frac{x^2 + z^2}{w_L^2}\right) \cos^2(ky) \\
& -V_{L_z} \exp\left(-2\frac{x^2 + y^2}{w_L^2}\right) \cos^2(kz)
\end{aligned} \tag{3.30}$$

Here  $V_{L[x,y,z]}$  denotes the attractive potential of each pair.

By tuning the three potential depths independently one can create situations where the atoms are strongly confined to two dimensional pancakes or even one-dimensional tubes if the intensities in one or two of the three directions are much higher than in the others. These reduced geometries are known to yield rich physics as they strongly modify the single particle density of states. Indeed, the Berezinskii-Kosterlitz-Thouless transition and the absence of long range order [65, 66, 67] has been observed in two dimensional Bose gases [68, 69].

If the three pairs of lattice beams are superimposed onto the dipole trap, their envelope contributes to the trapping frequencies and — in the case of red detuning — increases it. However, the ground state energy of the harmonic oscillator on each site being proportional to the square root of the potential reduces this increase again [70]. The trapping frequency of a three-dimensional lattice with  $V_L = V_{L[x,y,z]}$  is

$$\omega_L^2 = \frac{4V_L - 2\sqrt{E_r V_L}}{w_L^2 m}, \tag{3.31}$$

where  $E_r = \hbar^2 k^2 / 2m$  is the recoil energy, the characteristic energy scale associated with the scattering of a photon with momentum  $\hbar k$  by an atom with mass  $m$ . The trapping frequencies of FORT and lattice add in quadrature according to

$$\omega_{[x,y,z]}^2 = \omega_{T[x,y,z]}^2 + \omega_L^2. \tag{3.32}$$

The effect of a combination of FORT, lattice and gravity on the single particle states is depicted in Figure 3.3. In typical experiments with a lattice depth of  $5E_r$  the effect of the lattice potential dominates the structure of the single particle states at low energies. The states in the lowest band extend over many sites and are delocalized over the trap. States with higher energy that reach far from the center of the trap can become localized due to the steep confinement [20, 71]. These localized states are due to a combination of to the increasing localization of the single particle states of a harmonic oscillator and the band gap in the lattice. The description of a purely homogeneous lattice without the effect of the confining potential follows in the next sections.

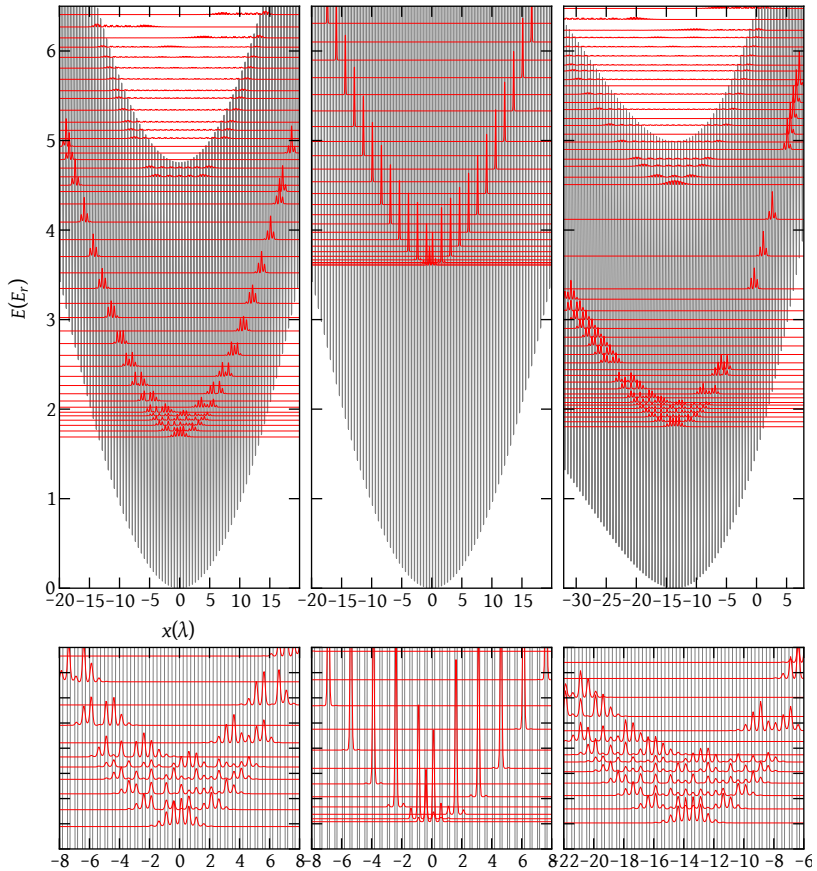


Figure 3.3: Single particle states of a  $^{40}\text{K}$  atom in a one-dimensional lattice ( $\lambda = 1064 \text{ nm}$ ) with harmonic confinement. Details of the first few states at low energies and the center of the trap are shown in the bottom row. The left plot corresponds to a  $V_L = 5E_r$  deep lattice and a Gaussian confinement with  $\omega/2\pi = 120 \text{ Hz}$ . The combined potential of lattice and trap is shown in gray. The probability density of every third state offset by the state's energy is shown in red. The band structure can be seen as well as the increasing localization of the states to the sides of the potential. The middle plot shows a deep  $V_L = 20E_r$  lattice where all states are localized within a few sites. The right plot demonstrates the situation where gravity induces a linearly increasing potential which leads to a sag in the trap minimum, a decreased localization for states at the bottom and an increased localization for top states.

### The Mathieu lattice

The Schrödinger equation for the wavefunction  $\varphi$  of a particle with mass  $m$  in a three-dimensional homogeneous lattice with a potential depth per direction of  $V_L$  is

$$E\varphi = \left( -\frac{\hbar^2}{2m}\nabla^2 + V \right)\varphi, \text{ where} \quad (3.33)$$

$$V = V_L(\cos^2(kx) + \cos^2(ky) + \cos^2(kz)). \quad (3.34)$$

The differential equation is separable in the three spatial directions and can be brought into the form of the Mathieu equation which has many applications in physics and mathematics [72, 73]:

$$\tilde{x}, \tilde{y}, \tilde{z} = kx, ky, kz \quad (3.35)$$

$$q = V_L/4E_r \quad (3.36)$$

$$\nu = \left( E - \frac{1}{2}V_L \right)/E_r \quad (3.37)$$

$$-\frac{d^2\varphi}{d\tilde{x}^2} + 2\nu \cos(2\tilde{x})\varphi = a\varphi, \quad (3.38)$$

where the recoil energy  $E_r = \hbar^2 k^2/2m$  is the characteristic energy scale of the problem. The solutions of the Mathieu equation form energy bands that are separated by band gaps.

The lowest energy of each band is designated by  $a_n(\nu)$  and the top energy of each band by  $b_{n+1}(\nu)$ . All energies within each band are eigenenergies and are shown in Figure 3.4 as shaded areas. In a one-dimensional lattice a true band gap emerges at any finite lattice depth. In a three-dimensional band structure, however, the maximum energy in the lowest band is  $3b_1(\nu)$  while the lowest energy in the first excited band is  $2a_0(\nu) + a_1(\nu)$  and the two lowest band overlap if  $\nu < 0.559$ . The condition for a true band gap in 3D is therefore  $V_L > 2.24E_r$ . Scattering between two particles could also transfer one scattering partner across the band gap into a higher band. This interband scattering is energetically forbidden as soon as the maximum energy of two particles in the lowest band  $6b_1(\nu)$  is lower than the minimum energy of two particles with one of them in a higher band,  $3a_0(\nu) + [2a_0(\nu) + a_1(\nu)]$ , which is the case for  $V_L > 3.74E_r$  [74].

### Band structure

The spatially periodic potential of a far-detuned standing light wave calls for the treatment of the atom's Hamiltonian in terms of Bloch-waves and band structures. Here the case of a general non-separable, two-dimensional, monochromatic lattice potential is considered. This configuration occurs in experiments



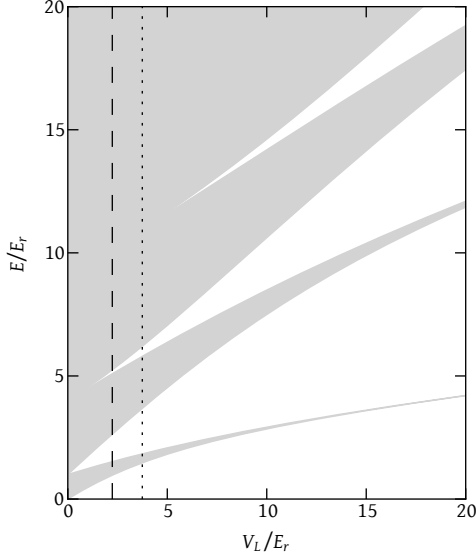


Figure 3.4: Energy bands and gaps of the Mathieu lattice. The one dimensional cosine shaped lattice potential of Equation 3.34 has solutions with real energy in the gray shaded areas. The lattice potential with depth  $V_L$  leads to a splitting of the initially continuous free space energy spectrum into bands. The dashed line at  $V_L = 2.24E_r$  marks the minimum lattice depth necessary to develop a true band gap between the lowest two bands in a three-dimensional lattice. The dotted line at  $V_L = 3.74E_r$  is the minimum depth required to prevent two-body scattering in the lowest band from promoting one of the scattering partners to a higher band.

where two beams from different orthogonal directions interfere and result in a diagonal standing wave.

$$\begin{aligned}
 V = & V_x \cos^2(kx') + V_y \cos^2(ky') \\
 & + V'_x \cos^2(kx' + \theta/2) \\
 & + 2\sqrt{V_x V_y} \cos \varphi \cos(kx') \cos(ky').
 \end{aligned} \tag{3.39}$$

$V_x$  and  $V_y$  are the potentials of two standing waves in the  $x'$  and  $y'$  directions, respectively. Their cross interference term  $\propto 2\sqrt{V_x V_y}$  depends on the phase relation between the four beams,  $\varphi$ . Additionally, a standing wave  $V'_x$  along the  $x'$  direction is included. It has a spatial offset  $\theta/2k$  and is made non interfering

with the other two standing waves either by choosing a large frequency offset or by adjusting its polarization orthogonally to the other beams.

One can now transform into a coordinate system

$$\begin{aligned}x &= x' + y' \\ y &= y' - x'\end{aligned}\tag{3.40}$$

that is rotated by  $90^\circ$  and enlarged by a factor of  $\sqrt{2}$ . Furthermore one can drop all spatially constant terms in the lattice potential as these only correspond to an energy offset. Employing the trigonometric identity  $2 \cos(a+b) \cos(a-b) = \cos(2a) + \cos(2b)$  to decompose the interference term  $\propto \sqrt{V_x V_y}$  leads to:

$$\begin{aligned}2V &= V_x \cos(kx - ky) + V_y \cos(kx + ky) \\ &+ V'_x \cos(kx - ky + \theta) \\ &+ 2\sqrt{V_x V_y} \cos \varphi (\cos(kx) + \cos(ky)).\end{aligned}\tag{3.41}$$

Decomposing the potential into its Fourier components, the potential in momentum space becomes:

$$\begin{aligned}4\tilde{V} &= (V_x + V'_x e^{\pm i\theta}) \delta_{\pm k, \mp k} \\ &+ V_y \delta_{\pm k, \pm k} \\ &+ 2\sqrt{V_x V_y} \cos \varphi (\delta_{\pm k, 0} + \delta_{0, \pm k}),\end{aligned}\tag{3.42}$$

where  $\delta_{a,b} = \delta(p_x - a) \delta(p_y - b)$  is the Dirac delta function.

The potential  $\tilde{V}$  therefore couples any free-space state with momentum  $\mathbf{p} = (p_x, p_y)$  to the 16 other states,  $(p_x \pm k, p_y)$ ,  $(p_x, p_y \pm k)$ ,  $(p_x \pm k, p_y \pm k)$ , and  $(p_x \pm k, p_y \mp k)$ . The single particle Hamiltonian in momentum space thus consists of the diagonal elements  $\mathbf{p}^2/2m = \mathbf{p}^2/m$  and the 16 off-diagonal elements of  $\tilde{V}$ :

$$\begin{aligned}H &= \sum_{\mathbf{p}} \left( \frac{\mathbf{p}^2}{m} c_{\mathbf{p}}^\dagger + \frac{1}{4} \left( (V_x + V'_x e^{\pm i\theta}) c_{\mathbf{p} \pm (k, -k)}^\dagger + V_y c_{\mathbf{p} \pm (k, k)}^\dagger \right) \right. \\ &\left. + \frac{1}{2} \sqrt{V_x V_y} \cos \varphi \left( c_{\mathbf{p} \pm (k, 0)}^\dagger + c_{\mathbf{p} \pm (0, k)}^\dagger \right) \right) c_{\mathbf{p}}.\end{aligned}\tag{3.43}$$

The summation is performed over a discrete set of momenta corresponding to a finite lattice.

The momentum  $\mathbf{p}$  (setting  $\hbar = 1$  here and in the following) is now written as the sum of an integer number of lattice momenta  $\mathbf{jk} = (j_x k, j_y k)$  and the fractional part  $\mathbf{q} = (q_x, q_y)$  with  $|q_x|, |q_y| < k/2$ :  $\mathbf{p} = \mathbf{jk} + \mathbf{q}$ . The Hamiltonian is then block diagonal and its eigenvalue problem can be solved in each  $\mathbf{q}$  sector

independently. This description is equivalent to the Bloch theorem that states that any eigenstate  $\varphi(x, \gamma)$  of a  $2\pi/k$ -periodic Hamiltonian  $H$  is the product of a  $2\pi/k$ -periodic function  $u(x, \gamma)$  and a plane wave  $e^{iq_x x + iq_y y}$  carrying the remaining fractional momentum component. Since  $\mathbf{q}$  is unique up to a multiple of  $k$  it is the so-called quasimomentum of the state in the lattice. Due to its periodicity,  $u$  can be written as a Fourier series:

$$\begin{aligned} u_{n\mathbf{q}}(x, \gamma) &= u_{n\mathbf{q}}(x + 2\pi/k, \gamma) = u_{n\mathbf{q}}(x, \gamma + 2\pi/k) \\ &= \sum_{\mathbf{j}} \nu_{n\mathbf{qj}} e^{i\mathbf{kj} \cdot \mathbf{x}}. \end{aligned} \quad (3.44)$$

With

$$\varphi_{n\mathbf{q}}(x, \gamma) = e^{i\mathbf{q} \cdot \mathbf{x}} u_{n\mathbf{q}}(x, \gamma), \quad (3.45)$$

the eigenvalue problem restricted to a  $\mathbf{q}$  subspace is

$$H\varphi_{n\mathbf{q}} = E_{n\mathbf{q}}\varphi_{n\mathbf{q}} \quad (3.46)$$

which is solved to obtain  $E_{n\mathbf{q}}$  and the eigenvectors  $\nu_{n\mathbf{qj}}$ . The band index  $n$  enumerates the solutions for a given  $\mathbf{q}$  with increasing  $E_{n\mathbf{q}}$ .

To visualize and discuss the eigenstates of a lattice one frequently resorts to a diagram of the band structure where the energy  $E_{n\mathbf{q}}$  is shown as a function of  $\mathbf{q}$  as in Figure 3.5. The detailed spatial structure of the individual wavefunctions  $\varphi_{n\mathbf{q}}(x, \gamma)$ , however, often does not convey much additional information. Their properties can be deduced from the quasimomentum which determines the fractional momentum, the proximity to states in other bands which determines the amount of admixture of higher lattice momenta and the band index which determines the spatial symmetry of the wavefunction.

In the leftmost panel of Figure 3.5 the situation of a regular  $\lambda/2$  lattice with  $V'_x = 5E_r$ ,  $V_x = 0$ , and  $V_y = 5E_r$  is shown in the view of the smaller and rotated Brillouin zone. The eigenenergies in the first few Bloch bands are shown along a triangular path through the Brillouin zone, see Figure 3.6. One observes that the lowest two bands are degenerate along the complete edge of the Brillouin zone, from the  $X$  point to the  $M$  point. In the enlarged and rotated Brillouin zone of the original coordinates, there is just one band while in the smaller Brillouin zone the triangular corners are folded back in such a way that for example the state with  $\mathbf{q}' = (k, k)$  in the lowest band in the original coordinates of the large Brillouin zone is the same as the  $\mathbf{q} = (0, 0)$  state in the second band of the small zone. The nearly complete symmetry between the lowest two bands around the line of degeneracy at the zone edge is also known as the perfect nesting condition where  $E_{\mathbf{q}} = -E_{\mathbf{q}+(k,k)}$  up to a constant: the dispersion relation of particles in the upper band and holes in the filled lower band is the same.

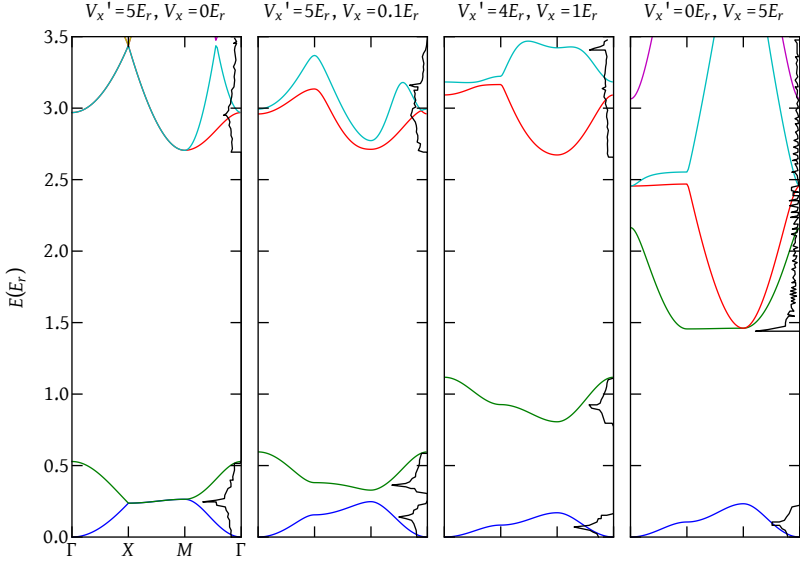


Figure 3.5: Band structure of a two-dimensional lattice. The eigenenergies along a triangular path (Figure 3.6) through the Brillouin zone are plotted for the lattice potential of Equation 3.39. The parameters of the potential for all four panels are  $V_y = 5E_r$ ,  $\varphi = 0$ ,  $\theta = \pi$ , while from left to right the potential of the non-interfering  $x$  lattice  $V_x'$  is successively transferred to the interfering  $V_x$  lattice. The density of states is shown in on the right of each band structure diagram.

The lattice spatial periodicity doubles and the degeneracy between the two lowest bands is lifted when the potential  $V_x'$  is decreased while the interfering potential  $V_x$  is increased, second to fourth plot in Figure 3.5. Increasing  $V_x$  leads to a separation of the upper half of the lowest band which then merges into the manifold of excited orbitals.

The density of states of a two dimensional lattice frequently exhibits a van Hove singularity or divergence at the center of the band. This singularity stems from the convolution of the two singularities at the band edges of a one-dimensional lattice. In three dimensions the singularities convolve into a plateau in the center of the band.

In a three-dimensional configuration each  $(q_x, q_y)$  has an additional band structure in  $z$  direction leading to multiple energy bands around each  $(q_x, q_y)$  quasimomentum solution. In a shallow lattice each of these  $z$  bands is wide and the band gaps are small leading to an overlap of the final  $x, y, z$  bands. Interaction

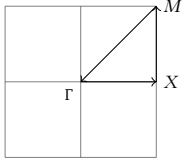


Figure 3.6: Triangular trace through the Brillouin zone. The path starts at the  $\Gamma$  point at  $\mathbf{q} = (0, 0)$  in the center, passes through the midpoint of the  $x$  edge at  $(k/2, 0)$  (the  $X$  point), proceeds along that edge to  $M$  point in the  $(k/2, k/2)$  corner, and diagonally back to  $\Gamma$ .

between particles can then mix the  $x, y$  bands more easily. In order to protect the band gaps in the  $x, y$  plane, deep lattices in  $z$  direction are required.

### Wannier functions

A new basis is constructed for each band to link the description in terms of delocalized quasimomentum states to localized states that are suitable for the site occupation basis of the Hubbard model. The delocalized wavefunctions  $\varphi_{n\mathbf{q}}(x)$  of a given band  $n$  are transformed into a set of localized Wannier wavefunctions  $w_{ij}(x)$ :

$$w_{ij}(\mathbf{x}) = \frac{1}{k} \iint_{-k/2}^{k/2} \varphi_{n\mathbf{q}}(\mathbf{x}) e^{-i\mathbf{q} \cdot (\mathbf{x} - \mathbf{x}_j)} d\mathbf{q}_x d\mathbf{q}_y, \quad (3.47)$$

$$\varphi_{n\mathbf{q}}(\mathbf{x}) = \frac{1}{k} \sum_{j_x, j_y} w_{ij}(\mathbf{x}) e^{i\mathbf{q} \cdot (\mathbf{x} - \mathbf{x}_j)}. \quad (3.48)$$

The Wannier functions are ortho-normal by construction,

$$\iint_{-\infty}^{\infty} w_{ij}(x, y) w_{il}^*(x, y) dx dy = \delta_{j_x, l_x} \delta_{j_y, l_y}, \quad (3.49)$$

and are uniquely identified by the site they are localized at,

$$w_{ij}(\mathbf{x}) = w_n(\mathbf{x} - \mathbf{x}_j). \quad (3.50)$$

It is easily overlooked that this definition is ambiguous as long as the arbitrary phase of each of the eigenfunctions  $\varphi_{n\mathbf{q}}$  is not determined in the summation. The  $w_{ij}$  are maximally localized if and only if they are symmetric in the even and antisymmetric in the odd bands and decay exponentially. In one dimension this can be enforced by choosing the  $\nu_{n\mathbf{q}j}$  to be all real for the bands where  $n$  is even and all imaginary for the odd bands. Additionally, they need to be summed as a smooth function of  $q$  [75, 76]. The Wannier functions of the first three bands of a one-dimensional lattice are shown in Figure 3.7 for different lattice depths.

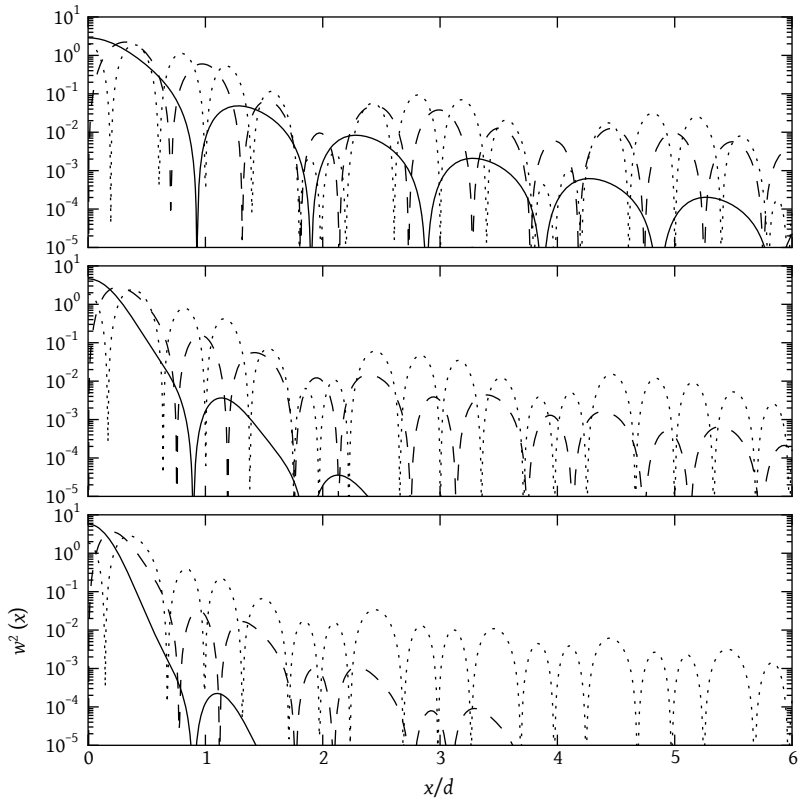


Figure 3.7: The maximally localized Wannier wavefunctions for the first three bands  $n = 0, 1, 2$  (solid, dashed, dotted) and lattice depths of  $V_L = 1, 5, 10E_R$  (top to bottom) of a one-dimensional sinusoidal lattice. In the three graphs the probability density of the Wannier functions  $w_n(x)w_n^*(x)$  is depicted as a function of the distance from their origin. The Wannier functions have  $n + 1$  zeros per site according to their symmetry and band index and show an exponential decay with increasing distance from their origin. The off-site lobes of the wavefunction are not centered on lattice sites but shifted outwards. In the higher bands the wavefunctions are increasingly delocalized and are also much less affected by changes of the lattice depth.

## Tunneling

The tunneling in an optical lattice can now be derived in position space in second quantization. Using the fermionic field operators  $\psi_\sigma(\mathbf{x})$  the Hamiltonian for kinetic energy and lattice potential  $V(\mathbf{x})$  becomes:

$$H_{\text{kin}} = \sum_{\sigma=\uparrow,\downarrow} \int \psi_\sigma^\dagger(\mathbf{x}) \left( -\frac{\hbar^2}{2m} \nabla^2 + V(\mathbf{x}) \right) \psi_\sigma(\mathbf{x}) \, d\mathbf{x} \quad (3.51)$$

The field operators  $\psi_\sigma(\mathbf{x})$  can be expanded in terms of the Wannier functions of the Bloch bands:

$$\psi_\sigma(\mathbf{x}) = \sum_{ij} w_{ij}(\mathbf{x}) c_{\sigma ij} \quad (3.52)$$

The tunneling by  $\mathbf{j}$  sites in the band with index  $n$  can be parametrized by the tunneling matrix element  $t_{ij}$ ,

$$t_{ij} = - \int w_{i0}^*(\mathbf{x}) \left( -\frac{\hbar^2}{2m} \nabla^2 + V(\mathbf{x}) \right) w_{ij}(\mathbf{x}) \, d\mathbf{x}. \quad (3.53)$$

The Wannier functions are Fourier integrals over the Bloch functions of a band. Again the Bloch functions  $\varphi_{n\mathbf{q}}(\mathbf{x})$  are the eigenvectors of the Hamiltonian  $H = -\hbar^2 \nabla^2 / 2m + V(\mathbf{x})$  with energy  $E_{n\mathbf{q}}$ . The tunneling matrix element  $t_{ij}$  is therefore simply the Fourier transform of the band structure evaluated at the tunneling vector  $\mathbf{j}$ :

$$t_{ij} = -\frac{1}{k^2} \iint_{-k/2}^{k/2} E_{n\mathbf{q}} e^{i\mathbf{q}\cdot\mathbf{j}} \, d\mathbf{q}_x d\mathbf{q}_y. \quad (3.54)$$

From the Fourier transform one can readily conclude that tunneling is small in flat bands and that the tunneling between neighboring sites where  $\mathbf{j} = (\pm 1, 0)$  or  $\mathbf{j} = (0, \pm 1)$  dominates if the band is mostly cosine shaped. In the case of a purely cosine shaped band in one dimension, the nearest neighbor tunneling matrix element is simply a quarter of the bandwidth: a factor of two from the peak-to-peak value of the cosine and another factor of two from the decomposition  $\cos q = \frac{1}{2}(\exp(iq) + \exp(-iq))$ .

If the temperature, interaction energy, and chemical potential are much smaller than the energy of the second Bloch band, only the lowest Bloch band is relevant. If additionally, the band is sufficiently cosine shaped, as is the case for deep lattices, only the tunneling between adjacent sites in the lowest band remains and one can take  $t = t_{0\mathbf{j}}$  with  $\mathbf{j} \in [(\pm 1, 0), (0, \pm 1)]$ .

The band structure and the tunneling need to be viewed together with the interaction between the atoms which both depend on the lattice depth. The ratio between on-site interaction energy and tunneling is the Hubbard parameter

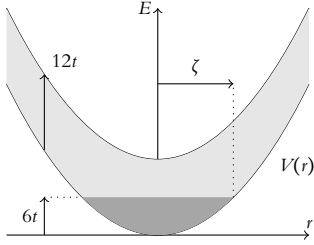


Figure 3.8: Characteristic filling in an optical lattice. The characteristic length  $\zeta$  corresponds to the radius where the trapping potential  $V(r)$  equals half the bandwidth  $6t$ .

which will be analyzed in a later section. This Hubbard parameter in the lowest band is shown for a broad range of lattice depths in Figure 3.14.

The one-dimensional dispersion relation  $E_{nq}$  can be used to assign effective masses to the quasimomentum states  $q$  by locally approximating the dispersion as a parabola. In analogy to the case of free particles where

$$E(p) = \frac{p^2}{2m}, \quad (3.55)$$

one defines in the lattice

$$m_n^*(q) = \frac{\hbar^2}{\frac{\partial^2}{\partial q^2} E_n(q)}. \quad (3.56)$$

Since narrow and flat bands have a smaller curvature compared to the free space dispersion, the effective mass is increased leading to slower dynamics.

### Characteristic filling

In a trapped cold atom system, the inhomogeneity of the trapping potential introduces a new energy scale  $m\omega^2 d^2/2$  where  $d = \lambda/2$  is the distance between two lattice sites. It can be expected that for systems where the atom number and the number of occupied lattice sites are large, a scaling law exists. The quantity denoting the size of the system, namely the total atom number  $N$ , should be expressed in terms of a characteristic atom number  $N_0$  so that their ratio uniquely identifies the physics in a trapped system independent of the absolute values of confinement, bandwidth, and chemical potential [77, 78].

To construct this scaling in three dimensions, a characteristic length scale  $\zeta$  is defined as the distance from the center of the cloud where the trapping potential energy equals half the bandwidth of the lowest Bloch band.

$$\frac{1}{2}m\omega^2 \zeta^2 d^2 = 6t. \quad (3.57)$$



This construction is shown in Figure 3.8. A sphere with a radius of  $\zeta$  contains  $N_0$  sites,

$$N_0 = \frac{4\pi}{3}\zeta^3 = \frac{4\pi}{3}\left(\frac{12t}{m\omega^2 d^2}\right)^{3/2} = 2^5\sqrt{3}\pi\left(\frac{t}{m\omega^2 d^2}\right)^{3/2} \quad (3.58)$$

Distributing  $N_0$  atoms per spin component on these  $N_0$  sites yields — at zero temperature and no interactions — a density of close to one particle per site and spin in the center of the trap. The characteristic density is then defined as

$$\rho = \frac{N}{2N_0} \quad (3.59)$$

where  $N$  is the total particle number of atoms in both spin components in a balanced spin mixture. A characteristic density  $\rho = 1$  closely corresponds to filling the lowest Bloch band at  $T = 0$ .

Under the local density assumption of a large number of sites, three quantities, namely the temperature in units of the tunneling  $T/t$ , the interaction in units of the half band width  $U/6t$ , and the characteristic density  $\rho$  are sufficient to characterize the system. They fully determine the different phases that emerge in each trap region as well as their relative size.

Slight variations of this definition can be found in the literature. The original definition was coined with one-dimensional systems in mind and leads to a different scaling in bandwidth and confinement. Other authors do not use a characteristic density but rather a characteristic trapping potential strength [64] or omit the factor of  $4\pi/3$  [79].

### *The noninteracting trapped system*

Having derived the formalism to describe the harmonic confinement in a dipole trap as well as the tunneling in the lowest band of the lattice, the Hubbard Hamiltonian in a trap without interaction can be written as:

$$H_{U=0} = -t \sum_{\sigma, \langle ij \rangle} c_{i\sigma}^\dagger c_{j\sigma} + \sum_i V_i (n_{i\uparrow} + n_{i\downarrow}). \quad (3.60)$$

This Hamiltonian can be solved numerically. It is separable in the three spatial directions and the many body state can be constructed from the single particle wavefunctions [80].

The results of such a complete, exact diagonalization of systems with up to  $N = 600 \times 10^3$  atoms on  $100^3$  sites are shown in Figure 3.9. The double occupancy defined as the fraction of atoms residing on doubly occupied sites is chosen as an observable. This quantity is experimentally well accessible and can be measured with high accuracy both in the regime of large filling and correspondingly large double occupancy as well as small fillings and small double

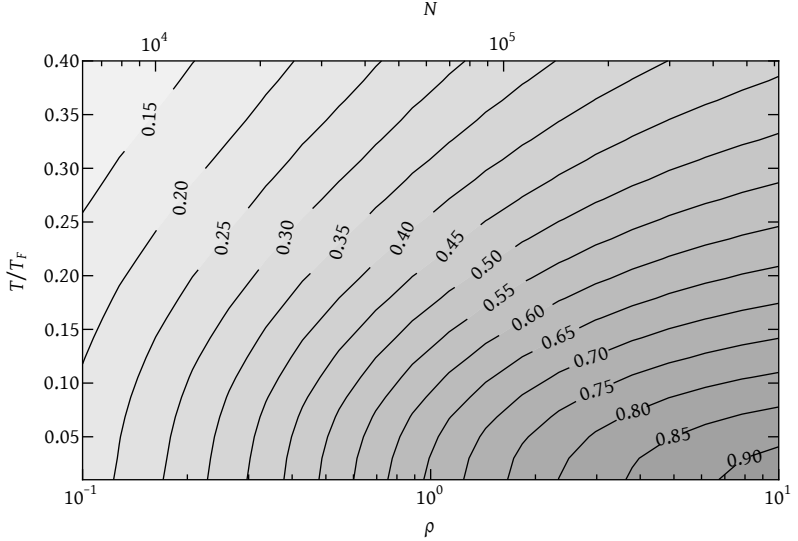


Figure 3.9: Double occupancy of a non-interacting harmonically trapped Fermi gas in an optical lattice. In universal units, the double occupancy depends only on the characteristic filling  $\rho = N/2N_0$  and temperature  $T/T_F$ . Typical experimental parameters for  $^{40}\text{K}$  are: a lattice with a spacing of  $d = 532$  nm, a lattice depth of  $7E_r$ , a tunneling rate of  $t/\hbar = 174$  Hz and a mean trapping frequency of  $\omega/2\pi = 70.2$  Hz. The characteristic atom number is then  $N_0 \approx 31 \times 10^3$ .

occupancy. Since the double occupancy depends sensitively on temperature in many experimentally relevant regimes, it can be used as a thermometer for the temperature in the lattice which is otherwise difficult to deduce.

### *Interactions between ultracold atoms*

The behavior of an ideal non-interacting quantum gas in an optical lattice is fully described by the single particle states and their quantum statistics. The phase-space distribution is obtained by filling the single particle states according to temperature and chemical potential. Intriguing complex quantum many-body states appear only by virtue of the interaction between the particles which leads to nontrivial correlations. In cold atomic systems these interactions can be precisely controlled by accessing Feshbach scattering resonances. These resonances were originally developed as a description for nuclear interactions [81]. They

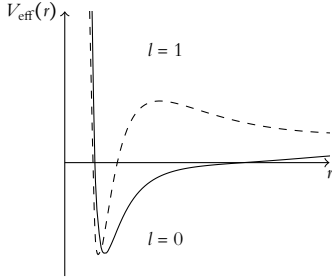


Figure 3.10: Centrifugal barrier in the interatomic scattering potential. In the limit of low energies  $k \rightarrow 0$  the centrifugal barrier suppresses scattering in the  $p$ -wave  $l = 1$  and higher channels. Only  $s$ -wave scattering with  $l = 0$  remains.

are now routinely used to prepare and explore interacting cold atomic systems [82, 83, 84, 85, 86]. Recently, the use of Feshbach resonances has also enabled ultracold chemistry with full control over the quantum state using heteronuclear alkali molecules in the ground state [87].

### Scattering at low energies

The interaction of two atoms at low energies is a textbook example of pure quantum mechanical scattering theory [88]. In dilute atomic samples it suffices to describe the two-body interaction in the spherically symmetric interaction potential  $V(r)$ . The two-body scattering wavefunction in spherical coordinates  $(r, \theta, \varphi)$  is expressed in terms of the Legendre polynomials  $P_l(\cos \theta)$  of order  $l \in \{0, 1, \dots\}$  and the radial wavefunction  $u_l(r)/r$ . The Schrödinger equation for the radial part of the scattering problem becomes

$$\frac{\hbar^2}{2m} \left( \frac{\partial^2}{\partial r^2} + k^2 \right) u_l(r) = V_{\text{eff}}(r). \quad (3.61)$$

Here the potential  $V(r)$  is replaced by an effective potential

$$V_{\text{eff}}(r) = V(r) + \frac{\hbar^2 l^2 (l+1)}{2mr^2} \quad (3.62)$$

which includes a centrifugal barrier for the higher angular momenta  $l > 0$ .

The barrier suppresses these channels at low energies  $k \rightarrow 0$  (Figure 3.10) and, at sufficiently low temperatures, only the isotropic  $s$ -wave scattering remains relevant. Additionally, for indistinguishable scattering partners, the symmetry of the scattering wavefunctions needs to be considered. Fermions of equal spin can only assume a symmetric spin wavefunction. The spatial wavefunction must therefore be antisymmetric which is the case for all odd angular momenta  $l$ : spin polarized Fermions do not interact in  $s$ -wave collisions at low temperatures.

For  $l = 0$  and large interatomic distances  $r \gg r_0$  much larger than the range  $r_0$  of the potential  $V(r)$ , Equation 3.61 can be simplified to read  $u_0''(r) = 0$  and therefore  $u_0(r) \propto r - a$ . Here  $a$  denotes the  $s$ -wave scattering length which determines the intercept of the asymptotic scattering wavefunction.

The  $s$ -wave scattering amplitude [89, 90] for small energies is  $f_0(k) = -1/(a^{-1} + ik + O(k^2))$ . Using the optical theorem one obtains from the scattering length a scattering cross section

$$\sigma_0 = \frac{4\pi}{k} \text{Im}f_0(k) = \frac{4\pi a^2}{1 + a^2 k^2}. \quad (3.63)$$

### Interatomic potentials

The notion of *ultracold atomic gases* is a thermodynamic paradox since, already at room temperature, the equilibrium phase for an alkali metal is the solid phase. Only the extremely low densities prevent three-body and higher order recombinative processes from forming clusters and releasing the binding energy in the form of kinetic energy [91]. The distances in a fermionic atomic quantum gas are on the order of the inverse Fermi wavevector  $k_F^{-1}$  and typically several hundred nm. At these large distances the interaction between two neutral alkali atoms is attractive and of the van der Waals or London dispersion type  $V(r) = -C_6/r^6$  with a characteristic length scale of  $\beta_6 = (C_6 m/\hbar^2)^{1/4}$ . In typical experiments one can assume  $k_F \beta_6 \ll 1$  [47]. The two-body scattering state is then determined solely by the behavior at large distances and the many-body behavior is only determined by the scattering amplitude [92]. Only for very steep potentials such as deep optical lattices with a short site distance, the scattering is not described anymore by this zero-range limit where  $|a^{-1} + ik|/k^2$  is much smaller than the effective range of the interaction potential. If  $k_F \beta_6 \ll 1$  holds, the generally very complicated interatomic potential can be replaced by a zero-range pseudopotential operator [49]

$$V_{\text{pseudo}}(r) = g\delta(r)\frac{\partial}{\partial r}r \quad (3.64)$$

where  $\frac{\partial}{\partial r}r$  regularizes the potential by removing  $1/r$  divergences of the wavefunction for  $r \rightarrow 0$ . The interaction parameter  $g$  is directly proportional to the scattering length

$$g = \frac{4\pi\hbar^2}{m}a. \quad (3.65)$$

The pseudopotential allows treatment in the Born approximation and allows the interaction in many-body systems to be described as a mean field if  $k_F|a| \ll 1$ .

## Feshbach resonances

Feshbach resonances have become a workhorse in experiments with ultracold atoms for several reasons. They are relatively easy to use as they can be tuned externally via a magnetic field [93, 85], using radio frequency [94] techniques, or by optical means [95, 96, 61]. Since many of them can be accessed in a nearly loss-free fashion, they provide intriguing adiabatic paths between completely different quantum many-body systems. Their use has for example enabled the observation of the crossover between BCS and BEC type superfluidity where attractively interacting Fermions are adiabatically and continuously converted into repulsively interacting Bosons [97, 98, 99].

In optical lattices, Feshbach resonances are frequently used to control the on-site interaction  $U$  and consequently the Hubbard parameter  $U/6t$ . Furthermore, the conversion of atom pairs or double occupancies into molecules either adiabatically via magnetic field sweeps or quasi-instantaneously via radio frequency (rf) pulses is used as a probe for the density correlations of the many body state [100].

Feshbach resonances arise from the electronic spin-spin coupling during the collision of two atoms, as shown in Figure 3.11. Two atoms in the hyperfine states  $|F_1, m_{F1}\rangle$  and  $|F_2, m_{F2}\rangle$  collide in the so-called open channel. Here  $F$  is the total hyperfine angular momentum and  $m_{F1,2}$  denotes its projection onto the magnetic field axis. The incoming channel is open since the collision energy is slightly above the continuum threshold. The spin-spin coupling leads to an admixture of other states that conserve the total spin  $M_F = m_{F1} + m_{F2}$ . These other state configurations  $|F'_1, m'_{F1}\rangle, |F'_2, m'_{F2}\rangle$  generally can have different interaction potentials and also a differing magnetic moment  $\Delta\mu$ . The scattering becomes resonant if the magnetic field is adjusted to a value  $B_{\text{res}}$  where some bound state in the  $|F'_1, m'_{F1}\rangle, |F'_2, m'_{F2}\rangle$  interatomic potential — the closed channel — coincides in energy with the collision state near the continuum threshold of the open channel. The coupling leads to a virtual population of this bound state in the closed channel. The detuning from this resonance is given by  $\hbar\delta = \Delta\mu(B - B_{\text{res}})$ .

The emergence or disappearance of a bound state in a scattering problem generally leads to a divergence of the scattering length around the point where the bound state joins the continuum of unbound states. The same effect is known from the basic single channel scattering problem of an attractive well (Figure 3.12).

In the proximity of an  $s$ -wave scattering resonance, the magnetic field dependence of the scattering length is generically described by [83, 101]

$$a(B) = a_{\text{bg}} \left( 1 - \frac{\Delta B}{B - B_0} \right), \quad (3.66)$$

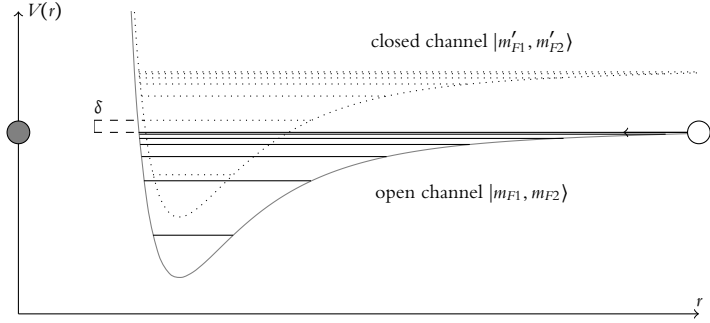


Figure 3.11: Feshbach resonance due to coupling between two collisional channels. The differing magnetic moments of the closed and open channel allow the energies to be tuned relative to each other. For vanishing detuning  $\hbar\delta \rightarrow 0$  this leads to resonant coupling between atoms colliding in the open channel and the bound state in the closed channel.

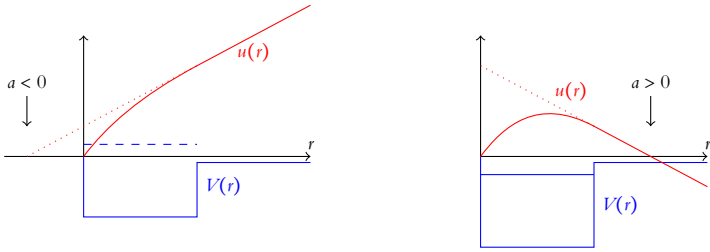


Figure 3.12: Positive and negative scattering lengths in an attractive potential. The  $s$ -wave scattering length  $a$  is the intercept of the radial scattering wavefunction  $u(r)$  which for large distances behaves as  $u(r) \propto r - a$ . As the attractive potential gets deeper,  $a \rightarrow -\infty$ . If a new bound state lies just at the threshold of zero binding energy, the scattering length diverges. Approaching the resonance from the other side where the binding strength is decreased by an increasingly shallow potential,  $a \rightarrow \infty$ .

where  $a_{\text{bg}}$  is the background scattering length far away from the resonance. It is determined by the highest lying vibrational state of the open channel interaction potential. The position of the resonance  $B_0$  does not exactly coincide with the crossing of the bound state  $B_{\text{res}}$  and the dissociation threshold [102]. It is shifted from  $B_{\text{res}}$  due to the significant coupling to the highest lying bound state of the entrance channel potential. The width of the resonance  $\Delta B$  is determined by the effective range of the scattering potential  $r_{\text{eff}}$  and the background scattering length via  $\Delta B = 2\hbar^2 / (mr_{\text{eff}}a_{\text{bg}}\Delta\mu)$  [47].

The resonances are classified in broad and narrow Feshbach resonances. Resonances are called broad if the maximum admixture of the closed channel bound state is kept low by the proximity to the anticrossing with the highest bound state in the entrance channel. If the maximum admixture of the closed channel is significant, the resonance is narrow. In terms of length scales a resonance is considered wide if the effective range of the interaction potential is comparable or smaller than the true van der Waals length scale  $\beta_6$ . Broad resonances can be successfully modeled using a single-channel approach, narrow resonances require two- [84] or even multi-channel models [103]. Wide resonances are generally preferable from an experimental viewpoint as they offer easier magnetic field control and simple theoretical modeling.

The region around a Feshbach resonance allows access to several different regimes with fascinating physics: On the side of negative scattering length no two-body bound state exists without confinement, but pairs can form via the BCS mechanism and at low temperatures the system of fermionic atoms exhibits superfluidity [104]. By sweeping the magnetic field in such a way that the scattering length diverges to  $-\infty$ , the scattering pairs are adiabatically bound to molecules. In the regime where  $a \rightarrow \pm\infty$  the character of the superfluidity corresponds to resonance superfluidity [105]. The region where  $|k_F a| \gg 1$  is especially interesting as it corresponds to a crossover phase where the only remaining length scale is the interatomic distance or equivalently the inverse Fermi momentum, as can be seen in the cross section of Equation 3.63. In this unitarity limit the system behaves in a thermodynamically universal way [106] and can be modeled analogously to neutron stars or quark-gluon plasmas. On the side of positive scattering length fermionic atoms are weakly bound to bosonic molecules and can Bose condense. The system then exhibits BEC type superfluidity. Fermionic atoms in this bound state are very stable as the size of the Feshbach molecule is large and the constituents see each other as independent fermions which suppresses three-body decay by Pauli blocking [107]. Close to the resonance on the BEC side the binding energy of the molecule is given by the Wigner formula [88]

$$E_b = -\frac{\hbar^2}{ma^2}. \quad (3.67)$$

Far away from the resonance, for smaller values of  $a$ , the long-range van der Waals tail and the anticrossing with the highest bound state of the entrance channel need to be taken into account [101, 108].

### *Interactions in optical lattices*

At low temperatures and correspondingly low energies only the interatomic  $s$ -wave scattering contributes significantly to the interaction and it can be modeled

as a contact pseudopotential, Equation 3.64, which is proportional to the  $s$ -wave scattering length of the atoms. In an optical lattice, the pseudopotential approximation requires that harmonic oscillator length on a lattice site  $a_{\text{ho}} = \sqrt{\hbar/m\omega_{\text{site}}}$  is much smaller than the van der Waals length  $\beta_6$ . The wavefunction in very deep optical lattices can become confined to small length scales where the requirements for the asymptotic regime are violated [109].

Using the expansion of the field operator in terms of Wannier functions of Equation 3.52, the many-body Hamiltonian for the interaction  $W(\mathbf{x})$  of two particles in an optical lattice becomes:

$$\begin{aligned} H_{\text{int}} &= \frac{g}{2} \int \psi_{\uparrow}^{\dagger}(\mathbf{x})\psi_{\downarrow}^{\dagger}(\mathbf{x})\psi_{\downarrow}(\mathbf{x})\psi_{\uparrow}(\mathbf{x}) \, d\mathbf{x} \\ &= \frac{g}{2} \sum_{\substack{m,n,o,p \\ i,j,k,l}} c_{\uparrow m i}^{\dagger} c_{\downarrow n j}^{\dagger} c_{\downarrow o k} c_{\uparrow p l} \int w_{m i}^*(\mathbf{x}) w_{n j}^*(\mathbf{x}) w_{o k}(\mathbf{x}) w_{p l}(\mathbf{x}) \, d\mathbf{x}. \end{aligned} \quad (3.68)$$

If the off-site interaction terms where  $i, j, k, l$  are not all equal are small compared to the other energy scales in the model, they can be neglected. The remaining terms are all on-site and can be written as

$$H_{\text{int, on-site}} = \sum_{m,n,o,p} U_{m n o p} c_{\uparrow m i}^{\dagger} c_{\downarrow n i}^{\dagger} c_{\downarrow o i} c_{\uparrow p i} \quad (3.69)$$

$$U_{m n o p} = \frac{g}{2} \int w_m^*(\mathbf{x}) w_n^*(\mathbf{x}) w_o(\mathbf{x}) w_p(\mathbf{x}) \, d\mathbf{x}. \quad (3.70)$$

The interaction terms can be grouped in two classes: those that are diagonal in the basis of the Wannier functions in different Bloch bands  $U_{m m m m}$  and those that couple different bands  $U_{m n o p}$  with  $m \neq p$  or  $n \neq o$ .

If the Wannier functions can be approximated as 3D harmonic oscillator levels, the problem of two interacting particles can be solved analytically for a regularized contact interaction pseudopotential [110]. The resulting coupling of the harmonic oscillator levels (Figure 3.13) has also been observed experimentally [17].

All terms apart from  $U_{0000}$  can be omitted for scattering lengths much smaller than the harmonic oscillator length, and the on-site interaction becomes proportional to the overlap integral in the lowest band. Setting  $U = U_{0000}$ , the dominant term of Equation 3.70 represents the interaction term in the Hubbard Hamiltonian.

$$\begin{aligned} H_{\text{int}} &= \frac{g}{2} \int w_0(\mathbf{x})^4 \, d\mathbf{x} \sum_i c_{\uparrow i}^{\dagger} c_{\downarrow i}^{\dagger} c_{\downarrow i} c_{\uparrow i} \\ &= U \sum_i n_{\uparrow i} n_{\downarrow i} \end{aligned} \quad (3.71)$$



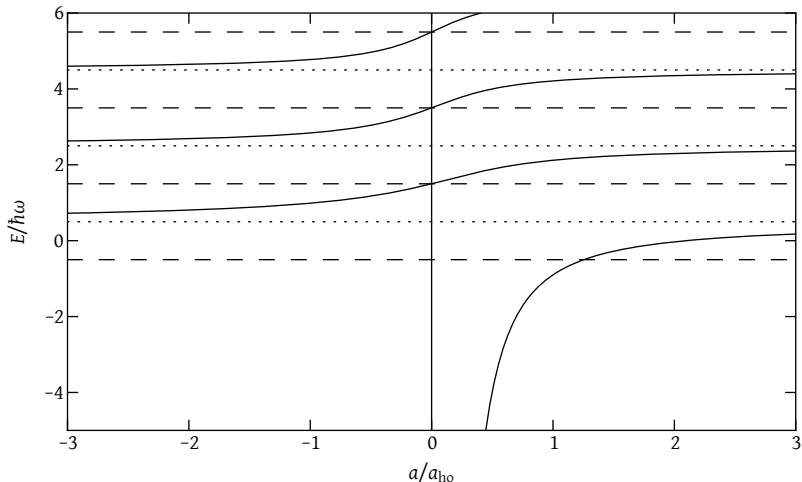


Figure 3.13: Energy levels of two interacting particles in a harmonic oscillator (solid). While for non-interacting particles the energies are located at  $2n + 3/2$  (dashed), on resonance they become  $2n + 1/2$  (dotted), on every resonance crossing the harmonic oscillators levels are adiabatically shifted to their adjacent levels. Below the lowest oscillator level, a true bound state exists which is independent of the confinement.

We furthermore take the nearest neighbor tunneling  $t = t_{0(1,0)}$  from Equation 3.53 as the kinetic energy term and obtain the single band Hubbard model.

$$H_{\text{kin}} = t \sum_{\langle ij \rangle, \sigma} c_{\sigma j}^{\dagger} c_{\sigma i}^{\dagger} \quad H_{\text{int}} = U \sum_i n_{\uparrow i} n_{\downarrow i} \quad (3.72)$$

$$H = H_{\text{kin}} + H_{\text{int}} \quad (3.73)$$

The typical Hubbard parameters  $U/6t$  and the limits of the applicability [111, 112, 3] of the assumptions that have been made so far are analyzed in Figure 3.14.

In order to describe the system for large scattering lengths where the assumption of negligible coupling to higher bands ceases to be correct, different approaches have been proposed, see Figure 3.15. One can expand the optical lattice potential around the site's center and treat the two-body scattering problem in a purely harmonic oscillator [110]. This method already fails to describe the regime of low scattering length where the single-band  $U$  would still be correct since the Wannier function of the lowest band is significantly larger than the analytic harmonic oscillator obtained from the expansion. The approach must therefore systematically overestimate the interaction energy. If one takes the distance of the two lowest bands to be the harmonic oscillator energy, the low- $a$

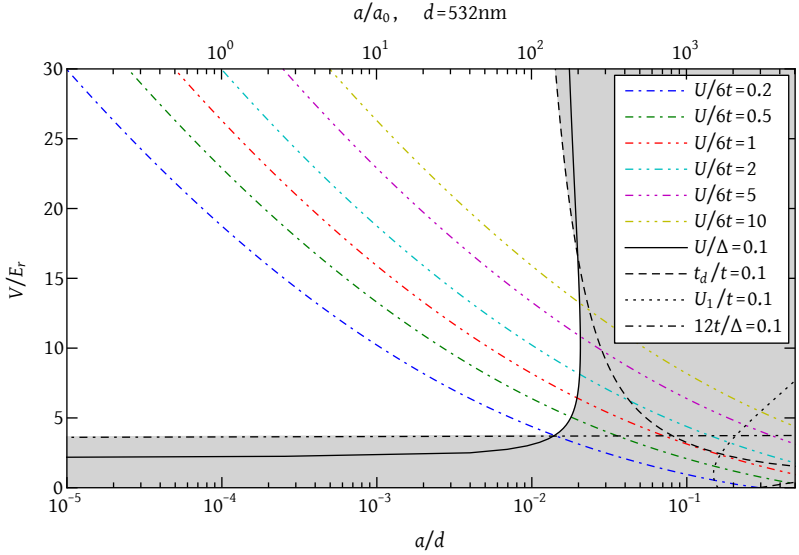


Figure 3.14: Applying the Hubbard model to ultracold atoms in an optical lattice. The plot shows the contours of constant Hubbard parameter  $U/6t$  versus the experimental parameters of lattice depth  $V$  and scattering length  $a$ . The scattering length is given in units of the site distance  $d$  (bottom axis) and the Bohr radius  $a_0$  (top). The regime where the straight forward description in terms of only the single-band tunneling  $t$  and single-band on-site interaction  $U$  ceases to be applicable is shaded in gray. Here one of several parasitic processes may become relevant. If  $U > 0.1\Delta$  (solid line), where  $\Delta$  is the band gap, the onsite interaction can possibly cause a coupling to the Wannier functions in higher bands. If  $t_d > 0.1t$  (dashed), then density-assisted hopping which corresponds to terms such as  $t_d c_{\uparrow i}^\dagger c_{\downarrow i+1}^\dagger c_{\downarrow i} c_{\uparrow i}$  plays a role. The area with  $U_1 > 0.1t$  (bounded by the dotted line) corresponds to the regime where direct nearest neighbor interaction becomes sizable. Finally, the bandwidth should be much smaller than the band gap  $12t < 0.1\Delta$  (dash-dotted line) to prevent thermal excitations to higher bands.

behavior is correctly reproduced and for larger scattering lengths, one observes a reduction of the interaction energy due to the coupling to higher bands. One can also diagonalize the full on-site interaction Hamiltonian of Equation 3.70 for two particles. This particular approach reproduces the low- $a$  behavior and leads to a more drastic reduction of the interaction energy compared to the harmonic oscillator approach due to the flatter potential for higher energies. Coming from another angle, one can also choose  $U$  in such a way that the low-energy scattering behavior instead of the bound states are correctly reproduced [42]. Here the

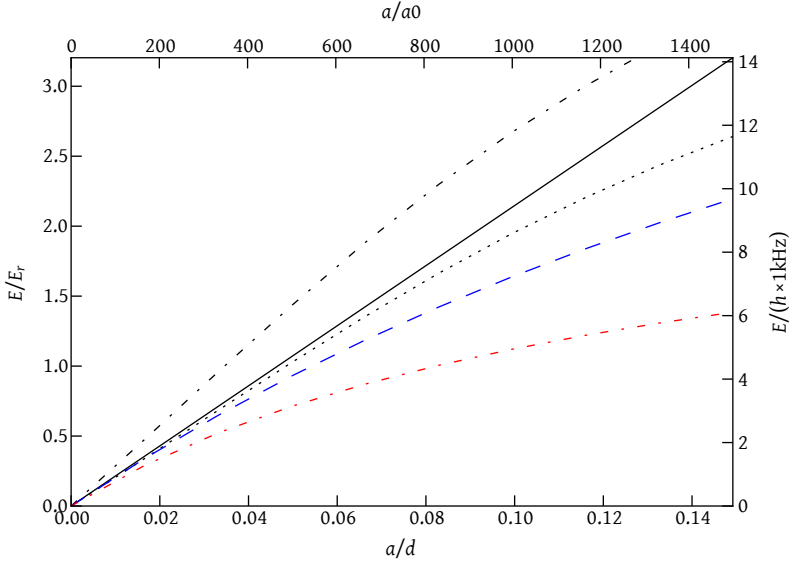


Figure 3.15: Comparison of different large- $a$  approaches. For a  $V = 12E_r$  lattice with a site spacing of  $d = \lambda/2 = 532$  nm the on-site interaction energy for  $^{40}\text{K}$  is calculated using different methods. The solid line shows the widely used approximation  $U = U_{0000}$ . The dash-dotted and dotted lines show the result for the harmonic oscillator as in Figure 3.13, once for the analytic oscillator frequency (upper dash-dotted) and once for the band separation as oscillator frequency (dotted). The dashed line is a numeric diagonalization of the interaction in the Wannier basis and the lower dash-dotted curve represents a recent result for the low-energy scattering behavior in the Hubbard model.

reduction of the interaction energy is most severe but the high-energy bound state can not be treated.

### *The high temperature series*

#### *The atomic limit*

One of the cases where the Hubbard model can be solved perturbatively is the limit of high temperatures  $T \gg t$  [113, 114, 115]. In this limit, a good starting point is the description of a single site in the grand canonical ensemble. The site is embedded in a bath that determines a temperature  $T = 1/\beta$  (setting  $k_B = 1$ ) and a chemical potential  $\mu$ . The tunneling is the process that connects a site to

its neighbors and serves to exchange energy ( $T$ ) and particles ( $\mu$ ). It mediates coherence over several lattice sites only at low temperatures. With increasing temperature, the effect of the coherent tunneling is limited to small distances and a description in terms of local processes is valid.

The high temperature series is an expansion around the atomic limit  $t = 0$  in powers of  $t/T$ . From the grand canonical partition function for the Hubbard Hamiltonian  $H$

$$Z = \text{Tr} \exp(-\beta H), \quad (3.74)$$

the grand canonical potential  $\Omega$  is obtained:

$$\Omega = -\frac{\ln(Z)}{\beta}. \quad (3.75)$$

It is derived to yields thermodynamic quantities such as the particle number  $N$ , the entropy  $S$ , the double occupancy  $D$ , and the energy  $E$ :

$$N = -\frac{\partial \Omega}{\partial \mu}, \quad S = -\frac{\partial \Omega}{\partial T}, \quad D = \frac{\partial \Omega}{\partial U}, \quad E = \Omega + TS + \mu N. \quad (3.76)$$

For a single isolated site the Hubbard Hamiltonian reduces to  $H_0 = U n_\uparrow n_\downarrow - \mu(n_\uparrow + n_\downarrow)$  and the partition function is the trace over the Boltzmann factors of the four possible states  $|0\rangle$ ,  $|\uparrow\rangle$ ,  $|\downarrow\rangle$ , and  $|\uparrow\downarrow\rangle$ :

$$\begin{aligned} Z_0 &= 1 + 2 \exp(\beta\mu) + \exp(2\beta\mu - \beta U) \\ &= 1 + 2z + z^2 u \end{aligned} \quad (3.77)$$

with the fugacity  $z = \exp(\beta\mu)$  and  $u = \exp(-\beta U)$ . The extension to  $k$  sites in the atomic limit with  $H_0 = \sum_i U n_{i\uparrow} n_{i\downarrow} + \sum_i \mu(n_{i\uparrow} + n_{i\downarrow})$  can be done directly: the partition function becomes  $Z_0^k$  and the potential is  $k\Omega_0 = -k \ln Z_0/\beta$ .

### *The series expansion*

The tunneling term  $W = t \sum_{\langle ij \rangle} c_j^\dagger c_i$  prevents this factorization but it can be treated perturbatively for  $0 < t \ll T$  by writing [49]

$$\begin{aligned} Z &= \text{Tr} \exp(-\beta H_0 - \beta W) \\ &= Z_0 + Z_0 \sum_{j=1}^{\infty} (-1)^j \int_0^\beta \int_0^{\tau_1} \cdots \int_0^{\tau_{j-1}} \langle \tilde{W}(\tau_1) \tilde{W}(\tau_2) \cdots \tilde{W}(\tau_j) \rangle_0 d\tau_j \cdots d\tau_2 d\tau_1. \end{aligned} \quad (3.78)$$

Here the interaction representation for  $W$  is used,

$$\tilde{W}(\tau) = \exp(\tau H_0) W \exp(-\tau H_0), \quad (3.79)$$

and the expectation value of an operator  $A$  is evaluated in the unperturbed Hamiltonian,

$$\langle A \rangle_0 = \text{Tr}[\exp(-\beta H_0) A] / Z_0. \quad (3.80)$$

By applying the expansion of Equation 3.78 in the grand canonical potential of Equation 3.75, the perturbative contributions to  $\Omega$  can be grouped by powers of  $\beta t / Z_0$ ,

$$\Omega = -\frac{k}{\beta} \ln Z_0 - \frac{k}{\beta} \sum_{l=1}^{\infty} \left( \frac{\beta t}{Z_0} \right)^l X_l. \quad (3.81)$$

### Second order

The first non-vanishing term in this series is  $X_2$  and corresponds to hopping to a neighboring site and back. In a simple cubic lattice only the  $m = 6$  neighboring sites can be reached by this tunneling order and only by a single path resulting in a single hopping diagram to be evaluated. The trace in Equation 3.80 is performed over the  $4 \cdot 4 = 16$  states  $|\psi_2\rangle$  of two neighboring sites yielding the following contributions  $\langle \psi_2 | \tilde{W}(\tau_1) \tilde{W}(\tau_2) | \psi_2 \rangle_0$  to  $X_2$ :

$ \psi_2\rangle =  n_{\uparrow} n_{\downarrow}, n_{\uparrow} n_{\downarrow}\rangle$	$\langle \psi_2   \tilde{W}(\tau_1) \tilde{W}(\tau_2)   \psi_2 \rangle_0$
$ 0, 0\rangle$	$1 \cdot 0 \cdot z^0 u^0$
$ \uparrow\downarrow, \uparrow\downarrow\rangle$	$1 \cdot 0 \cdot z^4 u^2$
$ \uparrow, \uparrow\rangle,  \downarrow, \downarrow\rangle$	$2 \cdot 0 \cdot z^2 u^0$
$ \uparrow, 0\rangle,  \downarrow, 0\rangle,  0, \uparrow\rangle,  0, \downarrow\rangle$	$4 \cdot 1 \cdot z^1 u^0$
$ \uparrow\downarrow, \uparrow\rangle,  \uparrow\downarrow, \downarrow\rangle,  \uparrow, \uparrow\downarrow\rangle,  \downarrow, \uparrow\downarrow\rangle$	$4 \cdot 1 \cdot z^3 u^1$
$ \uparrow, \downarrow\rangle,  \downarrow, \uparrow\rangle$	$2 \cdot 2 \cdot z^2 u^0 \exp(-U(\tau_2 - \tau_1))$
$ \uparrow\downarrow, 0\rangle,  0, \uparrow\downarrow\rangle$	$2 \cdot 2 \cdot z^2 u^1 \exp(U(\tau_2 - \tau_1))$

Each contribution is the number of configurations in the left column times the number of tunneling processes possible in each configuration multiplied by the respective expectation value. Each site adds  $m/2$  new bonds and hence, up to second order, the grand canonical potential is

$$\Omega_2 = -\frac{k}{\beta} \ln Z_0 - \frac{k}{\beta} \left( \frac{\beta t}{Z_0} \right)^2 m \left( z + z^3 u + 2z^2 \frac{1-u}{\beta U} \right). \quad (3.82)$$

### Higher orders

Graph theoretical approaches are frequently used to determine the hopping and interaction diagrams for higher orders in the perturbative expansion as well as the respective configurations and their contributions [113]. Since the number of configurations for each diagram of order  $l$  increases approximately as  $4^l$  and the number of diagrams also grows exponentially, the task becomes exceedingly

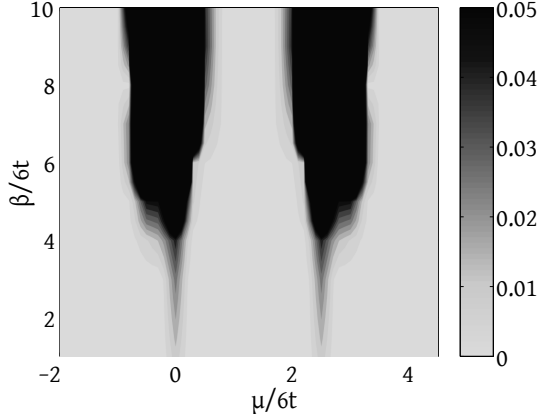


Figure 3.16: Regimes of convergence and divergence of the high temperature series for  $U/6t = 2.5$ . The figure shows the color coded density error of the high temperature series in tenth order compared to dynamical mean field theory (DMFT). The parameter space is spanned by the chemical potential  $\mu$  and the inverse temperature  $\beta = 1/T$ . Both axes are rescaled by  $6t$ .

complex. The second order contains only four terms, but in fourth order there are already 29 terms and, for the tenth order, some 1000 terms need to be analyzed.

It can be expected from the structure of the high temperature expansion in Equation 3.81 that for  $\beta t > 1$  (that is  $T < t$ ) the series will not converge as the terms  $(\beta t)^l$  grow exponentially. The respective coefficients of each additional order  $X_l$  do not have alternating signs nor do they decay faster than  $(\beta t)^l$  grows. The series indeed diverges as depicted in Figure 3.16 where expansion orders up to  $l = 10$  are compared. The divergence signals the vicinity to a phase transition where the tunneling can not be treated perturbatively anymore but dominates the physics. This phase transition is the Néel transition where a combination of tunneling and on-site repulsion mediate an exchange interaction between neighboring alternating spins. The high temperature expansion cannot yield insight in this regime but nevertheless remains well-behaved up to temperatures close to  $T_{\text{Néel}}$ . Additionally, the expansion has been used very successfully in the regime of  $T > t$  as a tool to calibrate and verify other numerical approaches. These new techniques like diagrammatic determinant Monte Carlo [38] aim to reach deep into the ultracold strongly correlated phases.

### *Imbalance and inhomogeneity*

The preceding calculation can be extended to include further effects. A magnetic field or a spin imbalance both correspond to separate and unequal chemical potentials for the two spin components:  $\mu(n_\uparrow + n_\downarrow)$  is replaced by  $\mu_\uparrow n_\uparrow + \mu_\downarrow n_\downarrow$ . Additionally, a locally inhomogeneous system can be represented by a site dependent energy shift  $\varepsilon_i$  and terms of the form  $\sum_i \varepsilon_i (n_{i\uparrow} + n_{i\downarrow})$  in the Hamiltonian [116]. As long as the magnitude of the inhomogeneity is smaller than the temperature, the behavior of the system is not altered.

### *The high temperature phase diagram*

Above the Néel transition, the high temperature series is able to capture all metallic, band-insulating, and Mott-insulating physics. At finite temperature and in the absence of long-range magnetic or charge order no symmetry is broken in the Fermi-Hubbard model and therefore no phase transition exists. The different phases are separated by crossover regimes where the observables change smoothly.

Figure 3.17 covers the regimes of strongly attractive to strongly repulsive interactions and fillings from an empty lattice to a band insulator. There are three insulating regimes, namely the empty lattice, the Mott insulator, and the band insulator which are separated by four different metallic transition regions. The universal line of half filling  $N \equiv 1$  is located at the diagonal of each plot where  $\mu = U/2$ . It is independent of the temperature and a characteristic feature of the intrinsically particle-hole symmetric Hamiltonian.

At low chemical potential  $\mu/6t \sim -3 \ll U$  the system is an empty band insulator (BI). Large negative  $U \sim 2\mu$ , however, lowers the energy of the doubly occupied state below the chemical potential and leads to a band insulator of double occupancies. The crossover between the empty lattice and the band insulator at  $\mu \sim U/2$  describes a metal of double occupancies and takes place without any intermediate regime of singly occupied sites. While this crossover exhibits the largest fluctuations in density in the complete phase diagram, only two states — the empty and the double occupied — are relevant and the maximum entropy per site is  $S = \log 2 \approx 0.7$ .

As soon as doubly occupied states become energetically disfavored due to repulsive interactions,  $U/6t \gg 1$ , sites are first singly occupied. The transition from an empty lattice to single occupancy takes place via a metallic state  $\mu \sim 0$  where the three states empty, spin-up and spin-down are equally likely. Here the entropy per site can become as large as  $S = \log 3 \approx 1.1$ . At large repulsive interaction  $T \ll U$  and sufficiently high chemical potential  $T \ll \mu \ll U$  all sites are singly occupied. Although the band is only half filled, the system becomes Mott insulating (MI) exclusively due to the repulsive interaction and charge

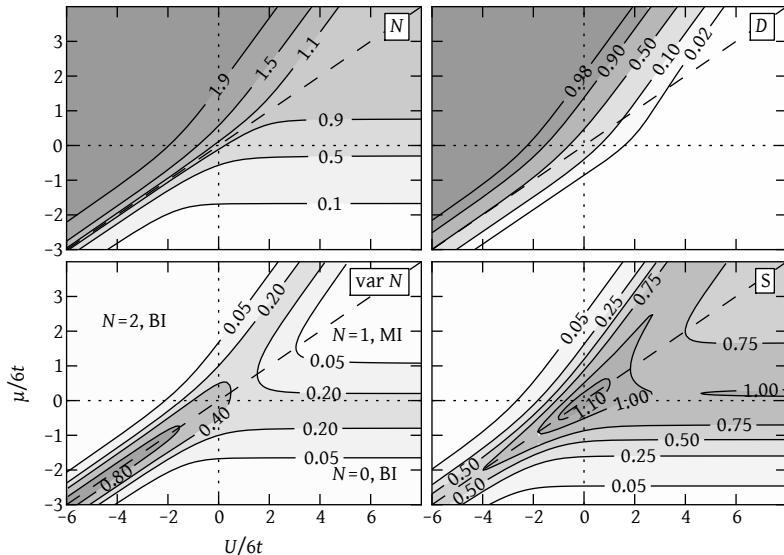


Figure 3.17: The phase diagram of the Hubbard model at  $T/t = 2.5$ . The phase space is parametrized by the on-site interaction  $U/6t$  and the chemical potential  $\mu/6t$ . From top left to bottom right: the density  $N$  in particles per site, the probability of the site being doubly occupied  $D$ , the variance of the density  $\text{var } N$ , and the entropy per site  $S$ . The high-temperature expansion up to second order has been used to obtain the phase diagram. The line of half filling  $\mu = U/2$  is indicated as a dashed line and  $\mu = 0$  and  $U = 0$  as dotted lines respectively.

fluctuations vanish. Only the spin degree of freedom remains and a site can accommodate  $S = \log 2 \approx 0.7$  of entropy. Increasing the chemical potential further to  $\mu \sim U$  permits sites to become doubly occupied at first resulting in a metal of double occupancies on top of a Mott insulator and then in a band insulator for  $\mu \gg U$ .

In the center of the phase diagram at  $\mu \sim 0$  and  $U \sim 0$  resides the region of largest entropy where all four possible occupation states for a site have the same energy and Boltzmann factor and are thus equally likely.

The width of the four metallic regions depends on the number of states that are accessed. In terms of the chemical potential, the empty-to-band-insulator transition at negative  $U$  is the narrowest while the empty-to-Mott-insulator and Mott-insulator-to-band-insulator transitions for repulsive interactions are about  $12t$  wide. At  $U = 0$  the direct transition from an empty to a full band without an



insulating intermediate phase is the widest. The width of the metallic regimes in terms of the chemical potential increases with bandwidth and with temperature.

### *Local density approximation*

The high-temperature series describes clusters of sites that grow in size with increasing order of the expansion. The atomic limit only describes a single site while the second order describes already a bond of two sites. This property can be exploited with the local density approximation (LDA) to model a complete finite system with a slowly varying inhomogeneous trapping potential. Each site is subject to the global temperature and to a chemical potential that is shifted by the local trapping potential.

$$T_i = T, \quad \mu_i = \mu - V_i, \quad (3.83)$$

The series is evaluated for each  $i$  and, by summing over all the site indices  $i$ , the properties of the complete system are obtained:

$$N_{\text{tot}} = \sum_i N_i, \quad S_{\text{tot}} = \sum_i S_i, \quad D_{\text{tot}} = \sum_i D_i. \quad (3.84)$$

If the discrete sums are now replaced by integrals, their evaluation becomes numerically stable and can be subjected to the optimizations that are implemented in various numerical integration methods. These algorithms determine the integrals to a given accuracy by choosing a suitable set of representative samples of the integrand without the need to evaluate the integrand at all sites.

Since the sites are only distinguished by their local trapping potential, the integrals over space can be rewritten as integrals over the chemical potential using the density of sites. There are  $M = 4/3\pi j^3$  sites within a sphere of radius  $j$ , and the trapping potential at the surface of the sphere is  $V = \gamma j^2$  where  $\gamma = \frac{1}{8}m\omega^2\lambda^2$ . The density of sites at a potential energy  $V$  is therefore:

$$\rho(V) = \frac{dM}{dV} = 2\pi\sqrt{\frac{V}{\gamma^3}} \quad (3.85)$$

and the global observables of the finite system become integrals over the LDA-observables, for example  $N(\mu)$ :

$$N_{\text{tot}} = \int_0^{\infty} N(\mu - V)\rho(V) dV \quad (3.86)$$

In experimental realizations, temperature  $T$  and global chemical potential  $\mu$  are often unknown because the system is finite and isolated from any particle or

energy bath. Only the total atom number  $N_{\text{exp}}$  and the total entropy  $S_{\text{exp}}$  are given or conveniently measurable. The two non-linear integral equations

$$N_{\text{tot}}(T, \mu) = N_{\text{exp}}, \quad (3.87)$$

$$S_{\text{tot}}(T, \mu) = S_{\text{exp}} \quad (3.88)$$

are solved simultaneously for  $T$  and  $\mu$  using a suitable multi-dimensional iterative numerical algorithm.

The LDA breaks down at low temperatures where the site-to-site energy offsets within a cluster of given expansion order become comparable to the temperature. In this case the local inhomogeneity within a cluster can be taken into account [116]. This becomes increasingly complex and if the extent of long-range order reaches an appreciable fraction of the system size, the cluster and hence the order of the expansion must be chosen large enough to contain these correlations ultimately leading to a single cluster for the complete system.

### *Coexistence of different phases*

In the local density approximation the local chemical potential assumes all values from  $-\infty$  up to the maximum in the trap center. This leads to a coexistence of all phases that are possible under these conditions of temperature, bandwidth and interaction. The cloud thus exhibits a rich structure of different phases in spatially separated regions. The observables density, double occupancy, holes, compressibility and entropy for a typical experimental cloud are visualized in Figure 3.18. Each observable is visualized in one of the four octants that are slightly offset outwards for clarity. The cloud is anisotropic due to the steeper confinement in vertical  $z$  direction than in the two horizontal directions. It is an oblate ellipsoid with an aspect ratio of  $1/3$ . The total atom number and repulsive interaction strength are chosen such that all five phases are expressed. From outer to inner shell they are the empty insulator, the metal in the lower Hubbard band, the Mott insulator, the metal in the upper band and the band insulator of double occupancies. All phases are separated by crossovers and can be clearly identified by their characteristic signatures in the observables.

In the top left shaded octant the atomic density indicates the strictly increasing density from outside to inside with shells of approximately constant  $N = 1$  and  $N = 2$ . These shells are also clearly identified in the density of double occupancies in the top right shaded region. The three insulating phases lead to a vanishing compressibility and a density that is constant over a certain spatially extended region. The compressibility is largest in the metallic transition regions that are located between the insulators. Contrary to the compressibility, the entropy differs from zero also in the Mott insulator due to the remaining spin entropy. From the distribution of compressibility and entropy one can expect

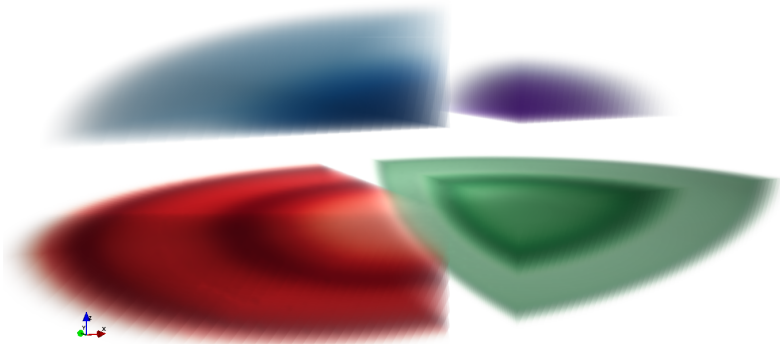


*Figure 3.18:* High temperature series simulation of a trapped Mott-insulating system. The cloud is an oblate spheroid with the  $z$ -axis in the vertical direction. The parameters are  $\mu/6t = 6$  in the center,  $T/t = 2.5$ , and  $U/6t = 4$ . Different observables are visualized in four octants of the ellipsoidal cloud. The local value of the observable is encoded in the opacity. The octants are formed by cuts along planes perpendicular to the horizontal  $x$  and vertical  $z$  axes and have been moved outward slightly for clarity. In the top left the density is encoded. It exhibits a light colored Mott insulator and a opaque doubly occupied core. In the top right, the density of only the double occupancies is rendered. The bottom two cut-outs show the compressibility (in the left) and the entropy per site (in the right octant).

that there is always at least one highly compressible and entropy-rich metallic shell. In a preview for the following chapters, it is worth noting that this shell limits the lowest observable total compressibilities but also acts as a buffer that sinks entropy away from e. g. the Mott-insulating shell.



## 4 *The experimental apparatus*

The apparatus used to achieve the experimental results presented in this thesis has continuously evolved since the start of its construction in 2001. It was extended and modified in several stages to allow different effects to be explored. Initially the apparatus was used to perform some of the first experiments with low-dimensional Bose gases [117] and Bose gases in optical lattices [118, 119]. This stage of the experimental setup is described in [120]. After extending the apparatus to also allow cooling of fermionic Potassium [121, 122] the experiment was the first to load Fermi gases in 3D optical lattices and allowed exploration of the physics of low-dimensions [22], interaction [16], confinement [123], Feshbach molecules [18, 17], and Bose-Fermi mixtures [23]. Throughout the course of this thesis the experiment has been improved to allow for a clean implementation of the Hubbard model with fermionic atoms [63].

Many experimental details have already been accurately presented in the preceding references and especially in the various theses. This chapter will only briefly review the apparatus and focus on changes and new experimental techniques.

The experimental components are conveniently separated on two optical tables. On one table the laser sources and electronics are mounted which are needed to generate the optical frequencies for cooling, trapping, manipulating, and imaging the atoms as well as to form the optical potentials. The laser sources include external cavity diode lasers and tapered amplifiers with custom mechanical, optical, and electronic design [124], as well as various solid state lasers. The lasers are stabilized using frequency modulation spectroscopy [125] or by stabilizing the beat frequency of two lasers [126]. The light is fed through optical fibers to the second table supporting the front-end beam shaping, detection, stabilization, and imaging optics, as well as the vacuum chamber and magnetic field coils. The cameras for recording images of the atomic clouds are located close to the experimental chamber. The separation permits a compact experimental setup, easy access to the different parts, and quick replacement of laser systems. It also allows acoustic decoupling of the two tables.

### *The experimental cycle*

In ultracold atom experiments, the final detection step is usually destructive as gaining a sufficient amount of information from the sample comes at the price of a significant increase of entropy and temperature. After the cooling, preparation,

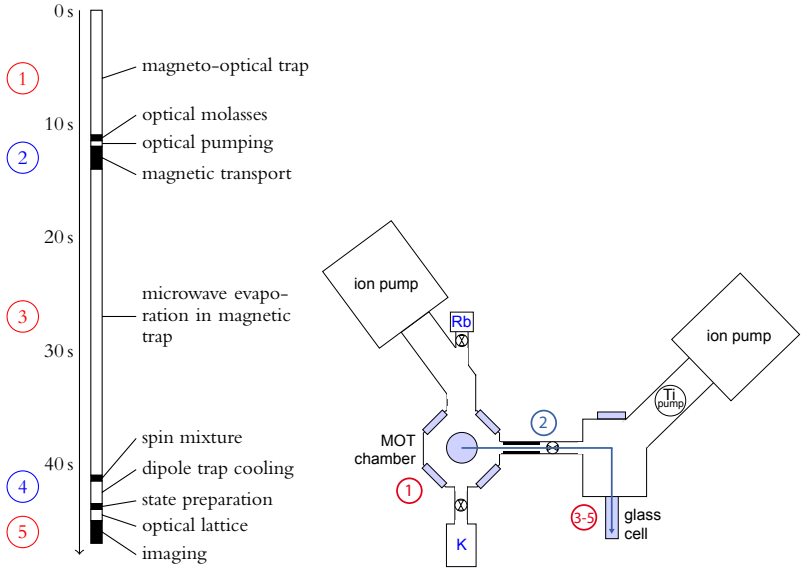


Figure 4.1: Timing sequence of an experimental cycle and sketch of the vacuum chamber. The experimental cycle starts in the MOT chamber where the atoms are collected. The atom cloud is then transported through a differential pumping tube. The main part of the experiment takes place in the glass cell in where the atoms are cooled to quantum degeneracy and loaded into the optical lattice.

manipulation, and finally imaging, a sample must be prepared anew. This experimental cycle is therefore repeated continuously while the experimental parameters are varied from cycle to cycle. As drifts and hysteresis effects can lead to unwanted variations during the thermalization of the experimental setup, the cycle is also repeated when there are no pending parameter sets. The experimental sequence is timed and controlled by a software infrastructure developed in our research group [120].

The time sequence of the cycle and a schematic representation of the vacuum components of the apparatus are shown in Figure 4.1. Each cycle starts by cooling and trapping fermionic  $^{40}\text{K}$  and bosonic  $^{87}\text{Rb}$  in a magneto-optical trap (MOT) from background vapor pressure. In the MOT region the residual gas pressure is about  $10^{-8}$  mbar and collisions with background gas atoms and molecules would prevent reaching quantum degeneracy. The clouds are therefore transported through a differential pumping region into an ultra high vacuum glass cell at about  $10^{-11}$  mbar. Here the  $^{87}\text{Rb}$  cloud is cooled by forced

evaporation in a Quadrupole-Ioffe (QUIC trap). The  $^{40}\text{K}$  cloud is cooled sympathetically by thermal contact via collisions. Both clouds reach quantum degeneracy before the bosonic cloud is discarded. The fermionic cloud is then loaded into a crossed beam dipole trap (FORT) and evaporatively cooled down to the desired temperature and atom number. Subsequently, the optical lattice potential is slowly turned on. After the experiment has been performed, several absorption images are taken and the cycle is repeated.

### *Magneto optical trap*

Two atom sources provide the required background vapor pressure to load the  $^{40}\text{K}$  and the  $^{87}\text{Rb}$  MOT in approximately 10 seconds. At  $50^\circ\text{C}$ , the equilibrium vapor pressure of Potassium is  $4 \times 10^{-7}$  mbar while that of Rubidium is  $3 \times 10^{-7}$  mbar at  $20^\circ\text{C}$ . Both sources are ampules with some of the element in solid form and are heated independently to control the background vapor pressure. The  $^{40}\text{K}$  source has been enriched from 0.012% natural abundance to approximately 7%.

The first stage in the preparation of the quantum degenerate Fermi gas, consists of collecting and laser-cooling the atoms [127]. In the three-dimensional magneto-optical trap dissipative light forces due to the combination of Doppler and Zeeman effects are used to collect and laser-cool both species [128, 129, 130]. During the first 10 s only  $^{40}\text{K}$  is collected using the optical transitions shown in Figure 4.2 [131]. In the last few seconds also  $^{87}\text{Rb}$  is collected resulting in clouds of several  $10^9$  atoms of both species. Sub-Doppler cooling of the  $^{87}\text{Rb}$  in an optical molasses configuration [132] is followed by optical pumping of the  $^{40}\text{K}$  to the  $|F = 9/2, m_F = 9/2\rangle$  state and  $^{87}\text{Rb}$  to the  $|F = 2, m_F = 2\rangle$  state. Both states are low field seekers and can hence be loaded into a magnetic quadrupole trap.

### *Magnetic transport*

By cross-fading the quadrupole field sequentially between several spatially separated coil pairs, the magnetic field zero and with it the two clouds are transported from the MOT chamber through the differential pumping tube around a corner and into the glass cell [133].

### *Quadrupole-Ioffe trap*

The magnetic field configuration is subsequently modified by turning on a Ioffe coil which transforms the pure quadrupole trap into a QUIC trap [134] to prevent losses at high densities due to Majorana spin flips [135, 136].

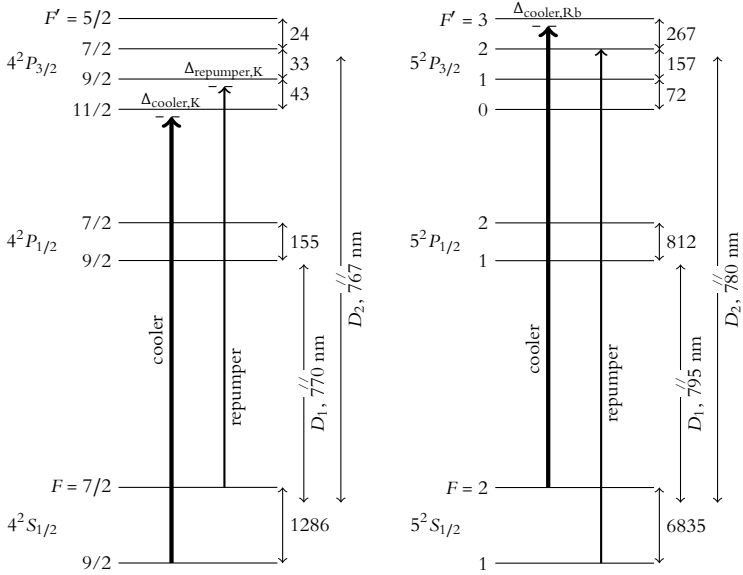


Figure 4.2: Level scheme and cooling transitions for  $^{40}\text{K}$  and  $^{87}\text{Rb}$ . During the MOT phase the main cooling is performed on the indicated transitions while driving the two repumping transitions recycles atoms that were excited off-resonantly to other levels. The  $D_2$  lines have a width of  $\Gamma/2\pi = 6.04$  MHz for  $^{40}\text{K}$  and  $5.75$  MHz for  $^{87}\text{Rb}$  respectively. All hyperfine level splittings are given in MHz.

Both clouds are in thermal contact due to the large attractive scattering length for collisions between  $^{87}\text{Rb}$  and  $^{40}\text{K}$ . In order to cool both, it is sufficient to selectively remove the high energy  $^{87}\text{Rb}$  atoms from the trap and to let the system rethermalize at lower atom number and lower temperature. The evaporation is performed by spin-flipping  $^{87}\text{Rb}$  from the trapped  $|F=2, m_F=2\rangle$  state to the anti-trapped  $|F=1, m_F=1\rangle$  state using a microwave transition. The frequency is generated using a computer controlled direct digital synthesizer (DDS) developed in our group [137]. In the outer trap regions, atoms in the  $|F=1, m_F=1\rangle$  state are parasitically transferred by the microwave to the  $|F=2, m_F=1\rangle$  and  $|F=1, m_F=-1\rangle$  states which are also trapped and lead to loss of  $^{40}\text{K}$ . These two states are statically evaporated out of the trap by an additional pair of constant microwave frequencies.



wavelength	$\lambda_T = 826.05 \text{ nm}$
horizontal waist	$w_h = 150 \mu\text{m}$
horizontal waist	$w_v = 50 \mu\text{m}$
typical final total absolute trap depth	$V_T \approx 8E_f \approx k_B \times 3 \mu\text{K}$
typical gravitational sag	$z_0 \approx -11 \mu\text{m}$
typical final trap depth with gravity	$\Delta V_T \approx 2.4E_f \approx k_B \times 0.5 \mu\text{K}$
typical final trap frequencies (measured)	$\omega_{T(x,y,z)}/2\pi = (35, 23, 123) \text{ Hz}$
typical mean trap frequency	$\omega_T/2\pi = 46 \text{ Hz}$

Table 4.1: Dipole trap (FORT) parameters. The two beams propagate horizontally in the  $x$  and  $y$  direction. The typical final parameters correspond to an evaporation down to about 36 mW per beam and depend on final power as well as on the alignment. The small waist in vertical direction allows for an easier compensation of gravity and leads to a correspondingly smaller sag.

In the last stages of the microwave evaporation, the Rubidium is completely removed from the trap and up to  $5 \times 10^6$  fermions in the  $|F = 9/2, m_F = 9/2\rangle$  state at temperatures of  $T/T_F = 0.2$  to  $0.5$  remain.

### Dipole trap

A focused pair of far red-detuned laser beams crossing at the position of the atoms is gradually turned on and the sample is transferred into this FORT by subsequently turning off the QUIC trap. The trap is characterized by the parameters listed in Table 4.1. The trapping frequencies in the FORT are determined by exciting the cloud with a short kick using either the trap itself or the magnetic field in some direction. A measurement of the oscillation period directly yields the trap frequency.

To evaporate the fermionic cloud, the spin-polarized pure  $m_F = 9/2$  sample from the magnetic trap is not suitable for two reasons: the  $m_F = 9/2$  state is not the ground state and spin-changing collisions could lead to heating and losses. Additionally, spin-polarized fermions do not interact in  $s$ -wave collisions at low temperatures and will therefore not rethermalize during the evaporation. For this reason, the cloud is first transferred to the  $m_F = -9/2$  state in the  $F = 9/2$  manifold using a low-field rf Landau-Zener sweep [138] across the complete hyperfine manifold. Subsequently, the magnetic field is ramped to higher values of approximately 220 G where the quadratic Zeeman shift allows selective addressing of certain  $m_F \rightarrow m_F \pm 1$  transitions by lifting their degeneracy. The cloud is then depolarized using several fast Landau-Zener sweeps across the transition to  $m_F = -7/2$ . Collisions and inhomogeneities are needed to destroy the coherence during the incomplete sweeps and to achieve a balanced mixture.

The  $F = 9/2$  hyperfine manifold of  $^{40}\text{K}$  contains two broad Feshbach resonances for the  $m_F = -9/2, -7/2$  and  $m_F = -9/2, -5/2$  state configurations that are used in this work. The positions have been obtained from literature [139, 140]

configuration	position $B_0$	width $\Delta B$
$m_F = -9/2, -7/2$	202.10(7) G	7.5(1) G
$m_F = -9/2, -5/2$	224.21(5) G	7.6(1) G

Table 4.2: Feshbach resonance parameters used in this work. The table lists position and width of two Feshbach resonances in the  $F = 9/2$  hyperfine manifold of  $^{40}\text{K}$ . The background scattering length is  $a_{\text{bg}} = 174a_0$ .

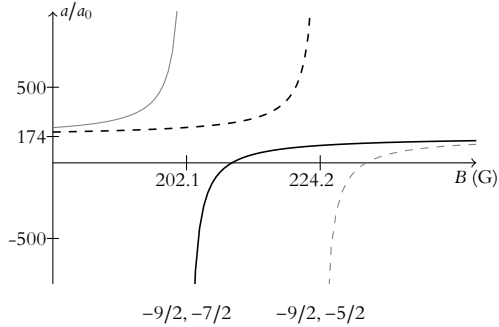


Figure 4.3: The scattering length in the vicinity of the two Feshbach resonances used in this thesis.

while the width was determined within the course of thesis [141] using Bloch oscillations [142]. Their parameters are given in Table 4.2 and a plot of the scattering length in the magnetic field region of interest is shown in Figure 4.3.

These Feshbach resonances are used in different contexts. During evaporation in the dipole trap the proximity to the  $m_F = -9/2, -7/2$  resonance at 202.1 G is used to boost the thermalization of the mixture and between the two spin components. The collision cross section is increased by approaching the resonance from the high field side where the scattering length is large and negative. At a scattering length of  $-1700a_0$  the atoms are able to rethermalize continuously. Evaporation in the dipole trap is then achieved by lowering the trapping potential and letting the hot atoms escape downwards over the potential barrier downwards. The beam powers are decreased in a two-step linear ramp to reach the desired atom number and temperature, and then increased again to stop further loss of atoms.

In order to prepare repulsively interacting atomic samples, the  $m_F = -9/2, -7/2$  Feshbach resonance cannot simply be crossed from the high field side as this would instead lead to molecules. Instead, the  $m_F = -9/2, -5/2$

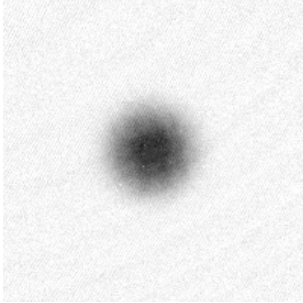


Figure 4.4: Typical absorption image of about  $250 \times 10^3$  atoms after evaporation and release from the dipole trap and 20 ms time-of-flight. The temperature obtained from the momentum distribution is  $T/T_F = 0.13$ .

resonance is used to access repulsive interactions. The  $m_F = -7/2$  atoms are transferred to the  $m_F = -5/2$  state with a Landau-Zener sweep. The sweep is performed by a linear magnetic field ramp at constant rf frequency in the window between the two  $s$ -wave resonances.

By changing the ramp speed and the final trap depth, we can adjust the atom number between  $20 \times 10^3$  and  $400 \times 10^3$ . The temperature in units of the Fermi temperature can be chosen to lie between  $0.08 T_F$  for the coldest clouds and about  $1 T_F$  for the hottest clouds.

### *Optical lattice*

Three mutually perpendicular pairs of retro-reflected laser beams form the optical lattice. The lattice beams are combined with the imaging and with the FORT beams on the two horizontal axes as sketched in Figure 4.5. On the vertical axis only the imaging light is superimposed onto the lattice beam. Collinear propagation of imaging, FORT, and lattice allows for easy alignment of the beams due to the permanent availability of a camera in every direction.

Similar to the FORT beam power, the lattice beam power is controlled in an analog proportional-integral-derivative control loop and the setpoint is provided by an analog output channel from the computer control [121]. Custom shot noise limited photodetectors [143, 144] with a bandwidth above 10 MHz receive about 1% of the trapping light and provide the sensing input to the control loop. Acousto-optical modulators are driven to stabilize the detected light power.

Since the bandwidth of the computer's analog output board is above 1 MHz and much larger than the sampling rate of typically 80 kHz the control signal contains a significant amount of alias frequencies when changed in time. These alias frequencies need to be suppressed to prevent feed-through onto the beam intensities and possible excitation of the atoms. A custom active analog

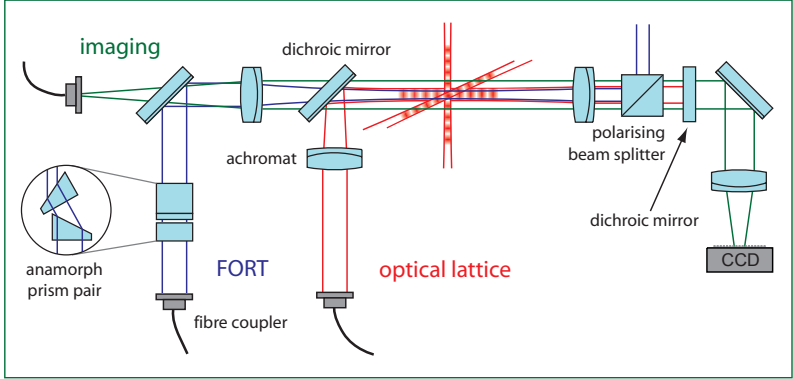


Figure 4.5: Optical setup for dipole trap, lattice, and imaging beams. Imaging, FORT, and lattice beams are extracted from optical fibers, collimated, and shaped. They are combined with dichroic mirrors and focused onto the atoms. Behind the vacuum chamber, spurious reflections of the FORT are suppressed by extracting it with a polarizing beam splitter. The lattice beam is retro-reflected and the imaging beam is directed onto a CCD camera. Mutual interference among FORT and lattice beams from different axes are averaged out by frequency differences of several 40 MHz.

wavelength	$\lambda = 1064 \text{ nm}$
beam waists	$w_{(x,y,z)} = (160, 180, 180) \mu\text{m}$
maximum lattice depth per axis	$V_0 \approx 40E_r$
typical total trap frequencies	$\omega_{(x,y,z)}/2\pi = (49, 53, 133) \text{ Hz}$

Table 4.3: Properties of the optical lattice. Some parameters depend on beam power, alignment, and the overlap of the beams. For a lattice depth of  $7E_r$  the final trap frequencies due to FORT and lattice are given. The envelope of the lattice beams increases the trapping frequencies of the dipole trap especially in the horizontal directions.

fourth-order Chebychev filter in Sallen-Key topology with a corner frequency of 11 kHz attenuates the first alias frequencies at 30 kHz by more than 40 dB.

The optical lattice is characterized by the properties given in Table 4.3. The crucial parameters lattice depth and trapping frequency depend on several alignment parameters and can not be inferred from the beam shape and power with sufficient accuracy.

Two of several possible methods are cross-validated [145] to determine the lattice depth. Both methods use a  $^{87}\text{Rb}$  BEC as its momentum distribution is narrower. Using the first method, a small intensity modulation is added to the lattice beam intensity. The modulation drives transitions between the different

Bloch bands [146] and the resonance for the transfer from the lowest to the first excited even band is located. From this transition frequency, the band structure and the absolute lattice depth are inferred. The alternative method is to subject the BEC to a lattice potential for a very short time in such a way that the atoms are not displaced in the lattice [147]. This regime corresponds to Raman-Nath diffraction in the context of Kapitza-Dirac scattering. The probability to diffract an atom into the  $p = 2n\hbar k$  momentum state is

$$P_n = J_n^2(z), \quad z = \frac{1}{\hbar} \int V(t) dt \quad (4.1)$$

where  $J_n(z)$  is the Bessel function of order  $n$  and  $V(t)$  is the temporal shape of the lattice potential. By recording both the diffraction probabilities and the temporal shapes of the intensity pulses, the lattice depth can be determined to an estimated accuracy of 3%.

For a measurement of the total combined trap frequency of dipole trap and 3D lattice, dipole oscillations are unsuitable due to the effect of the lattice on the oscillation frequency. The effective mass strongly depends on the quasimomentum and would lead to different oscillation frequencies that dephase quickly [148, 149] and prevent an accurate determination of the trap parameters. After measuring the oscillation frequencies in the pure dipole trap  $\omega_{T(x,y,z)}$ , we therefore measure for each 1D standing wave  $i = x, y, z$  the two transverse oscillation frequencies  $\omega_{ij}$ . The total trap frequencies  $\omega_{(x,y,z)}$  are then given as e. g.

$$\omega_x^2 = \omega_{Tx}^2 + (\omega_{yx}^2 - \omega_{Tx}^2) + (\omega_{zx}^2 - \omega_{Tx}^2) = \omega_{yx}^2 + \omega_{zx}^2 - \omega_{Tx}^2. \quad (4.2)$$

This method allows the observation of many oscillation periods and automatically accounts for effects of beam alignment.

Before ramping up the optical lattice potential, the final scattering length is adjusted. Interaction-induced transitions between different many-body states in the lattice often require mass transport which has been shown to be slow for strong interactions [150, 149, 151, 152]. Consequently, a globally adiabatic change of the scattering length in the lattice would require too much time.

The lattice is ramped up smoothly within 100-200 ms to prevent excitations within the band and into higher bands. As the density of states changes significantly, the process must require collisions between the atoms. The need for mass redistribution can also be seen in the single particle states in Figure 3.3 in the previous chapter. As soon as a state reaches the band edge, it becomes expelled from the trap center and localizes in the perimeter. It can therefore be expected that on one hand loading non-interacting clouds into the lattice requires long loading times due to the suppression of collisions. On the other hand, as soon as atoms become localized due to strong interactions, redistribution is slowed down again. In general, the process of loading an ultracold interacting sample

into an optical lattice in a finite time can not be adiabatic and the details have by no means been completely understood.

### *Imaging*

The experimental cycle ends with imaging the atoms. If the magnetic field is kept high then it is preferable to use the cycling  $\sigma^-$ -transition  $|F = 9/2, m_F = -9/2\rangle \rightarrow |F' = 11/2, m'_F = -11/2\rangle$ . At low field, the imaging transition  $|F = 9/2\rangle \rightarrow |F' = 11/2\rangle$  corresponds to “isotropic” polarization [153]. The imaging can be performed in situ in the trap or after release and time-of-flight. Before releasing the atoms, a scattering length is accessed where interactions are minimal and all potentials are ramped down quickly. For vanishing interaction and instantaneous release the spatial atom distribution after long time-of-flight represents a direct image of the original momentum distribution. Interactions — especially during the first stage of expansion when the density is still high — complicate the picture. Absorption images are generally taken in the low saturation regime.

### *Experimental techniques*

#### *High intensity strong saturation imaging*

Quantitative imaging of ultracold atom clouds often suffers from several systematic error sources. Some of these are the not precisely known probe beam polarization, population of the different Zeeman levels in the electronic ground state, and the detailed structure of the excited state. By exploiting the saturation non-linearity, the absorption imaging can be calibrated [154].

The scattering rate of a two-level atom in the presence of monochromatic imaging probe light with intensity  $I$  and a detuning  $\Delta$  from the atomic resonance is given by:

$$R_{\text{sc}} = \frac{\Gamma}{2} \frac{I/I_{\text{sat}}}{1 + 4(\Delta/\Gamma)^2 + I/I_{\text{sat}}}, \quad I_{\text{sat}} = \frac{\pi\hbar c}{3\lambda^3 \tau} \quad (4.3)$$

where  $\tau = 1/\Gamma$  is the radiative lifetime of the excited state,  $\Gamma$  is the linewidth, and  $I_{\text{sat}}$  is the saturation intensity. For the  $^{40}\text{K } D_2$  line, lifetime and saturation intensity are accurately known [155, 156]:  $\tau = 26.37(5)$  ns,  $I_{\text{sat}} = 1.750(3)$  mW/cm<sup>2</sup>.

The scattering and the saturation can also be expressed in terms of an intensity-dependent scattering cross section,

$$\sigma(I) = \frac{\sigma_0}{1 + 4(\Delta/\Gamma)^2 + I/I_{\text{sat}}}, \quad \sigma_0 = \frac{3\lambda^2}{2\pi}. \quad (4.4)$$

If the imaging probe beam passes through an atomic sample with density distribution  $n(z)$  along the propagation direction of the imaging light, the differential

absorption is given by Beer's law,

$$dI = -n(z)\sigma(I)I dz. \quad (4.5)$$

The departure from this two-level description due to the uncertainties mentioned above can be modeled by a decreased effective intensity  $\alpha I_1 = I$  with  $\alpha < 1$  or equivalently an increased saturation intensity  $I_{\text{sat}}, 1/\alpha = I_{\text{sat}}$ . The absorption becomes

$$dI_1 = -n(z)\sigma(\alpha I_1)\alpha I_1 dz. \quad (4.6)$$

After reordering the terms, both sides can be integrated in the usual way:

$$\begin{aligned} \sigma_0 \int n(z) dz &= - \int_{I_{\text{bright}}}^{I_{\text{atoms}}} \frac{1 + 4(\Delta/\Gamma)^2}{\alpha I_1} + \frac{1}{I_{\text{sat}}} dI_1 \\ &= \frac{1 + 4(\Delta/\Gamma)^2}{\alpha} \ln \left( \frac{I_{\text{bright}}}{I_{\text{atoms}}} \right) + \frac{I_{\text{bright}} - I_{\text{atoms}}}{I_{\text{sat}}}. \end{aligned} \quad (4.7)$$

The two intensities  $I_{\text{atoms}}$  and  $I_{\text{bright}}$  are the limits of the intensity integral. They are obtained in each absorption imaging cycle after correction by the background image  $I'_{\text{dark}}$ ,

$$\begin{aligned} I_{\text{atoms}} &= I'_{\text{atoms}} - I'_{\text{dark}}, \\ I_{\text{bright}} &= I'_{\text{bright}} - I'_{\text{dark}}. \end{aligned} \quad (4.8)$$

To determine the two unknown quantities, namely the column density  $\sigma_0 \int n(z) dz$  and the correction factor  $\alpha$ , several images are taken for different intensities under otherwise identical conditions. A linear regression between  $\ln(I_{\text{bright}}/I_{\text{atoms}})$  and  $(I_{\text{bright}} - I_{\text{atoms}})/I_{\text{sat}}$  is performed. The detuning  $\Delta$  can either be measured independently or ignored. In this case its effect is treated as to be simply included in  $\alpha$ .

It is important to note that the correction factor  $\alpha$  and the detuning  $\Delta$  are both taken to be universal and spatially as well as intensity independent. While a variation of  $\alpha$  along the directions perpendicular to the imaging integration axis  $z$  can be accounted for by a pixel-dependent  $\alpha(x, y)$ , several other effects appear more problematic. If the light is non-monochromatic or contains different polarizations that are absorbed differently or not at all,  $\alpha$  or a hypothetical averaged  $\Delta$  will change along the integration direction. Similarly, if the probe light intensity is varied and the pulse time is not changed accordingly to maintain a constant amount of scattered light, the detuning due to an average Doppler shift varies both with imaging intensity and along the integration direction. Optical pumping effects that lead to strong variation and non-universal evolution of the populations in the different states can equally alter the absorption in a non-trivial way. All these effects can lead to a break-down of the above analysis.

Compared to low-saturation absorption imaging, where  $\ln(I_{\text{bright}}/I_{\text{atoms}}) \gg (I_{\text{bright}} - I_{\text{atoms}})/I_{\text{sat}}$ , high-intensity strong saturation imaging depends on good knowledge of absolute intensities. We determine them by explicit calibration of a photodiode that records the shape of the imaging pulse. However, the method does not require any estimate of  $\alpha$ . While commonly  $\alpha = 1$  and low-saturation are assumed, we observe that typical values in our experiments are  $\alpha = 0.7$  which would correspond to a 30% underestimation of the atom number if it was not taken into account.

### *Scattering length calibration*

The first experimental characterizations of the Feshbach resonances used in this work were performed in harmonic traps [157]. In such a setup, the position of a Feshbach resonance  $B_0$  can be accurately determined from the conversion point of atoms to molecules [158, 159, 160]. The transition region of this conversion is usually sufficiently narrow to allow locating the resonance center within 0.05 G. The resonance width  $\Delta B$  is much less accurately known. The width is determined by measuring the transition frequency between Zeeman levels and extracting the mean field shift. From the difference of the mean field shift in the initial state near resonance and the final state where the mean field shift is small, the scattering length and consequently the resonance width are determined [139, 161]. This method is limited by the knowledge of the atomic density in the trap and by the rather broad rf resonance. The reported widths are  $\Delta B = 7.8(6)$  G for the  $m_F = -9/2, -7/2$  resonance and  $9.7(6)$  G for the  $m_F = -9/2, -5/2$  resonance. The systematic uncertainty due to the imprecision in the density is quoted to be another 50%. These uncertainties in the resonance widths directly limit the knowledge of the scattering length and the on-site interaction energy  $U$  in the Hubbard model.

A powerful method to characterize a Feshbach resonance is the observation of Bloch oscillations in the lattice. If non-interacting atoms with quasimomentum states  $q$  are subjected to a constant force  $F = \hbar \dot{q}$ , their oscillation is confined to the first Brillouin zone due to the anticrossing of the dispersion at the band edge and the corresponding periodicity of the quasimomentum. At vanishing interaction these oscillations can be sustained for many thousand cycles [142]. A small amount of interactions, however, already leads to collisions and to the dephasing of oscillations of different atoms.

It is necessary to limit the filling in the band since the fermionic nature of the atoms would otherwise lead to a complete occupation of the entire Brillouin zone and hence prevent the observation of Bloch oscillations. In order to locate the zero crossing, the atoms are allowed to oscillate for up to 750 ms so that after the oscillation they are left either at the band edge or at the band center. Choosing a final position at the band edge corresponds to the largest root mean



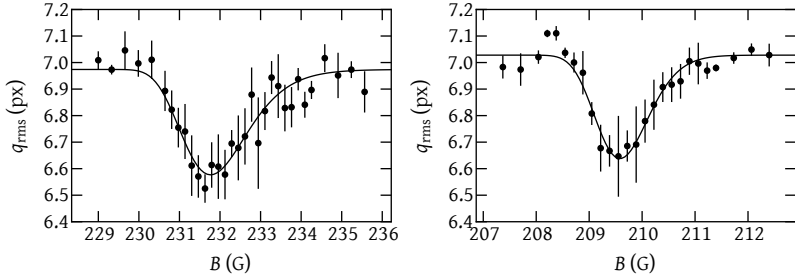


Figure 4.6: Suppressed dephasing of Bloch oscillations at the zero crossing of the scattering length. In the  $m_F = -9/2, -5/2$  (left) and  $m_F = -9/2, -7/2$  (right) mixtures the root-mean-square momentum width  $q_{\text{rms}}$  in units of camera pixels exhibits a characteristic dip when interactions vanish at the zero crossing of the scattering length.

square momentum spread for  $a = 0$  while a final position in the band center corresponds to the smallest rms momentum. In the subsequent time-of-flight expansion, the quasimomentum distribution is mapped to position and finally recorded in an absorption image. Using the known values for the resonance position  $B_0$  and the background scattering length  $a_{\text{bg}}$ , we fit a gaussian dip to the rms momentum width:

$$q_{\text{rms}}(B) = q_0 + \Delta q \exp\left(-\frac{1}{2} \left(\frac{a_{\text{bg}}}{\Delta a}\right)^2 \left(1 - \frac{\Delta B}{B - B_0}\right)^2\right). \quad (4.9)$$

The four remaining parameters are determined by the fit:  $q_0$  the rms momentum for dephased oscillations,  $\Delta q$  the maximum change in rms momentum without interactions,  $\Delta a$  the width of the low dephasing region around  $a = 0$ , and  $\Delta B$  the width of the Feshbach resonance. An example of such a dephasing measurement is reproduced in Figure 4.6. We obtain a width of 7.5(1) G for the  $m_F = -9/2, -7/2$  resonance at 202.1 G and 7.6(1) G for the  $m_F = -9/2, -5/2$  resonance at 224.21(5) G. The accuracy is limited by the magnetic field calibration, the uncertainty in the resonance position, and the width of the dip. These experiments represent the first observation of Bloch oscillations of interacting Fermions.

### *Thermometry in the dipole trap*

Two different approaches have turned out to be suitable to determine the temperature in the dipole trap. On one hand, the momentum distribution and its sharp Fermi edge can serve as a thermometer for weakly interacting Fermi

gases [162]. The phase space density, on the other hand, is also intimately related to the temperature and can be inferred from the efficiency in adiabatically associating Feshbach molecules [163].

By fitting the momentum distribution after time-of-flight to absorption images such as Figure 4.4, the fugacity  $z$  and the corresponding temperature can be obtained. We employ this method predominantly in the case of  $m_F = -9/2$  spin-polarized gases, for mixtures at small interactions and for high-field imaging of the  $m_F = -9/2$  spin component. In the  $m_F = -9/2, -7/2$  mixture on the right side of the Feshbach resonance, we routinely achieve temperatures between  $0.05 T_F$  and  $0.1 T_F$  in terms of the Fermi temperature  $T_F$ . This configuration is also advantageous as the scattering length can be driven to zero on the right side of the resonance. In the  $m_F = -9/2, -5/2$  mixture on the left side of the resonance, the temperature is slightly higher at about 0.1 to 0.15  $T_F$ . Here the scattering length is always above the background scattering length. The minimal amount of interactions present on the left side of the resonance changes the apparent temperature by less than 3% of the Fermi temperature.

The momentum distribution of highly degenerate Fermions in time-of-flight is typically more difficult to analyze than the momentum distribution of Bosons. While non-interacting Bosons approach a very small rms momentum which is only limited by the harmonic oscillator ground state, in a fermionic gas even in the absolute ground state, momenta as large as the Fermi momentum are occupied. Detecting the small excess momentum which corresponds to departures from  $T = 0$  is therefore much easier in Bosons than in Fermions due to the large background momentum of the Fermi gas. Very small occupation changes at the Fermi edge need to be detected reliably. A least squares fit to the momentum distribution of degenerate Fermions in time-of-flight absorption images is especially sensitive to the sharpness of the edges of the cloud which are furthermore of low optical density.

A Monte-Carlo simulation was performed to assess the influence of technical noise on the reliability of the temperature determination. The results are reproduced in Figure 4.7 and show that certain types of technical imperfections are highly detrimental while others are benign. Smoothing of the image that could be due to imperfect focusing leads to a systematic increase of the apparent temperature. This is expected since it broadens the Fermi edge. Its error, however, is systematically underestimated by the fit. Noise on the pixel length scale which is smaller than the edge width is rather benign and is also correctly accounted for by the fit's uncertainty in the temperature. A typical source of pixel scale noise is the electronic readout and dark current noise or the photon shot noise in the imaging beam. Multiplicative noise on larger length scales of about a third of the cloud radius is dangerous. Its influence is frequently underestimated as it is not accounted for by the uncertainty of the fit result and can lead to a systematic error in the obtained temperature. Optical fringes in the imaging light being

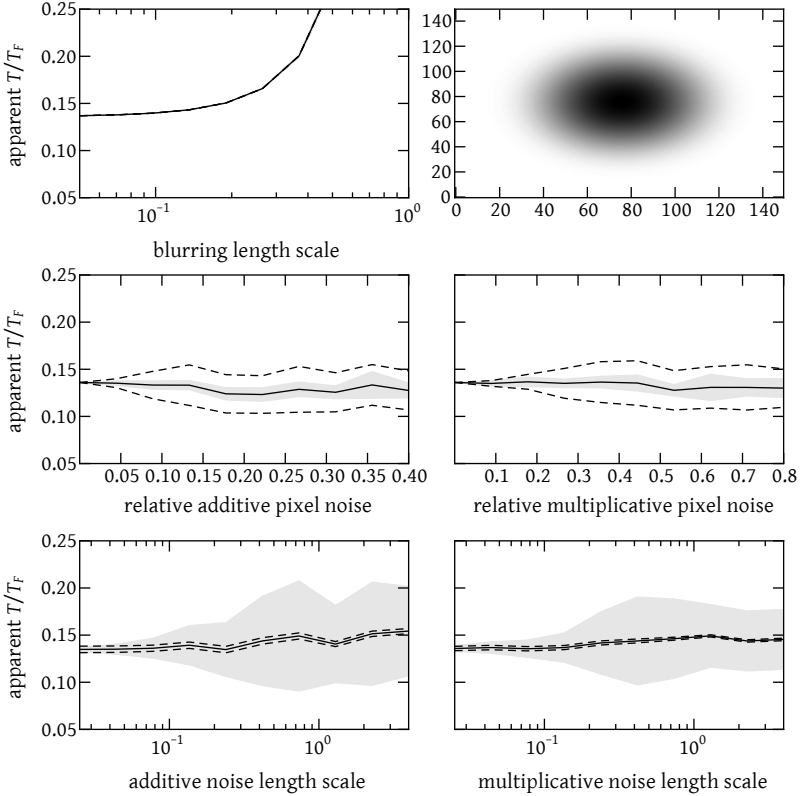


Figure 4.7: Sensitivity of the temperature determination in time-of-flight to noise sources and imprecisions. An absorption image of an ultracold fermionic atom cloud is synthesized with known parameters corresponding to typical experimental conditions (top right panel). Four different parametric noise sources and the blurring due to imperfections in the imaging could lead to departures (line in each plot) from the actual temperature of  $T/T_F = 0.136$ . The standard deviation of the fit results is shown as a gray corridor and the mean fit error of the apparent temperature as dashed lines. The different sources of imperfections are from top left to bottom right: (a) a gaussian blurring of the image on varying length scales, (b) spatially uncorrelated additive noise where each pixel receives a random shift, (b) multiplicative noise, (c) 3.5% additive noise with varying length scale, (d) 7% multiplicative noise with varying length scale. The additive noise is scaled by the maximum density signal in the image in the center of the cloud. All length scales are given in units of the cloud radius.

difficult to remove are typically of this size. In the case of 3.5% additive or 7% multiplicative noise they lead to an error of  $0.05 T_F$  in the temperature.

The formation of molecules can be used as an alternative thermometry method on the attractive side of the Feshbach resonance. A good measure for the phase space density can be obtained by ramping across the resonance and thereby associating atom pairs to molecules. If the ramp is adiabatic, atoms within a phase space volume of  $\delta v \delta p < \gamma \hbar$  are associated. The rest remains unpaired. Here  $\gamma$  parametrizes the pairing and is comparable to unity [163]. In order to associate the atoms, the magnetic field is adiabatically swept from the attractive side of the resonance at 202.8 G to the molecular side at 200.8 G adiabatically in 5 ms. The molecules are then bound deeper and made non-absorbing for the imaging light by fully switching off the magnetic field and imaging the remaining atoms. A conservative lower estimate for the total paired fraction is obtained by comparing the number of unpaired atoms with images where the molecules were dissociated adiabatically before imaging. From at least three such image pairs we infer the fraction of molecules that were formed. We routinely achieve molecule fractions of about 85% which correspond to temperatures below  $0.1 T_F$ .

### *Double occupancy*

The double occupancy is a sensitive indicator for the properties of a Fermion sample in an optical lattice. It can be directly related to the amount of thermal excitations for non-interacting [80] as well as for correlated systems [79]. Additionally, at low temperatures where antiferromagnetic order is expected to set in, the double occupancy signals the redistribution of entropy from the spin configuration to the charge correlation [111]. A reliable experimental protocol to detect double occupancies enables access to these properties. In this section, our implementation of two methods is presented.

A straight forward approach is to slightly adapt the thermometry method in the dipole trap which was described in the previous section. A  $m_F = -9/2, -7/2$  spin mixture is prepared at a scattering length on the right side of the Feshbach resonance. Then, atoms on lattice sites that are occupied with an  $m_F = -9/2$  and an  $m_F = -7/2$  atom are converted into molecules. The remaining atoms as well as the total atom number are counted in two realizations of the experiment. The adiabaticity condition that needs to be met to form molecules with near unit efficiency requires ramp times of several milli-seconds. As this is already comparable to the tunneling rate in typical lattices, a redistribution of atoms during the ramp across the Feshbach resonance has to be prevented. This suppression of tunneling is achieved by quickly increasing the lattice depth to some  $30 E_r$  within  $500 \mu\text{s}$ . The deeper lattice potential leads to a strong localization of the atomic wavefunctions and to a reduction of the tunneling rate to below

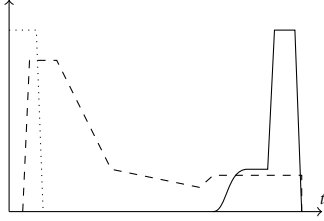


Figure 4.8: Cooling, lattice loading, and freezing procedure. The time dependence of the potential depths of the QUIC trap (dotted), the FORT (dashed), and the optical lattice (solid) are shown schematically (not to scale).

2 Hz which is much longer than the experimental timescale. The ramp speed is chosen low enough to prevent the excitation of atoms into higher bands where they would not bind. Subsequently, atom pairs on doubly occupied sites can be adiabatically converted into molecules. A timing sketch of the evolution of the potential depths is provided in Figure 4.8.

This method of measuring the double occupancy is experimentally disfavored for two reasons: It requires two consecutive experimental cycles per data point and is therefore sensitive to atom number drifts. Furthermore, resolving small double occupancies corresponds to detecting changes in the number of unpaired atoms. As this is a small signal on a large background, it suffers from noise.

The second method we have implemented is significantly more versatile. It is effective on the attractive side of the resonances as well as on the repulsive side and relies on rf transitions [17] between molecular states on one resonance and repulsive states on the other.

The scheme is depicted in Figure 4.9. In the window between the two  $s$ -wave Feshbach resonances at 202 G and 224 G we prepare either a  $m_F = -9/2, -5/2$  mixture on the low field side of their Feshbach resonance with repulsive interactions and  $a > a_{\text{bg}}$  or a  $m_F = -9/2, -7/2$  mixture on the high-field branch of the resonance with  $a < a_{\text{bg}}$ . The mixture is loaded into the lattice and the desired experiment is performed. To determine the double occupancy, the atomic density distribution is stabilized by increasing the lattice depth to  $30 E_r$  as for the adiabatic molecule formation. Then a magnetic field of 201.3 G on the low field side of the  $m_F = -9/2, -7/2$  resonance is accessed. In the case of a  $m_F = -9/2, -7/2$  mixture, atoms on doubly occupied sites are converted into molecules during this ramp. Their binding energy amounts to  $\delta v_{-7/2} \approx -110$  kHz. At this point, atoms in the other mixture have a weakly repulsive scattering length and a positive interaction energy of  $\delta v_{-5/2} \sim 10$  kHz. The bare transition frequency of an atom on a singly occupied site between the Zeeman levels  $m_F = -7/2$  and  $-5/2$  amounts to  $\nu_{\text{single}} = 47.072$  MHz at this magnetic field. On a doubly occupied site the transition is shifted to  $\nu_{\text{double}} = \nu_{\text{single}} - \delta v_{-7/2} + \delta v_{-5/2}$ .

By driving a rf  $\pi$  pulse with a frequency of  $\nu_{\text{double}}$  in the  $m_F = -9/2, -7/2$  ( $m_F = -9/2, -5/2$ ) mixture, the  $m_F = -7/2$  ( $-5/2$ ) atoms on doubly occupied

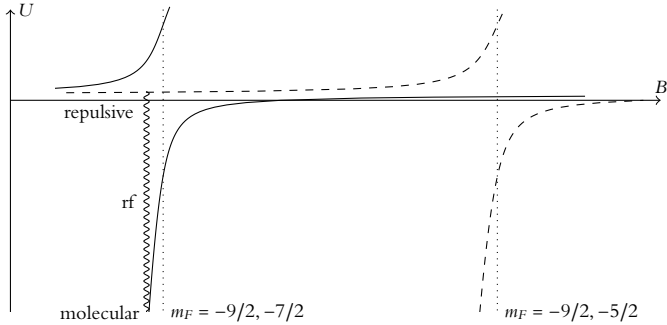


Figure 4.9: On-site energy in an optical lattice and rf spectroscopy. In the two spin mixtures, the interaction energy of an atom pair on a lattice site depends on magnetic field and spin configuration. The energy difference between the bound state on the left side of the  $m_F = -9/2, -7/2$  resonance (solid) and the weakly repulsive unbound state on the left side of the  $m_F = -9/2, -5/2$  resonance (dashed) allows selectively addressing double occupancies with rf pulses (coiled).

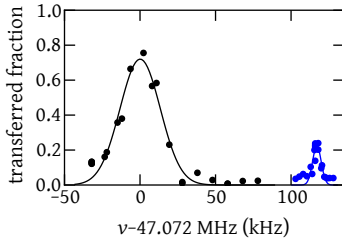


Figure 4.10: Radio frequency spectrum of an interacting  $m_F = -9/2, -5/2$  Fermi mixture in the lattice. The left peak corresponds to singly occupied sites and a  $\pi$ -pulse time of  $35 \mu\text{s}$  while the right peak has been recorded for a  $\pi$ -pulse duration of  $130 \mu\text{s}$  on the transition frequency of doubly occupied sites.

sites are selectively transferred to the  $m_F = -5/2$  ( $-7/2$ ) state. After the pulse, the molecules are dissociated again by ramping to the right side of the Feshbach resonance. Alternatively, we drive the  $v_{\text{single}}$  transition and flip the  $-7/2$  ( $-5/2$ ) atoms on singly occupied sites. The  $m_F = -9/2$  component is not altered and serves as a reference to confirm the total atom number  $N_{-9/2} = N_{-7/2} + N_{-5/2}$  which is conserved throughout the rf spectroscopy. For our experimental conditions a  $\pi$  pulse for the spin flip takes  $130 \mu\text{s}$  on doubly occupied sites and  $35 \mu\text{s}$  on singly occupied sites due to the different Franck–Condon factors. The envelopes of the rf pulses are electronically shaped to limit their bandwidth. A comparison of the two rf spectroscopy peaks of the transition on singly and doubly occupied sites is provided in Figure 4.10.

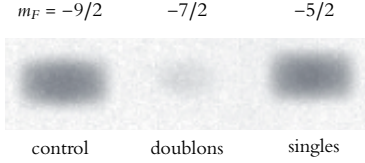


Figure 4.11: Absorption image after double rf spectroscopy, Stern-Gerlach spin separation and time-of-flight.

After the rf spectroscopy, the optical lattice and magnetic field are ramped down in 10 ms. Then, the FORT is turned off and the three spin components expand during 6 ms time-of-flight. Using a magnetic field gradient during the first 2 ms, the three components receive different additional accelerations depending on their spin, analogous to the Stern-Gerlach experiment.

Figure 4.11 shows a typical absorption image of a cloud released from the lattice. The system was initially a repulsively interacting  $m_F = -9/2, -5/2$  mixture with a double occupancy of about 10%. The three spin components can be clearly identified. They correspond to the  $-9/2$  total atom number control population, the  $-7/2$  component which were  $-5/2$  atoms on doubly occupied sites, and finally the unaltered  $-5/2$  atoms on singly occupied sites. The magnetic field and the gradient during the time-of-flight point both along the horizontal direction. Due to the relatively short time-of-flight  $t_{\text{tof}} \sim 1/\omega$ , the shape of the clouds reflects a mixture of both, the horizontally elongated ellipsoidal spatial shape of the cloud in the trap and the square momentum shape of the first Brillouin zone.

Due to a reproducible change of the imaging beam profile between the atomic absorption image and the subsequent reference image without atoms, residual structures are present in the density profiles. These are reduced by repeating the entire experiment without loading atoms and subtracting the obtained residual density distribution from the atomic density distribution. The number of atoms  $N_{m_F}$  per spin component  $m_F$  is determined from the 2D column density by simultaneously fitting the sum of three quartic terms

$$A \cdot \max\left(1 - \left(\frac{x}{w_x}\right)^4, 0\right) \cdot \max\left(1 - \left(\frac{y}{w_y}\right)^4, 0\right) \quad (4.10)$$

with identical widths  $w_{x,y}$  and mutual distances. This permits accurate detection of atom numbers down to 200 atoms per spin state. We have validated the absolute accuracy of the fits against integration of the density. The fraction  $D$  of atoms residing on doubly occupied sites is defined as

$$D = 2N_{m_F^*}/N \quad (4.11)$$

where  $N = N_{-9/2} + N_{-7/2} + N_{-5/2}$  and  $m'_F = -5/2$  ( $-7/2$ ) for samples initially containing atoms in the  $-7/2$  ( $-5/2$ ) states, respectively.

We calibrated this method against adiabatic molecule formation for double occupancies near 60% and found good agreement to within 10%. Therefore, rf spectroscopy is now the method of choice for precision measurements of the double occupancy. It allows accurate determination of total atom number as well as single and double occupancy in a single shot, making it insensitive to drifts. Rf spectroscopy allows for a significant reduction of the error of double occupancy down to 1% since it is a zero-background technique both for very high and very low double occupancy. The development of this technique was essential for the experiments presented the subsequent chapters.



## 5 Exploring the Mott insulator

In a solid material strong interactions between the electrons can lead to surprising properties. A prime example is the Mott insulator, where the suppression of conductivity is a result of interactions and not the consequence of a filled Bloch band [165]. The proximity to the Mott-insulating phase in fermionic systems is the origin for many intriguing phenomena in condensed matter physics [166], most notably high-temperature superconductivity [40]. Therefore, it is highly desirable to use the novel experimental tools developed in atomic physics to access this regime. The previous chapters have shown that the Hubbard model [8], which encompasses the essential physics of the Mott insulator, also applies to quantum gases trapped in an optical lattice [3]. However, the Mott-insulating regime could initially only be reached with a gas of bosons [15], lacking the rich and peculiar nature of fermions. This chapter reports on the formation of a Mott insulator of a repulsively interacting two-component Fermi gas in an optical lattice.

Different experimental approaches are chosen to detect three characteristic features of a Mott-insulating phase:

- Under the influence of strong repulsion the double occupancy of sites with both a spin-up atom and a spin-down atom is suppressed to extremely small values compared to the non-interacting case.
- The compressibility of the system is strongly reduced. Even as a response to a large increase in chemical potential, the system does not react with an increase of the density and the maximum occupancy remains close to unity.
- In the excitation spectrum, a new gapped mode emerges at the on-site interaction energy. It is clearly separated from the energy scales of the lowest Bloch band. The mode corresponds to the selective excitation of double occupancies.

### *The metal insulator transition in a trap*

The Hubbard model assumes a single static energy band for the electrons and on-site interactions. Spin-up and spin-down fermions are moving on a lattice and

---

Parts of this chapter have been published in [164]

interact when occupying the same lattice site. According to the Pauli principle, in the lowest Bloch band, fermionic particles with equal spin cannot occupy the same site. The consequence of strong repulsive interactions is that also fermions in different spin states tend to avoid each other. In the case of a half filled band the particles get localized and an incompressible state with one fermion per site forms. Since no symmetry is broken, the transition between the metallic and the Mott-insulating regime at finite temperature exhibits a smooth crossover rather than a sharp phase transition at well defined parameters.

In optical lattice experiments the presence of an underlying harmonic trapping potential has an important influence on the observable physics. Let us first consider a zero temperature Fermi gas prepared in an equal mixture of two non-interacting spin components. All available single particle quantum states will be filled up to the Fermi energy and, for a sufficiently large number of trapped atoms, a band insulating region with two atoms per site appears in the trap center, surrounded by a metallic shell with decreasing filling, see Figure 5.1. An important quantity to characterize the state of the system is the fraction  $D = 2 \sum_i \langle n_{\uparrow} n_{\downarrow} \rangle / N$  of atoms residing on lattice sites which are occupied by two atoms, one from each component. For the non-interacting case this double occupancy should increase in a continuous fashion with the number  $N = \sum_i \langle n_{\uparrow} + n_{\downarrow} \rangle$  of atoms in the trap.

A very different scenario can be anticipated for a gas with increasingly strong repulsive interactions. A Mott insulator will appear, at first in those regions of the trap where the local filling is approximately one atom per site. For very strong repulsion the entire center of the trap contains a Mott insulating phase and double occupancy is suppressed, see Figure 5.1. Since the Mott-insulating region is incompressible [39, 167], the suppression of double occupancy should be robust against a tightening of the trapping potential, or equivalently, against an increase in the number of trapped atoms. However, once the chemical potential  $\mu$  reaches a level where double occupation of sites becomes favorable, a metallic phase appears in the center and the double occupancy increases accordingly. The energy spectrum in the Mott-insulating phase is gapped, with a finite energy cost required to bring two atoms onto the same lattice site. This energy has to be large compared to the temperature in order to keep the number of thermally excited doubly occupied sites small. Thermally excited holes in the center are suppressed by the chemical potential  $\mu$ .

### *Experimental methods*

Our experiment is performed with a quantum degenerate gas of fermionic  $^{40}\text{K}$  atoms, prepared in a balanced mixture of two magnetic sublevels of the  $F = 9/2$  hyperfine manifold. The Feshbach resonances allow us to tune the  $s$ -wave

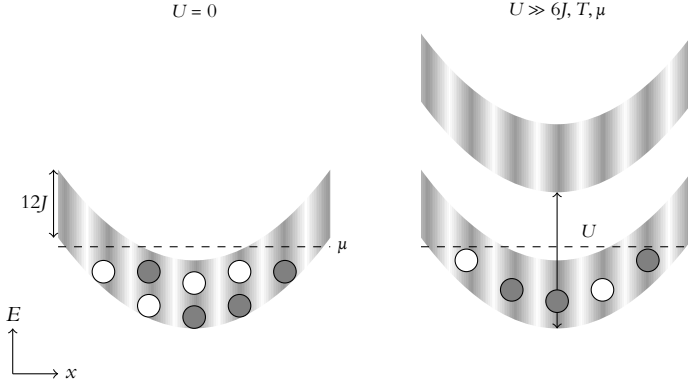


Figure 5.1: Energy spectrum of a Fermi gas in an optical lattice with an underlying confining potential. In the non-interacting case (left) the curvature of the lowest Bloch band reflects the harmonic confinement. At zero temperature all states up to the chemical potential  $\mu$  are filled with atoms of both spin states. In the Mott-insulating limit (right) the energy cost for creating doubly occupied sites greatly exceeds the temperature  $T$  and the kinetic energy parametrized by  $J$ , giving rise to a gap of order  $U$ . The energy spectrum of single particle excitations is then depicted by two Hubbard bands. Doubly occupied sites correspond to atoms in the upper Hubbard band.

scattering length between  $a = 240(4)a_0$  and  $810(40)a_0$  as well as to prepare non-interacting samples. The two-component Fermi gas is subjected to the potential of a three-dimensional optical lattice of simple cubic symmetry. The lattice potential depth  $V_0$  is chosen between  $6.5$  and  $12E_R$ . The system is described by the Hubbard Hamiltonian. In this chapter the nearest neighbor tunneling matrix element is parametrized by  $J$  and not by  $t$  owing to the historical provenance of Mott physics with ultracold atoms from Bosonic systems [4, 3]. The quotient  $U/6J$  which characterizes the ratio between interaction and kinetic energy can be tuned from zero to a maximum value of 30.

### Preparation

After sympathetic cooling with  $^{87}\text{Rb}$ ,  $2 \times 10^6$  fermionic  $^{40}\text{K}$  atoms are transferred into a dipole trap. Initially, a balanced spin mixture of atoms in the  $|m_F\rangle = |-9/2\rangle$  and  $|-7/2\rangle$  states is prepared and evaporatively cooled at a magnetic bias field of 203.06 G. Using this mixture we realize non-interacting samples with a scattering length of  $a = 0(10)a_0$ . Repulsive interactions are obtained by transferring the atoms in the  $|-7/2\rangle$  state to the  $|-5/2\rangle$  state during the evaporation, thus cooling and preparing a spin mixture of atoms in  $|-9/2\rangle$  and  $|-5/2\rangle$  states, close

to a Feshbach resonance at 224.21 G [159]. After tuning the scattering length to the desired value we load the atoms into the lowest Bloch band of the optical lattice by increasing the intensity of three retroreflected laser beams within 200 ms using a spline ramp. For a given scattering length and lattice depth  $J$  and  $U$  are inferred from the Wannier functions including the interaction induced coupling to the second Bloch band. The latter leads to corrections of up to 15% with respect to the single band model.

### *Temperature*

The temperature is measured in the harmonic dipole trap before ramping up the lattice and after a subsequent reversed ramp back into the dipole trap. The highest temperatures measured before and after ramping are  $T_i = 0.15T_F$  and  $T_f = 0.24T_F$ , respectively. Since we expect non-adiabatic heating to occur during the lattice ramp up as well as during ramp down, we use the mean value of  $0.195T_F$  as a realistic estimate. The reported temperatures represent upper limits, since we have achieved temperatures down to  $0.08T_F$  in the dipole trap prior to loading.

### *Radio-frequency spectroscopy*

In order to characterize the state of the Fermi gas in the optical lattice, we use rf spectroscopy to measure the fraction  $D$  of atoms residing on doubly occupied sites with a precision of down to 1%. By increasing the depth of the optical lattice to  $30E_R$  in 0.5 ms tunneling is suppressed. In the next step, we shift the energy of atoms on doubly occupied sites by approaching a Feshbach resonance. The magnetic field is tuned to 201.28 G, where a molecular state for a  $|-9/2\rangle$ ,  $|-7/2\rangle$  pair with binding energy  $h \times 99(1)$  kHz and a weakly interacting state for a  $|-9/2\rangle$ ,  $|-5/2\rangle$  pair exist [17]. This enables us to specifically address only atoms on doubly occupied sites by using a radio frequency pulse to transfer one of the spin components to a third, previously unpopulated magnetic sublevel. The radio-frequency  $\pi$ -pulse dissociates (associates) pairs and changes the spin state of those  $|-7/2\rangle$  ( $|-5/2\rangle$ ) atoms that share a site with a  $|-9/2\rangle$  atom. Finally the magnetic field is increased to 202.80 G dissociating any molecules and the lattice potential is ramped down in 10 ms. All confining potentials are switched off and the homogeneous magnetic bias field is replaced by a magnetic gradient field, thus spatially separating the spin states. After 6 ms of time-of-flight all three clouds are imaged simultaneously and the atom numbers in the three spin components are determined.

We estimate the relative systematic error for the total number  $N$  of atoms in all spin components to be less than 20%. The  $|-9/2\rangle$ ,  $|-5/2\rangle$  mixture shows an

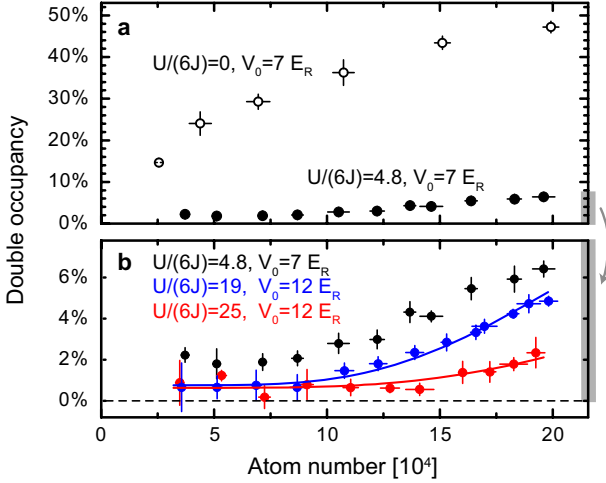


Figure 5.2: Double occupancy in the non-interacting and Mott-insulating regime. (a) A significant increase of the double occupancy with atom number is observed in the non-interacting regime (empty circles) whereas on entering the Mott-insulating regime the double occupancy is suppressed (filled circles). The corresponding onsite interaction strengths are  $U/h = 0(80)$  Hz and  $U/h = 5.0(6)$  kHz. (b) In the Mott-insulating regime the double occupancy is strongly suppressed. It starts to increase for large atom numbers indicating the formation of a metallic region of double occupancies on a Mott-insulating background in the trap center. The curves represent the theoretical expectation for  $D$  in the atomic limit. Values and error bars are the mean and the standard deviation of 4 to 8 identical measurements.

offset of 0.5% in  $D$  due to  $|-7/2\rangle$  atoms remaining from the initial spin transfer during evaporation.

Due to inelastic collisions we lose at most 4.8(6)% of the atoms during the preparation of the Mott-insulating state for the parameters above, where the losses are expected to be highest. The inelastic decay time for atoms on doubly occupied sites exceeds 850 ms, which is significantly longer than the relevant experimental timescale.

### Suppression of double occupancy

The double occupancy as a function of total atom number is plotted in Figure 5.2a, where the non-interacting situation is compared to the case of strong repulsive interactions. The former shows the expected rapid increase of double occupancy with atom number. A strikingly different behavior is observed in the

strongly repulsive regime with  $U \gg J, T, \mu$ , where a Mott insulator is expected. The double occupancy is strongly reduced to values systematically below 2% for small atom numbers. This is direct evidence for the suppression of fluctuations in the occupation number and for the localization of the atoms.

### Compressibility

The compressibility  $\kappa = \partial n / \partial \mu$  is a clear indicator for Mott-insulating behavior in a homogeneous system. It vanishes if the chemical potential is located between the two Hubbard bands,  $\mu = U/2$ , see Figure 5.3. Changes in the chemical potentials do not allow holes nor double occupancies to enter the system as  $\mu \gg 6J$  and  $\mu \ll U - 6J$ . The density is constant over a wide range. In a trapped system however, there are always large regions of low local chemical potential in the perimeter of the cloud where the density is low and the compressibility is dominated solely by the hole compressibility in the lower Hubbard band. Averaging the compressibility over the entire cloud therefore washes out all signatures of a Mott insulating core due to the constant large compressibility of the edges [116].

An alternative measure that has been proposed as an indicator for incompressibility is the cloud radius [64] which is the root mean square of the distance from the cloud center averaged over the density  $R^2 = \sum_i r^2 \langle n_i + n_{\bar{i}} \rangle / N$ . Similar to the total compressibility, the cloud radius is also bound to be dominated by edge effects in regions that are irrelevant to Mott-insulating behavior of the core. It can therefore only show weak signs of an incompressible core.

In order to experimentally investigate the compressibility on entering the Mott-insulating regime we determine how the double occupancy changes with increasing atom number. From these data we develop a robust measure for the compressibility that is insensitive to edge effects.

In the trapped system we define the number of doubly occupied sites  $D' = \sum_i \langle n_i n_{\bar{i}} \rangle = DN/2$  and the core compressibility  $\kappa_C$  analogously to the total compressibility  $\kappa$

$$\kappa_C = \frac{1}{N} \frac{\partial D'}{\partial \mu} = \frac{1}{N} \sum_i \kappa_{Ci} \quad (5.1)$$

$$\kappa = \frac{1}{N} \frac{\partial N}{\partial \mu} = \frac{1}{N} \sum_i \kappa_i. \quad (5.2)$$

In a homogeneous system, the core compressibility can be shown to be identical to the actual compressibility if the chemical potential is above the lower Hubbard band [116], see also Figure 5.3. However, it is insensitive to low chemical potentials and even vanishes entirely if the density is below half filling. This makes the quantity an excellent probe for the compressibility of the core

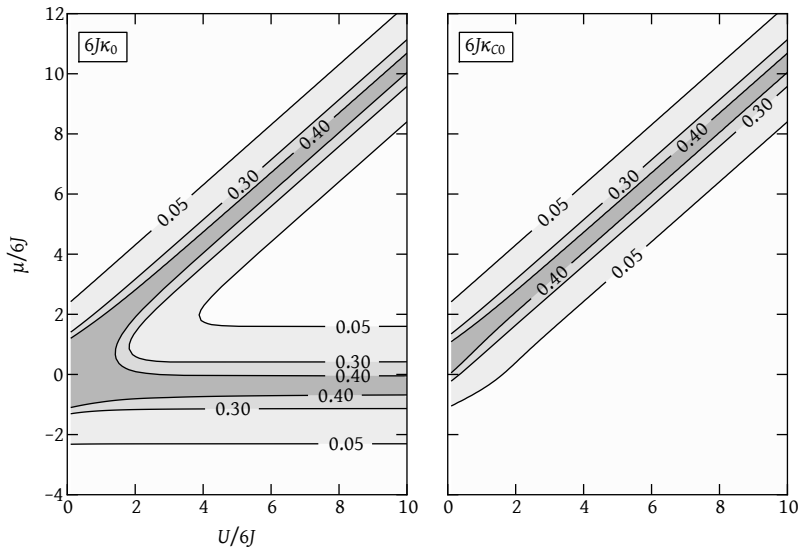


Figure 5.3: Comparison of core compressibility  $\kappa_{C0}$  and compressibility  $\kappa_0$  in a homogeneous system for  $T/6J = 3$  in second order high temperature series. The subscript  $(\cdot)_0$  indicates the reference to the homogeneous system. To characterize the compressibility of a trapped Fermi gas in an optical lattice, the core compressibility  $N\kappa_C = \partial D'/\partial\mu$  is much better suited than the compressibility  $N\kappa = \partial N/\partial\mu$ . It effectively excludes the contribution of the otherwise dominant regions of small chemical potential in the perimeter while still equaling the actual compressibility in the core where  $\mu \gg 6J$ .

region in a trapped system, since it excludes the influence of to the low density edges of the system.

Compressibility and core compressibility are related by the ratio

$$\frac{\kappa_C}{\kappa} = \frac{\partial D'}{\partial\mu} \frac{\partial\mu}{\partial N} = \frac{\partial D'}{\partial N}. \quad (5.3)$$

This core compressibility ratio is experimentally advantageous as it does not require knowledge of the chemical potential and can be measured directly and accurately. It inherits the features of the core compressibility: when averaging over the different chemical potentials present in the system, the  $\kappa_C$  deviates only from zero as soon as the upper Hubbard band contributes to the total compressibility and starts to become filled. The total compressibility  $\kappa$  stays large and approximately constant independent of the interaction strength and the presence of a Mott core.

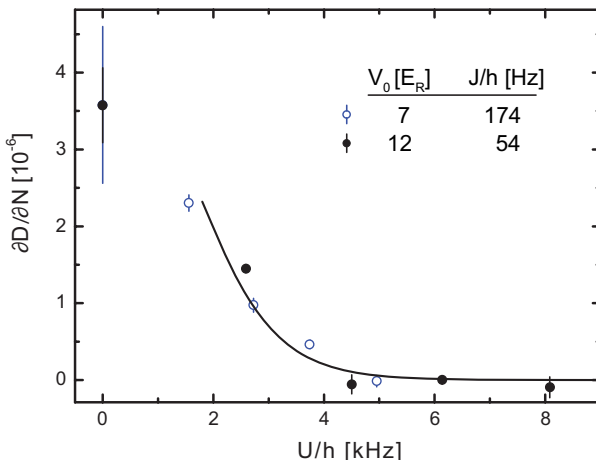


Figure 5.4: The transition to an incompressible sample. Upon changing  $U$ , two regimes can be distinguished by the slope  $\partial D/\partial N$ . For vanishing interaction the large initial slope signals the filling of the Bloch band. Increasing  $U$  reduces the double occupancy. For  $U/h \gtrsim 5$  kHz a change in atom number can no longer change the double occupancy. The compressibility  $\partial D/\partial N$  is obtained from a least squares fit of  $D(N) = (\partial D/\partial N)N + D_0$  to data such as those shown in Figure 5.2, with atom numbers in the interval from  $25 \times 10^3$  to  $8 \times 10^4$ . Error bars denote the confidence interval of the fit. The expected slope in the atomic limit is illustrated with a line for a lattice depth of  $12E_R$  and  $T = 0.28T_F$ .

In terms of the fraction of atoms on doubly occupied sites  $D = 2D'/N$ , the core compressibility ratio is

$$\frac{\partial D}{\partial N} = \frac{2}{N} \frac{\partial D'}{\partial N} - \frac{D'}{N^2} = \frac{2\kappa_C}{N\kappa} - \frac{D}{2N}. \quad (5.4)$$

The last term is negligible as long as the double occupancy is small. A vanishing slope  $\partial D/\partial N$  is thus equivalent to a vanishing core compressibility and is evidence of a Mott-insulating phase in the center of the trap.

We estimate the filling in the trap center for the non-interacting case from the measured double occupancy [80]. It significantly exceeds one atom per site,  $\langle n \rangle = 1.4$  for  $N = 5 \times 10^4$ ,  $V_0 = 7E_R$  and a temperature  $T$  of 30% of the Fermi temperature  $T_F$ . Consequently, already for vanishing interaction, the chemical potential is large enough to permit the use of the core compressibility ratio,  $\mu \gg 6J$ . Finite interactions can only increase the chemical potential.

We extract the slope  $\partial D/\partial N$  from curves such as shown in Figure 5.2. It is displayed in Figure 5.4 for a wide range of interaction strengths. The data



shows that we access two regimes: For small onsite interaction energies  $U$  the slope  $\partial D/\partial N$  is positive and the system is compressible. Yet for  $U/h > 5$  kHz the measured compressibility vanishes. This indicates that we have entered the Mott insulating regime. It implies a large central region with a filling reduced to one atom per site, surrounded by a metallic region with lower filling.

### *The atomic limit*

Further insight is gained by comparing our measurements with the theoretical values of  $\partial D/\partial N$  calculated in the atomic limit [168] of the Hubbard model, including confinement and finite temperature. In this limit the kinetic energy is neglected by setting the tunneling matrix element  $J$  to zero.

We calculate the temperature in the lattice by assuming that this entropy is the same as the entropy determined from temperature measurements in the dipole trap. The fits in Figure 5.2b involve  $U$  as determined by modulation spectroscopy (see the following section,  $U/h = 4.7(1)$  kHz and  $6.1(1)$  kHz) since band structure calculations disagree with the measured value by up to 30% for the largest scattering lengths.

We find good agreement between theory (line in Figure 5.4) and experimental data for  $U \gg 6J$ , where the atomic limit is accurate. For the calculation we have assumed a temperature of  $T = 0.28 T_F$ , which is deduced from the entropy in the dipole trap. For zero temperature the slope  $\partial D/\partial N$  would vanish as soon as  $U$  becomes larger than the chemical potential  $\mu$ , which is  $h \times 2.7$  kHz for  $N = 8 \times 10^4$  atoms and a lattice potential of  $V_0 = 12 E_R$ . Both our measurements and the model at finite temperature show a finite compressibility extending beyond  $U/h = 2.7$  kHz, which can be attributed to thermal excitations. For the largest interaction  $U/h = 8.1$  kHz the amount of thermal excitations is characterized by  $T = 0.11 U/k_B = 0.28 T_F$  corresponding to 3% vacancies in the trap center. The vanishing slope  $\partial D/\partial N$  at this filling implies incompressibility of the core. The obtained ratio  $T/U$  is comparable to estimates for the bosonic Mott insulator [169].

In the strongly repulsive regime, the measured compressibility should vanish if  $\mu < U$ . For atom numbers corresponding to higher chemical potentials a metallic phase will appear in the trap center and the double occupancy will increase. We observe this characteristic behavior [170] which is a consequence of the presence of a Mott insulator, see Figure 5.2b. The data agree well with the predictions of the Hubbard model in the atomic limit (lines in Figure 5.2b). The free parameters in the theory curves, the temperature and a constant offset in  $D$ , are determined by a least squares fit to the data. The fits yield temperatures of  $0.2(1) T_F$ . However, the accuracy is limited due to the high sensitivity to the energy gap and the harmonic confinement. The constant offset in  $D$  accounts

for the finite double occupancy in the ground state caused by second order tunneling processes as well as a systematic offset of 0.5% stemming from technical imperfections in the initial preparation of the spin mixture.

### *Excitations in the Mott-insulating regime*

An important feature of a Mott insulator is the energy gap in the excitation spectrum. The lowest lying excitations are particle-hole excitations centered at an energy  $U$ . The actual gap in the energy spectrum is reduced with respect to this value due to the width of the energy bands experienced by particles and holes [171]. A suitable technique for probing this excitation spectrum is to measure the response of the quantum gas in the optical lattice to a modulation of the lattice depth [118, 172, 173]: we apply 50 cycles of sinusoidal intensity modulation of all three lattice beams with an amplitude of 10%. The response is quantified by recording the double occupancy after the modulation as a function of modulation frequency. With increasing interactions we observe the emergence of a gapped mode in the excitation spectrum (Figure 5.5). For small values of  $U/6J$ , the double occupancy is not affected by the modulation of the lattice depth independent of the frequency. For large values of  $U/6J$  in the Mott-insulating regime a distinct peak appears for modulation frequencies  $\nu$  near  $U/h$ .

Furthermore, the area  $w$  under the excitation curve is shown in Figure 5.5d. It is determined from the spectrum according to

$$w = \sum_i \Delta\nu \left[ D(\nu_i) - \frac{1}{2}(D(200 \text{ Hz}) + D(700 \text{ Hz})) \right], \quad (5.5)$$

where  $D(\nu_i)$  is the measured double occupancy at frequencies  $\nu_i$  which are evenly spaced in steps of  $\Delta\nu = 500 \text{ Hz}$ . The area is plotted in units of the band width  $12J/h$ . It is a measure for the width and the weight of the excitation mode and increases with interaction strength before it saturates at large values of  $U/6J$ .

### *Conclusion*

The presented approach to the physics of the repulsive Fermi-Hubbard model is completely different and complementary to that encountered in solid-state systems, and provides a new avenue to one of the predominant concepts in condensed matter physics. In these first experiments we have found clear evidence for the formation of a Mott insulator of fermionic atoms in the optical lattice. We set limits for the deviation from unity filling in the Mott insulator by directly measuring the residual double occupancy and by deducing the number of holes from a realistic estimate of the temperature. The temperature is found to be small

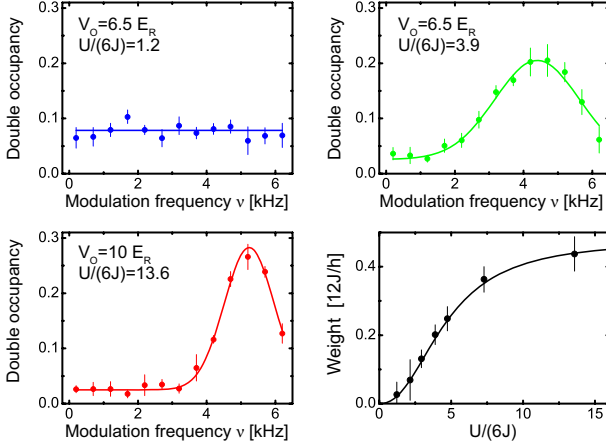


Figure 5.5: Emergence of a gapped mode. With increasing interaction (blue, green, red) the response to modulation of the lattice depth shows the appearance of a gapped mode. The weight of this peak grows with  $U/6J$  and saturates. All modulation spectra were obtained with  $32(2) \times 10^3$  atoms. The weight of the peak is shown in the bottom right panel. The first four data points are taken for a lattice depth of  $6.5E_R$ , the next at 7, 8 and  $10E_R$ , from left to right, respectively. The lines serve as a guide to the eye. Values and error bars are the mean and standard deviation of 4 to 8 measurements under the same conditions.

compared to the onsite interaction energy and the Fermi temperature. In addition, we have obtained good quantitative agreement with the Hubbard model in the atomic limit for a wide range of parameters. In further investigations of e.g. the energy spectra, the high resolution achieved may give direct insights into the width of Hubbard bands [171], and the level of anti-ferromagnetic ordering [112, 172] in the system. As presented in the following chapters the techniques developed in these experiments provide access to the details of the emergence and the lifetime of excitations.



## 6 Approaching quantum magnetism

Recent experiments [164, 64] including those presented in the preceding chapter have demonstrated that the strongly correlated regime of the repulsive Fermi-Hubbard model is experimentally accessible. In these experiments the emergence of a Mott-insulating state which is a prime example for these strong correlations has been observed.

In the next step towards the quantum simulation of the Fermi-Hubbard model the main challenge is a further reduction in temperature. Here the lack of a quantitative thermometry method in the lattice is a key obstacle. Different thermometry methods have recently been demonstrated for strongly correlated bosonic systems where the momentum distribution is a very sensitive probe. The temperature in the lattice could be inferred from a comparison of time-of-flight data with quantum Monte-Carlo simulations [174]. In another experiment the width of the boundary of two spin polarized clouds [175] was observed in analogy to domain walls in ferromagnetic materials [176]. In the fermionic case, previous methods to determine the temperature could be used only in limiting regimes of the Hubbard model, namely the non-interacting [80, 149] and zero-tunneling [164, 116] regimes. However, intermediate interactions are most interesting for quantum simulation of the Fermi-Hubbard model and no reliable thermometry method has been available up to now.

This chapter reports on a quantitative simulation of the Fermi-Hubbard model using cold atoms. The level of precision of the experiment enables us to determine the entropy and the temperature of the system, and thereby to quantify the approach to the low temperature phases of the Hubbard model in the regime of intermediate interactions.

The entropy of the system is determined by comparing accurate measurements of the equilibrium double occupancy with theoretical calculations over a wide range of parameters. In both the metallic and Mott-insulating regimes the double occupancy provides direct access to thermal excitations. We describe the crossover from thermal creation of double occupancies to thermal depletion which is unique to a trapped system. The variability of the double occupancy with respect to temperature allows the entropy of the system to be inferred directly by comparison with two *ab-initio* theoretical methods. We determine all other quantities entering the analysis separately and with methods that are independent of the double occupancy measurement and can assess the reliability of the entropy determination in a comprehensive analysis of all systematic errors.

---

Parts of this chapter have been published in [79]

## Experimental methods

### Spin mixture and atom number

To obtain a quantum degenerate Fermi gas we adhere to the procedure described in previous chapters. A balanced spin mixture of  $^{40}\text{K}$  atoms in the  $m_F = -9/2$  and  $-5/2$  magnetic sublevels of the  $F = 9/2$  hyperfine manifold is evaporatively cooled in a crossed beam optical dipole trap, with less than 1.2% of the atoms remaining in the  $m_F = -7/2$  state. We prepare Fermi gases with total atom numbers between  $N = 30 \times 10^3$  and  $300 \times 10^3$ . The atom number is calibrated using strong saturation imaging [154] at high magnetic field, with a remaining systematic error  $\sim 10\%$ .

### Lattice

The optical lattice potential is then ramped up in 0.2 s. Its depth of  $7E_r$  is determined from Raman-Nath diffraction of  $^{87}\text{Rb}$  and confirmed by resonant excitation of atoms to higher bands [145]. In the lowest Bloch band the tunneling matrix element is  $t/\hbar = 174(30)$  Hz. From transverse oscillations in the standing wave potentials of each lattice beam and the dipole trap we extract overall harmonic trapping frequencies of  $\omega_{[x,y,z]}/2\pi = [49.4(9), 52.6(6), 133.0(10)]$  Hz and a geometric mean of  $\omega/2\pi = 70.1(5)$  Hz. The characteristic filling is  $\rho = N/2N_0$  [167], where

$$N_0 = \frac{4\pi}{3} \left( \frac{12t}{m\omega^2 d^2} \right)^{3/2}. \quad (6.1)$$

### Interactions

We tune the interaction between the atoms by adjusting the scattering length in the proximity of the  $m_F = -9/2, -5/2$   $s$ -wave Feshbach resonance before loading into the lattice. To determine the scattering length, the width of the resonance was measured by using the suppressed dephasing of Bloch oscillations [142] to locate the zero crossing of the scattering length. We obtain a width of the resonance of 7.5(1) G which deviates from previous results [139] where the mean field energy was measured.

We infer the on-site interaction energy  $U$  from the scattering length and the Wannier function in the lowest Bloch band [3]. This *ab initio*  $U$  is experimentally validated using resonant excitation of double occupancies by lattice modulation. We cover the range from weak repulsion in the metallic regime to strong repulsion with a Mott-insulating core using scattering lengths between  $200a_0$  and  $650a_0$ . We choose values of the Hubbard parameter  $U/6t = 1.4(2), 2.4(4), 3.2(5)$  and  $4.1(7)$ .

## *Temperature*

Due to the lattice loading process, beam intensity noise, and spontaneous emission, the atoms heat up during preparation. Before loading into the lattice, the temperature in the dipole trap is around  $0.13T_F$  independent of the atom number as determined from the momentum distribution after time-of-flight. This corresponds to an entropy per atom of  $s = S/N \approx 1.3$ . Since the system is isolated from the environment, the temperature changes significantly even when adiabatically loading into the lattice. The entropy, however only changes due to non-adiabatic processes. Therefore we can find a typical upper limit of the specific entropy in the lattice by reversing the loading sequence and subsequently measuring the temperature after releasing the atoms from the dipole trap. Here we obtain  $s < 2.5$ .

## *Double occupancy measurement*

After loading the atoms into the lattice we determine the double occupancy. A sudden increase of the lattice depth suppresses further tunneling. The fraction of atoms on doubly occupied lattice sites  $D$  is then obtained by combining RF spectroscopy, Stern-Gerlach separation of the spin components and absorption imaging. The independently determined offset due to the imperfection of the initial spin mixture is accounted for at this point in the analysis. From long term reproducibility and comparison with the adiabatic formation of molecules via magnetic field sweeps we conclude that the relative systematic uncertainty of the double occupancy measurement is 10%.

## *Lattice thermometry*

Due to the harmonic trapping potential, the temperature behavior of the double occupancy can be markedly different from that of homogeneous systems [80, 177]. In a homogeneous Hubbard system with repulsive interactions and no magnetic order, the double occupancy always increases with temperature. However, in a harmonically trapped system an increase in temperature allows the atoms to reach outer regions of the trap, in turn reducing the density in the central region: in this case thermal excitations do not populate doubly occupied states but rather deplete them through the decrease of the density.

The regimes depicted in Figure 6.1 demonstrate the competition between thermal activation and the effect of the trapping potential on the double occupancy as a function of filling and entropy. The experimental data is compared with theoretical results to extract the entropy. The curves in Figure 6.1 correspond to the best fitting entropy and its experimental bounds.

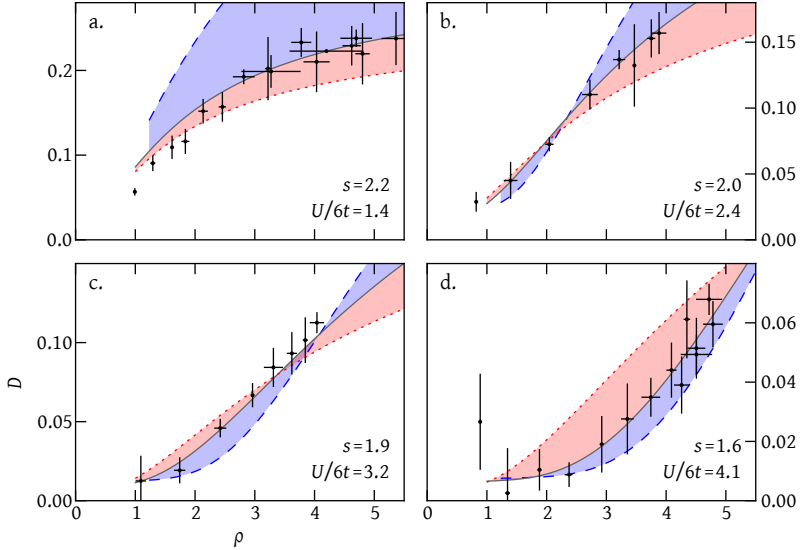


Figure 6.1: Double occupancy: experiment versus theory. Points and error bars are the mean and standard deviation of at least three experimental runs. The solid curve in each panel is the best fit of the second order high-temperature series to the experimental data and yields specific entropies of  $s = 2.2(2), 2.0(5), 1.9(4), 1.6(4)$  for the different interactions strengths of  $U/6t = 1.4(2), 2.4(4), 3.2(5), 4.1(7)$ . Curves for  $s = 1.3$  (dashed) and 2.5 (dotted) represent the interval of specific entropy measured before and after the ramping of the lattice.

We apply the high-temperature series expansion [113] as well as single-site dynamical mean-field theory (DMFT) [39] with a continuous time quantum Monte Carlo solver [178]. In the experimentally relevant regime we find the high-temperature series and DMFT to be in agreement to within 0.2%. For simplicity, the theoretical curves shown in this Letter are therefore generated using the second order high-temperature series unless stated otherwise. The entropy is determined from a one-parameter least-squares fit of the high-temperature series  $D(s, \rho_i)$  to the experimental data points  $D_i$  weighting them according to their statistical errors  $\sigma_{D_i}$ . The fit minimizes

$$\chi^2 = \sum_i (D(s, \rho_i) - D_i)^2 / \sigma_{D_i}^2. \quad (6.2)$$

The series is able to accurately reproduce the measured double occupancy for all shown interaction strengths. We find deviations of the experimental data only at



the lowest fillings at low repulsion, indicating that for very small atom numbers and weak interaction the cooling and loading procedure may fail to produce a constant entropy per atom.

The size and direction of the corridors between initial and final entropy in the dipole trap has implications for the usefulness of the double occupancy when performing thermometry. In Figure 6.1a the behavior for low repulsion  $U/6t = 1.4$  is shown. With increasing filling the system transforms from a dilute gas to an increasingly dense metal with high double occupancy. In this case the effect of the trapping potential dominates and  $D$  decreases with increasing entropy. Due to its large  $|\partial D/\partial s|$ , the regime well suited for thermometry.

At intermediate repulsion strengths in Figure 6.1b and c, double occupancies become increasingly suppressed and  $|\partial D/\partial s|$  decreases. The derivative  $\partial D/\partial s$  changes sign at a certain filling for each interaction strength. These points mark the crossover to thermal suppression of double occupancies. If  $\partial D/\partial s$  vanishes, the theory becomes parameter-free to first order and can be used to further determine other calibration factors, e.g., the characteristic filling.

Figure 6.1d shows data for clouds in the Mott insulating regime. It exhibits a pronounced plateau of suppressed double occupancy at intermediate fillings owing to a vanishing core compressibility, a characteristic signature of a Mott-insulating core. Large filling can increase the chemical potential to values comparable with  $U$  and thus create double occupancy. In this regime the thermal activation of double occupancies dominates over the thermal decrease of density due to the trapping potential. If  $\partial D/\partial s > 0$  a large fraction of particles resides in the Mott-insulating core. Here the chemical potential is high enough to prevent holes from entering the center and additionally the density of states is sufficiently gapped to allow only few thermally excited double occupancies.

The rate of change of the double occupancy with average entropy is explored in Figure 6.2 for an entropy of  $s = 1.6$  and all relevant characteristic fillings and repulsive interactions. The two regimes of dominant thermal activation of double occupancy (red) and depletion (green) can be distinguished. The magnitude of the response to changes in entropy grows with filling due to the increasing relative size of the doubly occupied or Mott-insulating region. In the regime of large  $U$  and small filling numerical imprecision leads to an unphysical slightly negative  $\partial D/\partial s \sim -0.001$ .

### *Error budget*

We now consider the errors of the parameters and measurements to assess the absolute reliability of the present method in determining the entropy. Table 6.1 lists the contributions. The sensitivity of the least squares fit to variation of the respective parameter shows the sign of the influence as well as the magnitude.

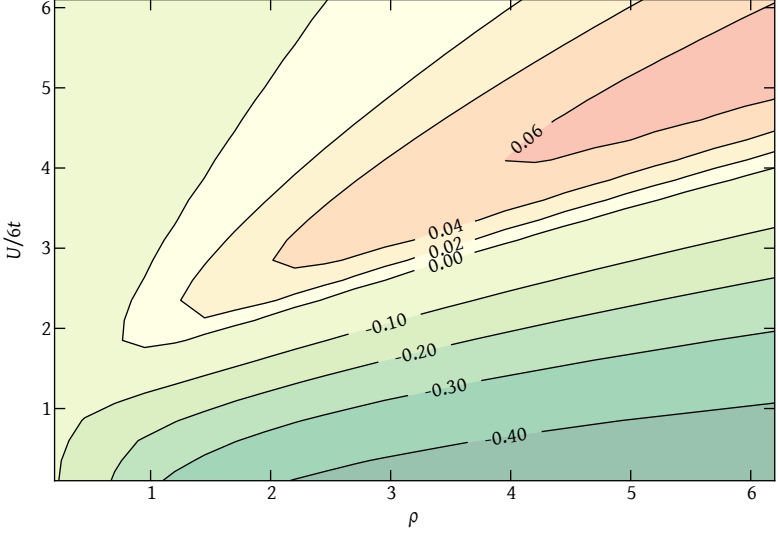


Figure 6.2: Sensitivity of the double occupancy to changes in specific entropy. The plot shows the change in double occupancy with changing entropy  $\partial D/\partial s$  for different characteristic fillings  $\rho$  and interaction strengths  $U/6t$  and  $s = 1.6$ . The simulation is based on the high temperature series expansion up to second order.

$U/6t$	1.4	2.4	3.2	4.1
$\delta_r \partial s_{\text{fit}}/\partial t$	-0.01	0.01	-0.11	-0.08
$\delta_U \partial s_{\text{fit}}/\partial U$	$\sim 0$	-0.04	0.07	0.09
$\delta_\omega \partial s_{\text{fit}}/\partial \omega$	0.01	0.07	-0.07	-0.07
$\delta_N \partial s_{\text{fit}}/\partial N$	0.06	0.30	-0.32	-0.32
$\delta_D \partial s_{\text{fit}}/\partial D$	-0.16	-0.30	0.13	0.13
$\sigma_s$	0.01	0.12	0.18	0.07
total $s$	2.2(2)	2.0(5)	1.9(4)	1.6(4)

Table 6.1: Error budget of the entropy determination. The table lists the sensitivity of the fit  $\partial s_{\text{fit}}/\partial(\cdot)$  to the changes in the system's parameters scaled by their systematic errors  $\delta_{(\cdot)}$ . For a positive contribution an increase in the parameter would lead to an increase in the apparent entropy. The contributions are added in quadrature to the fit error estimate  $\sigma_s^2 = 2(\partial^2 \chi^2/\partial s^2)^{-1}$  to obtain the total uncertainty of the entropy.

The total relative uncertainties are below 25% for all four interaction strengths which confirms the validity of the determined entropies. It is apparent that

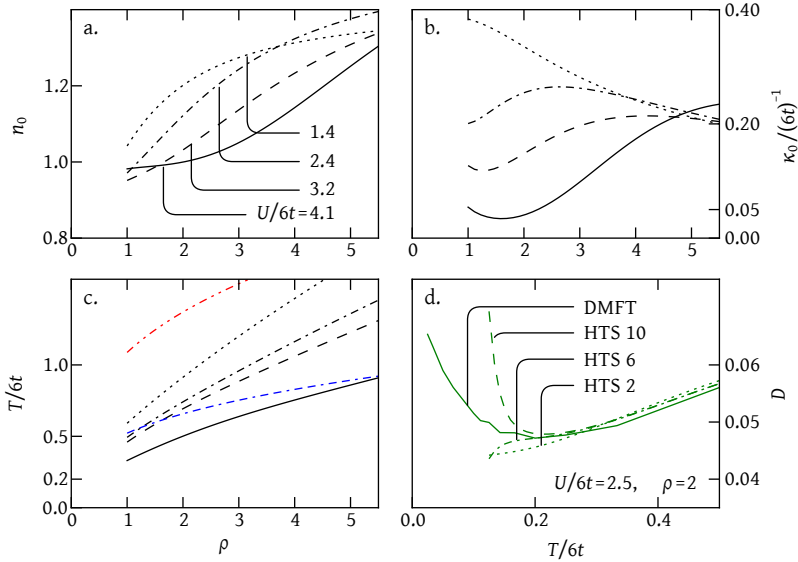


Figure 6.3: Properties of experimental regimes and validity of theoretical methods. Panels a, b, and c show the central density  $n_0$ , central compressibility  $\kappa_0$  and temperature  $T$  reached in the corresponding Hubbard model as a function of characteristic filling  $\rho$  for the parameters of Figure 6.1. The dash-dash-dotted (dash-dot-dotted) curve in panel c corresponds to the temperature for  $s = 1.3$  ( $s = 2.5$ ) without lattice and interaction but the same atom number and trapping frequency as in the lattice. Panel d: agreement between high-temperature series (HTS: second order dotted line, sixth order dash-dotted, tenth order dashed line) and DMFT (solid line) for  $U/6t = 2.5$  and  $\rho = 2$  as a function of temperature in the lattice  $T/6t$ . For low temperatures  $T \lesssim t$  the series starts to diverge.

the systematic errors dominate and that especially the atom number and double occupancy calibrations are critical. The observed increase of the specific entropy with decreasing interaction can be explained by an interaction-dependent global adiabaticity of the preparation [179] or by a combination of systematic errors in  $N$  and  $D$ .

### *In-trap properties and validity of numerical methods*

Several unique properties of trapped repulsively interacting Fermi-Hubbard systems can be derived from the theoretical description. Figure 6.3a and b show the central density  $n_0$  and compressibility  $\kappa_0 = \partial n_0 / \partial \mu$  versus characteristic filling

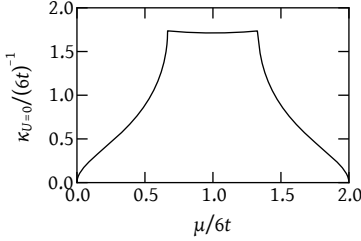


Figure 6.4: Density of states in the homogeneous non-interacting 3D Hubbard model.

for the interaction strengths and specific entropies of Figure 6.1. The plateau in  $n_0$  and the reduction of  $\kappa_0$  for  $U/6t = 4.1$  are signatures of the Mott insulating regime [177].

To compare the compressibility in the Mott-insulating regime with that of the ground state in the Hubbard model without interaction, we derive the density of states. In the cosine-shaped band structure  $E(q_x, q_y, q_z)$  of the lowest band, with the quasimomenta  $q_x, q_y, q_z$  in the first Brillouin zone,  $-\pi < q_i < \pi$ , we have for the number of states up to an energy  $E$ :

$$E(q_x, q_y, q_z) = 6t - 2t \cos(q_x) - 2t \cos(q_y) - 2t \cos(q_z) \quad (6.3)$$

$$N(E) = \frac{1}{4\pi^3} \int_{-\pi}^{\pi} \int_{-\pi}^{\pi} \int_{-\pi}^{\pi} \Theta(E - E(q_x, q_y, q_z)) dq_z dq_y dq_x. \quad (6.4)$$

where  $\Theta(x)$  is the Heaviside step function. Using abbreviated units,  $t = 1$  and  $e = |E/t - 6|/2$ , the density of states can be expressed in terms of the complete elliptic integral of the first kind  $F(m)$  [180]:

$$\kappa_{U=0}(e) = \frac{1}{\pi^3} \int_{\max(-1, -2-e)}^{\min(1, 2-e)} F\left(1 - \frac{(e+a)^2}{4}\right) \frac{1}{\sqrt{1-a^2}} da \quad (6.5)$$

$$F(m) = \int_0^{\pi/2} \frac{1}{\sqrt{1-m \sin^2 b}} db. \quad (6.6)$$

In the center of the band at half filling  $\mu = 6t$ , the density of single particle states and equally the compressibility of the ground state are  $\kappa_{U=0} \approx 1.69/6t$ . Compared to this value, the compressibility in the center of the trap at the largest interaction is suppressed by a factor of 50 to values as low as  $\kappa_0 \approx 0.03/6t$ .

The entropy as determined above needs to be related to a temperature to allow for comparison with models of homogeneous systems. Figure 6.3c shows this temperature in units of the half bandwidth as a function of characteristic

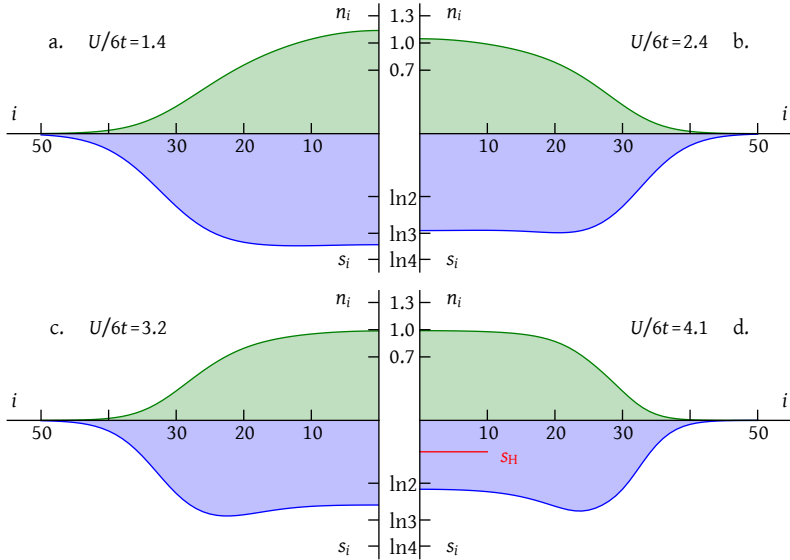


Figure 6.5: Density and entropy distribution in the trap. For the interaction strengths and entropies of Figure 6.1 the density  $n_i$  (upward) and entropy  $s_i$  (downward) per site  $i$  at a characteristic filling of  $\rho = 1.5$  in a spherically symmetric system are shown. The buffering effect of the low-density shell around the Mott-insulating core becomes clearly visible for  $U/6t = 4.1$ . There, the entropy reaches values of about twice the critical entropy of the Heisenberg model  $s_H \approx \ln 2/2$ .

filling. The behavior is similar to that of a Fermi gas in a harmonic trap where the temperature at constant specific entropy increases with the atom number. Figure 6.3c facilitates such a comparison of the temperature in the lattice with the temperature of a non-interacting gas at the same entropy and atom number in a dipole trap. The lattice temperatures which systematically have an entropy of  $s \geq 1.6$  approach the dipole trap temperature that corresponds to  $s = 1.3$ . This indicates the possibility of adiabatic cooling.

At the lowest fillings of  $\rho = 1$  the temperature in the lattice even approaches the energy scale of the tunneling  $T \sim t$ . At these low temperatures the results of high-temperature series and DMFT start to deviate considerably, see Figure 6.3d.

## Density and entropy distribution

In a finite trapped system, antiferromagnetic order requires two conditions to be met: It can only be established in regions of sufficiently constant atom density and low specific entropy. The experimental situation with respect to those conditions is depicted in Figure 6.5 for a characteristic filling of  $\rho = 1.5$  and the same parameters as those shown in Figure 6.1. The upward axes show the spatial density distribution. At low repulsive interaction (a-b) the system has a density above one in the center which corresponds to a significant doping. In panel c, double occupancies and holes compensate in the center and lead to an average density close to unity which then starts to deviate a few sites away from the center. Only for the largest repulsion d, the Mott-insulating core is robust against the confining potential over the central 20 sites. Here the density changes by less than 1%.

The entropy per site is shown on the downward axes in Figure 6.5. It is highest in regions of the trap where the density is most variable. For small interaction strengths it reaches values close to the maximum of  $s_i = \ln 4$  in some regions. For large repulsion the sites in the perimeter of the cloud where  $n_i \sim 2/3$  carry most of the entropy. This can be understood in the atomic limit at large  $U$ . At  $n_i = 2/3$  each site has three equally likely states and can accommodate  $s_i = \ln 3$  of entropy. The Mott-insulating core can only absorb  $\ln 2$  of spin entropy. Mean-field theory of the Heisenberg model predicts this to coincide with the entropy at its critical point. However, quantum fluctuations lower the entropy at the Néel temperature where magnetic long-range order sets in to about  $s_H \approx \ln 2/2 \approx 0.35$  [111]. We have verified numerically that for the Heisenberg model with exchange coupling  $J$  the entropy is  $s = 0.338(5)$  at  $T_{\text{Néel}}/J = 0.946(1)$  [181, 182] by integrating the energy,  $S = \int dE/T$ . Integration from above or below the Néel temperature agree. Additionally, we performed a new study of the Hubbard model using a diagrammatic determinant Monte Carlo method [183]. For  $U/t = 8$ , the critical temperature is  $T_{\text{Néel}}/t = 0.325(7)$  [37], and the critical entropy  $s_{\text{Néel}} = 0.345(45)$ . This differs from other mean-field calculation including fluctuation corrections [184] and is a factor of two less than the experimental results presented here.

## Conclusion

In the study presented here, we have demonstrated the versatility of the double occupancy in quantifying the state of the system and the applicability of both high-temperature series and dynamical mean field theory to obtain quantitative agreement with the experimental data. The achieved level of accuracy permits an experimental determination of the parameters needed to identify quantum magnetism of ultracold fermions in optical lattices, most importantly tempera-

ture and entropy. Using the theoretical models we have gained insight into the effects of the trapping potential on the distribution of entropy and density which lead to drastic differences and new regimes compared to the homogeneous case.

The details of the thermodynamic processes during the loading pose further interesting questions. An analysis of the fundamental and dominant contributions to diabatic heating during the loading could allow a significant reduction of the observed increase in entropy. Important steps to reduce the temperature in the lattice may lie in the possibility of adiabatic cooling due to the altered density of states.





## 7 *Controlling transport by interaction*

The study of conductivity in solids has led to the discovery of fundamental phenomena in condensed matter physics and to a wealth of knowledge on electronic phases. Intriguing quantum many-body phenomena such as superconductivity and the quantum Hall effect manifest themselves in their characteristic electronic transport properties. Moreover, the ability to manipulate conductivity has found numerous applications in technology, most prominently in semiconductors, where transport is controlled by electric biasing. Other ways to modify the conductivity in a material include adjusting temperature, pressure or magnetic field.

A gas of ultracold interacting fermionic atoms exposed to the potential of an optical lattice offers a new approach to study and control transport while providing a direct link to fundamental models in condensed matter physics. While the tunable interaction in these gases has been used to study fermionic superfluidity in the strongly interacting regime [185], it has so far not been applied to investigate transport phenomena in optical lattices. In previous experiments the transport of non-interacting fermionic atoms and the effect of a bosonic admixture mediating interactions were studied in one-dimensional optical lattices [30, 29]. Furthermore, the dynamics of Bose gases in a three-dimensional optical lattice was investigated experimentally [150, 186, 118] and theoretically [187, 188, 189, 190].

### *Introduction*

In this chapter we study the transport properties of a two-component  $^{40}\text{K}$  cloud trapped inside a three-dimensional optical lattice with underlying harmonic confinement. We monitor the center of mass motion of the atomic cloud after a sudden displacement of the trap minimum. The regimes of vanishing, weakly attractive and strongly attractive interactions are accessed by exploiting a Feshbach resonance to tune the scattering length for low energy collisions between the two atomic components. The atom number is adjusted so that at the trap center the lowest energy band is either filled or half-filled. For these parameters the system can be regarded as a realization of the attractive single-band Fermi-Hubbard model [191] with additional harmonic confinement. A Mott-

---

Parts of this chapter have been published in [149]

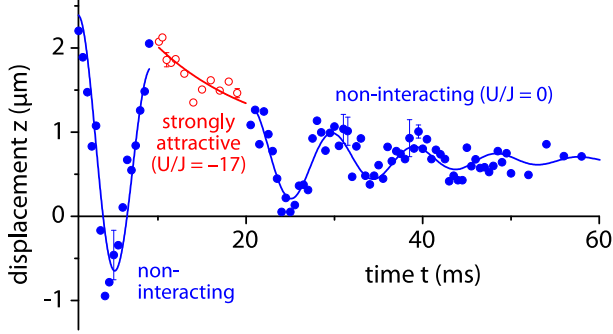


Figure 7.1: Dynamic control of transport by tuning the collisional interaction. The graph shows the center of mass motion of a two-component Fermi gas of  $2.9(3) \times 10^4$  atoms in a lattice of  $5E_r$  depth. At  $t = 0$ , the equilibrium position of the underlying harmonic trap is displaced vertically. After 9 ms of evolution without interaction ( $\bullet$ ), the magnetic field is changed linearly in 1 ms so that the interaction is strongly attractive ( $\circ$ ) for 10 ms. Then the magnetic field is changed to its original value again within 0.5 ms ( $\bullet$ ). The two non-interacting cases  $\bullet$  are each fit by a damped cosine and an offset, while the evolution with attractive interaction  $\circ$  is fit by an exponential decay and an offset. Error bars denote the standard deviation of at least four measurements.

insulating phase of pairs as discussed in the context of the multi-band Hubbard model [192, 186] is not expected.

The strong influence of the interactions on the transport is illustrated in Figure 7.1. An atomic cloud is prepared in the optical lattice at half filling and brought into non-equilibrium by displacing the trap minimum. The initially non-interacting cloud performs a weakly damped oscillatory motion in the confining potential. By temporarily switching on the attractive interaction, a controlled interruption of this oscillation is achieved.

## Experimental methods

### Preparation

We prepare a cloud of  $^{40}\text{K}$  atoms in an equal mixture of the hyperfine substates  $m_F = -9/2, -7/2$ . After evaporative cooling we obtain  $4 \times 10^4$  ( $3 \times 10^5$ ) atoms at temperatures below  $T/T_F = 0.20$  (0.25) in the dipole trap with final trapping frequencies of  $(\omega_x, \omega_y, \omega_z) = 2\pi \times (35, 23, 120)$  Hz, where  $T_F$  is the Fermi temperature. Next, the degenerate Fermi gas is subjected to the additional periodic potential of a three-dimensional optical lattice with a depth of  $5E_r$ . To load the atoms into the lowest Bloch band of the optical lattice, we increase the intensity

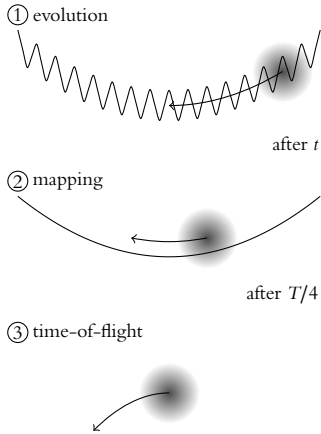


Figure 7.2: Mapping the cloud center of mass position in the lattice and dipole trap to momentum. The mass transport drives the evolution in the lattice for some time  $t$ . The lattice is then ramped down quickly and the cloud is allowed to oscillate in the pure dipole trap for a quarter of the oscillation period. This maps center of mass position to center of mass momentum. During time-of-flight, the cloud momentum is mapped again to position on the absorption image.

of the lattice beams using a spline ramp with a duration of 100 ms at a scattering length of  $a = 50a_0$ , where  $a_0$  is the Bohr radius.

### Observing transport

The gas is brought into a non-equilibrium position by increasing the beam intensities of the underlying dipole trap, which shifts the trap minimum by up to  $2.5 \mu\text{m}$  in the vertical  $z$ -direction. Since this displacement is smaller than our imaging resolution, we map the center of mass position of the atomic cloud to momentum space. For this purpose we switch off the optical lattice and let the cloud oscillate in the remaining harmonic dipole trap for a quarter period [150], see Figure 7.2.

After free expansion, we obtain the momentum distribution of the cloud from absorption imaging, determine the center of mass momentum using a Gaussian fit and infer the original displacement  $z$  of the cloud in the trap. Oscillations of the cloud size are not observed since the horizontal and vertical trapping frequencies are only increased by about 4% and 12%, respectively. Also, Bloch oscillations can be neglected for our small displacement since even for large fillings only few atoms gain sufficient energy to reach the band edge [193]. The energy deposited in the system by the trap displacement is estimated to increase the temperature in the lattice by an amount of  $0.05 T_F$ .

### *Attractive interactions*

Prior to the displacement of the trap the magnetic field is gradually ramped to final values between 210 G and 202.95 G within 50 ms, yielding an  $s$ -wave scattering length ranging from 0 to  $-1500a_0$ . This corresponds to an effective interaction strength  $U/J$  between 0 and  $-24$ .

The results of transport measurements for three interaction strengths and two different fillings are shown in Figure 7.3. We fit the function

$$z(t) = z_{\text{osc}} \cos(2\pi ft) \exp(-\beta t) + z_{\text{exp}} \exp(-\Gamma t) + z_0 \quad (7.1)$$

to the data. For the half filled case,  $3.6(4) \times 10^4$  atoms are prepared corresponding to 0.46(5) atoms per lattice site and spin state at the center of a non-interacting cloud.

In order to calculate the central filling and double occupancy the Hamiltonian for an isotropic non-interacting system with the same mean trapping frequency was diagonalized numerically on up to  $92^3$  sites at a temperature of  $0.27 T_F$  [80].

In the case of high filling, the samples contain  $2.7(3) \times 10^5$  atoms and form a large band insulating core. The filling factor of the Bloch band is position-dependent due to the inhomogeneous density profile of the trapped gas. The cases of zero, moderate and strong interaction are discussed hereafter.

In the non-interacting case with half filling we observe damped dipole oscillations (Figure 7.3(a) ◦). This damping of the center of mass motion can be attributed to the fact that the fermions in different quasi-momentum states possess different effective masses, resulting in a spectrum of oscillation frequencies. Furthermore, the total trapping potential is slightly anharmonic causing a dephasing also observed in the pure dipole trap. The system with high filling (Figure 7.3(a) ●) is characterized by a very slow relaxation towards the equilibrium position: The band insulating core suppresses center of mass motion and a large number of atoms occupy localized states [78, 194, 71, 29]. These single particle eigenstates exist at a distance  $z_{\text{loc}}$  from the center of the trap where the potential energy due to the harmonic confinement is larger than the bandwidth, i. e.  $m\omega_z^2 z_{\text{loc}}^2 / 2 > 4J$ . Consequently, the motion through the center is energetically prohibited. However, the atoms can still oscillate within the outer regions of the cloud. Even in the half filled case a small fraction of atoms is localized, which explains the small offset observed in the center of mass position after the decay of the oscillations (Figure 7.3(a) ◦).

The evolution of a non-interacting Fermi gas can be simulated by exact diagonalization the Hubbard Hamiltonian in the trap. The evolution for parameters comparable with those of Figure 7.3(a) ◦ is sketched in Figure 7.4. The low-filling case exhibits the dephasing that is also observed experimentally. The different effective masses lead to a reduced oscillation frequency compared with the free case and additionally to a periodic increase of the cloud size. In the

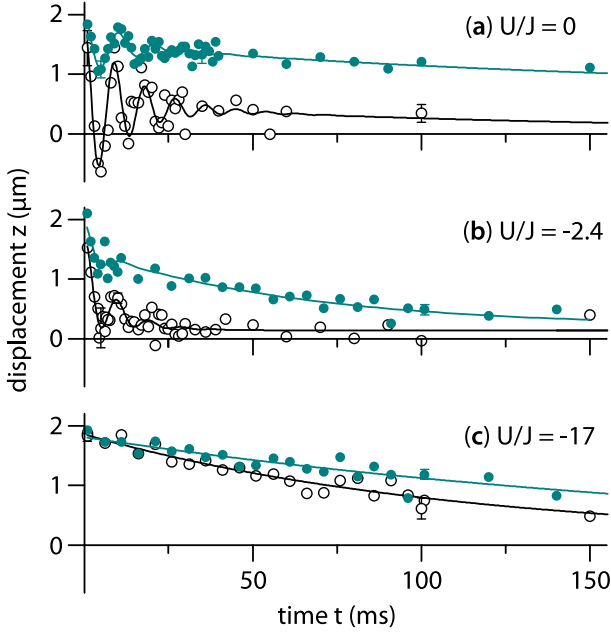


Figure 7.3: Evolution of the center of mass position for different interaction strengths and fillings. The circles  $\circ$  ( $\bullet$ ) denote samples in the half filled (band insulating) regime. For each data point the position of the cloud with and without displacement was compared to eliminate long term drifts. The error bars denote the standard deviation of at least 4 measurements.

large filling case also localized states and states with negative effective mass are occupied. The center of mass evolution of each initial single particle eigenstate is depicted in the lower panel. The different oscillation frequencies, the inverted oscillation of the states with negative effective mass and the confined oscillation of localized states can be clearly identified.

For moderate attractive interaction and half filling, the damping of the dipole oscillations becomes more pronounced (Figure 7.3(b)  $\circ$ ). The damping rate  $\beta$  increases from 80(17) Hz in the non-interacting case to 140(37) Hz at  $U/J = -2.4$ . As the interaction strength is increased beyond  $U/J < -3.5$ , the oscillations vanish entirely. The sample with high filling (Figure 7.3(b)  $\bullet$ ) relaxes faster towards equilibrium than in the non-interacting case, which can be attributed to umklapp processes [195].

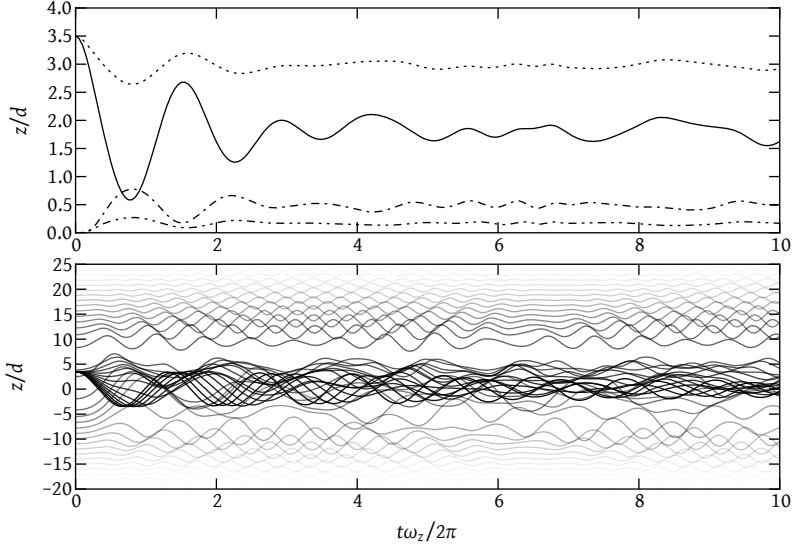


Figure 7.4: Transport oscillations of a non-interacting Fermi gas in an optical lattice. For similar parameters as in Figure 7.3(a) the evolution of the cloud has been simulated by exact diagonalization. The top panel shows the center-of-mass position in the low filling (solid) and large filling (dotted) case as well as the change in the clouds' root-mean-square size (dash-dotted and dash-dot-dotted for the two fillings respectively). The center-of-mass evolution of the individual single particle eigenstates are depicted in the bottom panel. Their occupation in the case of large filling is encoded in the opacity of the respective curve. Positions are given in units of the lattice spacing  $d = \lambda/2 = 532$  nm and oscillation times in inverse vertical trapping frequencies  $2\pi/\omega_z \approx 7.7$  ms.

In the strongly interacting case, a very slow relaxation is observed for both fillings (Figure 7.3(c)). The transport in this regime is governed by the dynamics of local fermionic pairs. In the limit of low atomic densities bound pairs form for  $U/J < -7.9$  [196, 17]. These pairs tunnel to adjacent sites via a second order process with an amplitude  $J_{\text{eff}} = 2J^2/U$ . This effective tunneling is obtained by considering a ground state where all atoms form pairs and by treating the tunneling term proportional to  $J$  as a perturbation in the Hubbard Hamiltonian [191]. Accordingly, the tunneling rate of pairs is reduced with increasing interaction as compared to bare atoms. Besides, the energy offset between neighboring sites due to the harmonic confinement reduces the tunneling probability. For these reasons we expect the relaxation time to become longer for stronger interactions. This is supported by the data in Figure 7.5, which shows a clear decrease

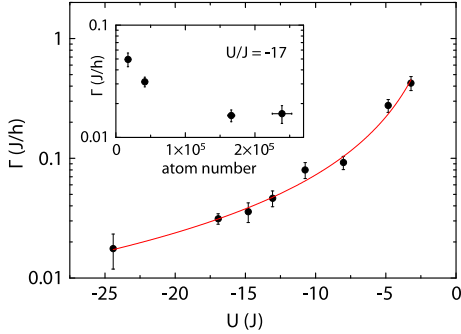


Figure 7.5: Relaxation rate  $\Gamma$  as a function of interaction strength. The data points and error bars are fit results to center of mass evolutions of  $3.8(4) \times 10^4$  atoms. The empirical power law  $h\Gamma = C J(U/J)^\nu$  with  $\nu = 1.61(3)$  and  $C = 2.95(17)$  fits the data well. The inset shows the dependence of the relaxation rate on the atom number.

of the relaxation rate  $\Gamma$  for growing attractive interaction. The data is well fit by the empirical power law  $\Gamma/J \propto (U/J)^{-1.61}$ . A quantitative understanding of this behavior is challenging due to the coexistence of bare atoms and local pairs which act as hardcore bosons in the lattice.

### Pair formation

Further insight into the physics of local pairs is gained by probing the double occupancy in the lattice for various interaction strengths without displacing the trap. For this purpose, we prepare the system at half filling as before and set the desired interaction within 50 ms by changing the value of the magnetic field. Then the lattice depth is abruptly increased from  $5E_i$  to  $30E_i$  in order to suppress further tunneling. By subsequently ramping the magnetic field from 203.26 G to 201.23 G within 5 ms, weakly bound Feshbach molecules are formed on those sites which are doubly occupied. We determine the number of atoms remaining after the molecule formation and compare it with the atom number which is obtained after dissociation of the molecules by applying the inverse magnetic field ramp. This yields the molecular fraction displayed in Figure 7.6, showing a strong dependence on the interaction strength: While for the non-interacting system the detected fraction is 18%, it increases up to 60% for strongly attractive interactions.

For the non-interacting gas the double occupancy in the lattice is solely determined by the number of trapped atoms and their temperature. The detected fraction of 18% is consistent with the temperature in the lattice of  $0.27(2)T_F$ ,

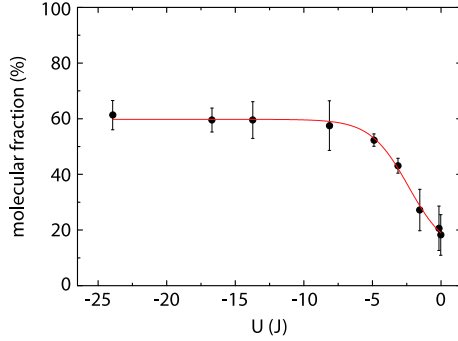


Figure 7.6: The fraction of molecules formed in the optical lattice increases with attractive interaction, demonstrating a higher number of doubly occupied lattice sites. Error bars denote the statistical errors of at least 4 measurements. The line serves as a guide to the eye.

which we determined in a separate measurement with  $2.7 \times 10^5$  atoms yielding a molecular fraction of 46(2)%. This temperature, even though measured in an ideal gas, suggests that the gas remains above the critical temperature for superfluidity also for strong interactions. Numerical calculations for a homogeneous interacting system show a considerable temperature dependence of the double occupancy [197]. We therefore expect that the temperature of the interacting gas can be deduced from the measured double occupancy.

The increase of the molecular fraction with rising attractive interactions provides strong evidence for the formation of local pairs. In accordance with numerical calculations for the attractive Hubbard model at finite temperature [36] the number of doubly occupied sites increases already for weak attraction and even in a regime where no bound state exists in the two-body problem ( $U/J > -7.9$ ). Pair formation in the many-body regime is expected to start at a value of  $U/J \approx -2$ .

For strong attractive interactions,  $U/J < -7.9$ , the number of doubly occupied sites saturates. This is in accordance with the fact that the pairs are well localized on single lattice sites and can be regarded as hardcore bosons. An increase in molecular fraction due to an attraction-induced shrinking of the cloud, which would result in a higher average density, is not substantiated by the following measurements: When tuning the interaction strengths we could not detect a change in the size of the trapped atom cloud with our measurement accuracy of 10%. Furthermore, the same increase in molecular fraction is found if the attractive interaction is turned on within only one tunneling time. This demonstrates



that we observe local pairing rather than a redistribution of the trapped atoms on a larger scale.

### *Conclusion*

In conclusion, we have found that the transport of an attractively interacting Fermi gas in a 3D optical lattice is strongly influenced by the formation of local pairs. In the future, studying the oscillation frequency below the superfluid transition temperature could serve to characterize the BCS-BEC crossover [198]. Extending these studies to the repulsive Fermi-Hubbard model may provide a tool to further explore quantum phases such as the fermionic Mott insulator.



## 8 *Observing elastic doublon decay*

Understanding the far-from-equilibrium dynamics of strongly correlated systems is a highly challenging task. Even the identification of the basic processes involved and the associated time scales is nontrivial when the system cannot be described by weakly interacting excitations or quasiparticles. In these systems, dynamics may couple states with widely different energies making the description in terms of a restricted set of low energy states as in the Fermi liquid theory impossible. Some progress has been made for one-dimensional systems, where it is often possible to obtain exact solutions for the eigenstates of the Hamiltonian. The absence of thermalization in one-dimensional Bose systems has been predicted [200, 201, 202] and observed [203] in cold atomic gases. However, these studies are hard to generalize to higher dimensions.

The main difficulty in analyzing non-equilibrium dynamics in the setting of condensed matter experiments is the strong coupling to the environment, which introduces extrinsic relaxation mechanisms and renders the controlled preparation and relaxation of far-from-equilibrium initial states a challenging task. By contrast, the nearly perfect isolation of many-body systems realized with ultracold atoms makes them a perfect candidate for studying the intrinsic dynamics of strongly correlated systems. In the setting of ultracold atoms it is possible to prepare a well-controlled initial state, evolve it under the action of a precisely defined microscopic Hamiltonian, and monitor the effects of the characteristic relaxation process [204].

This chapter reports on an investigation of the relaxation of artificially created highly excited states in the repulsive Fermi-Hubbard model with ultracold atom systems. Due to the negligible coupling to an external environment, we are able to carry out a direct comparison of experiment and theory. The interpretation of these results shows the importance of high-order scattering processes in bridging the energy gap between low- and high-energy excitations and how they can lead to exponentially slow thermalization.

This problem appears in diverse contexts like multiphonon decay of excitons in semiconductors [205], pump-probe experiments [206] and dynamics of resonances in nuclear matter [207].

Similar excitations are also probed in experiments that combine ultrashort laser or soft x-ray pulses with solid state systems [28, 208, 209]. In these systems, phase transitions emerge due to the creation of high energy excitations. The details, however are frequently challenging to analyze as the lattice degrees of

---

Parts of this chapter have been published in [141, 199]

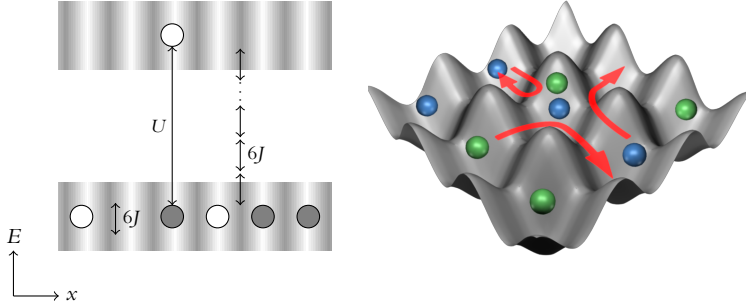


Figure 8.1: Stability of highly excited states in the single-band Hubbard model. Doubly occupied lattice sites are protected against decay by the on-site interaction energy  $U$ . The average kinetic energy of a single particle in a periodic potential is half the bandwidth  $6J$ . Thus the relaxation of excitations requires several scattering partners to maintain energy conservation.

freedom can play a dominant role and alter the physics of the electronic degrees of freedom.

### Introduction

In the experiment, we study the time evolution of doubly occupied lattice sites (doublons). In the context of a dilute Bose-Hubbard system isolated repulsively bound pairs have been experimentally identified and studied [210]. In this chapter the tunneling matrix element is denoted by  $J$  instead of  $t$  as has been common practice.

We report on the observation of elastic decay of artificially created doublons into single particles. The doublons are found to live longer as the interactions become stronger. More specifically their lifetime increases exponentially with the ratio of on-site interaction to kinetic energy in the lowest Bloch band  $U/6J$ . We argue that a doublon, having an excess energy  $U$ , decays in a scattering process involving several single fermions, see also Figure 8.1. Since each of these scattering partners can only absorb an average energy of  $6J$ , the number of virtual states involved in the simultaneous many-body process is  $U/6J$ . Hence the decay is exponentially suppressed for increasing  $U/6J$ . We find good agreement with diagrammatic calculations where the strongly correlated nature of the underlying state is crucial in obtaining the correct value of the scaling exponent.

## Experimental methods

### Preparation

The experimental sequence used to produce quantum degenerate Fermi gases has been described in detail the previous chapters. We prepare a balanced spin mixture of  $50(5) \times 10^3$   $^{40}\text{K}$  atoms at temperatures below 15% of the Fermi temperature  $T_F$ . The confinement is given by a dipole trap with trapping frequencies  $\omega_{[x,y,z]}/2\pi = [35, 23, 120]$  Hz. Using Feshbach resonances in either the  $m_F = -9/2, -7/2$  or  $m_F = -9/2, -5/2$  mixture, the interaction strength is tuned in the range  $98a_0$  to  $131a_0$  or  $374a_0$  to  $672a_0$ .

After adjusting the scattering length to the desired value, we add a three-dimensional cubic optical lattice. The lattice depth is increased in 200 ms to final values between  $6.5E_r$  and  $12.5E_r$ . The statistical and systematic errors in the on-site interaction strength  $U$  and the nearest-neighbor tunneling  $J$  are dominated by the lattice calibration and the accuracies in width and position of the two Feshbach resonances. Depending on  $U$  and  $J$  the accessible final regimes from metallic to Mott-insulating phases with an equilibrium double occupancy  $N_{d0}$  below 15%.

### Excitation, decay, and detection

The preparation of the system is followed by a sinusoidal modulation of the lattice depth with an amplitude of 10% and frequency close to  $U/h$ . This causes an increase of the double occupancy  $\Delta N_d$  to values up to 35% [172, 211, 212].

After the modulation the system is in a non-equilibrium state, which we let evolve freely at the initial lattice depth and interaction strength for up to 4 s. This is followed by a sudden increase of the lattice depth to  $30E_r$  which prevents further tunneling. We then measure the amount of atoms residing on doubly and singly occupied sites  $N_d$  and  $N_s$  by encoding the double occupancy into a previously unpopulated spin state using rf spectroscopy. Combining Stern-Gerlach separation and absorption imaging allows us to determine the population of all three spin components and to obtain single occupancy  $n_s = N_s/N_{\text{tot}}$ , double occupancy  $n_d = N_d/N_{\text{tot}}$ , and total atom number  $N_{\text{tot}} = N_s + N_d$  simultaneously in a single run.

### Evaluation

We repeat the experiment for a range of different times of free evolution and record the total atom number as well as the single and double occupancy, see Figure 8.2. The double occupancy is found to decay exponentially in time, while losses are observed on longer timescales. These losses lead to a reduction of the total atom number. To extract the doublon lifetime we model the decay

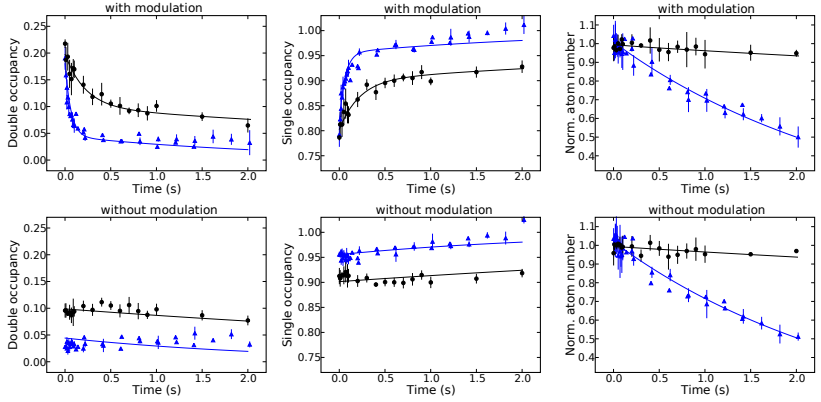


Figure 8.2: Time evolution of double occupancy, single occupancy and total atom number for two different ratios  $U/6J$  (round and triangular symbols). In the upper row, the system was previously excited via lattice modulation. The bottom row shows the reference measurement for the determination of the residual dynamics. The round data points were recorded using a  $m_F = -9/2, -7/2$  spin mixture with  $U/h = 1.4$  kHz and  $J/h = 70$  Hz, whereas the triangular data points show a  $-9/2, -5/2$  mixture with  $U/h = 3.2$  kHz and  $J/h = 100$  Hz. The solid lines are simultaneous fits of the integrated population equations 8.1. The total atom numbers are scaled to their initial values. Single occupancy and double occupancy are the fraction of atoms residing on sites of the respective type. Due to different detection efficiencies for hyperfine states the sum of double and single occupancy can be higher than one. Error bars denote the statistical error of at least four measurements for the same parameters.

by a set of coupled rate equations:

$$\begin{aligned}
 \Delta \dot{N}_d &= -\left(\frac{1}{\tau_D} + \frac{1}{\tau_{\text{inel}}} + \frac{1}{\tau_{\text{loss}}}\right) \Delta N_d, \\
 \dot{N}_{d0} &= -\left(\frac{1}{\tau_{\text{inel}}} + \frac{1}{\tau_{\text{loss}}}\right) N_{d0}, \\
 \dot{N}_s &= \frac{1}{\tau_D} \Delta N_d - \frac{1}{\tau_{\text{loss}}} N_s.
 \end{aligned} \tag{8.1}$$

Here, the dot denotes the time derivative. The three time constants parametrize three independent local decay processes differing in the type of site they affect:

- The lifetime of doublons  $\tau_D$  describes a population flow from doubly occupied to singly occupied lattice sites visible as a fast decay of the double occupancy within 0.01–1 s and a synchronous increase of the single occupancy. This process conserves the total atom number.

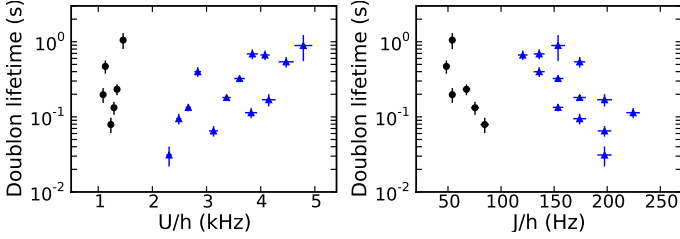


Figure 8.3: Doublon lifetime as a function of  $U$  and  $J$ . The circles show the fit results to datasets as shown in Figure 8.2, obtained with a  $-9/2, -7/2$  spin mixture while the triangular data points correspond to the  $-9/2, -5/2$  mixture. Error bars denote the confidence intervals of the lifetime fits and the statistical errors in  $U$  and  $J$ .

- The loss time constant  $\tau_{\text{loss}}$  corresponds to atom losses affecting both doubly and singly occupied site types in the same manner. This process is only observed in a change of the total atom number and not in the occupancy fractions. Collisions with hot atoms from the background vapor pressure could in part be responsible for this loss.
- Doubly occupied sites are generally subject to enhanced two-body losses due to the  $s$ -wave Feshbach resonance or due to coupling to a  $p$ -wave resonance channel. We summarize these additional inelastic losses on doubly occupied sites by  $\tau_{\text{inel}}$ . The loss is visible as a simultaneous decay of both the total atom number and double occupancy.

Changes of the decay times during the decay and other higher order terms in the rate equations are not included.

We integrate Equation 8.1 and fit the resulting system of time-dependent population equations to the time evolution of single and double occupancy as well as to the total atom number. To further reduce the coupling of the different decay rates, we assert that the two loss processes must identically affect a reference data set where no additional double occupancies have been created by lattice modulation. We record this reference data set time-interleaved with the actual decay data. Since the modulation does not change the losses, this procedure removes the influence of  $\tau_{\text{inel}}$  and  $\tau_{\text{loss}}$ , allowing for a reliable determination of the doublon lifetime  $\tau_{\text{D}}$ . The model and the observation are found to agree very well within experimental uncertainties, as shown in Figure 8.2.

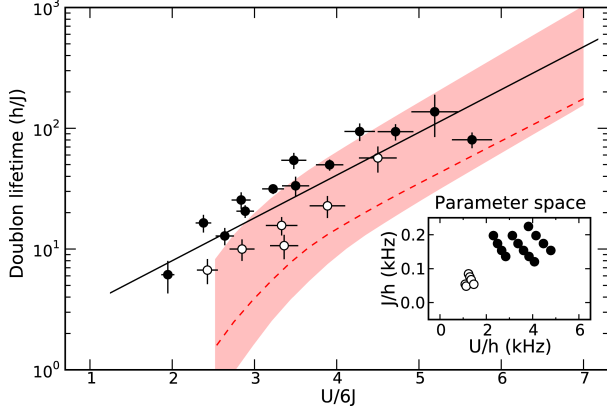


Figure 8.4: Semilog plot of doublon lifetime  $\tau_D$  versus  $U/6J$ . The lifetime is extracted from datasets as shown in Figure 8.2. Solid and hollow circles denote the  $(-9/2, -5/2)$  and  $(-9/2, -7/2)$  spin mixture respectively, while the dashed line shows the theoretical result at half filling. The solid line is a fit of Equation 8.2 to the experimental data, yielding  $\alpha = 0.82(8)$ , whereas for the theory curve the asymptotic slope at large  $U/6J$  is  $\alpha_{\text{theo}} = 0.80$ . The shaded corridor was obtained by varying the filling factor in the calculation by 30%. The inset shows the parameters used to realize the different values of  $U/6J$ . Error bars denote the confidence intervals of the lifetime fits and the statistical errors in  $U/6J$ . The systematic errors in  $U/6J$  and  $\tau_D/(h/J)$  are estimated to be 30% and 25%, respectively.

### Doublon lifetimes

We measure this doublon lifetime for various tunneling and interaction strengths, covering a parameter range where  $J$  and  $U$  each differ by more than a factor of four. The determined absolute lifetimes vary over two orders of magnitude, as shown in Figure 8.3. Furthermore, the lifetime clearly does not depend on the tunneling energy or the interaction energy alone.

The lifetime in units of the tunneling time is plotted logarithmically versus the ratio  $U/6J$  in Figure 8.4. The data is well described by an exponential function:

$$\frac{\tau_D}{h/J} = C \exp\left(\alpha \frac{U}{6J}\right). \quad (8.2)$$

The scaling exponent  $\alpha$  is found to be  $\alpha = 0.82(8)$  with  $C = 1.6(9)$  and we find fair agreement with our numerical model of the doublon lifetime which is outlined below.



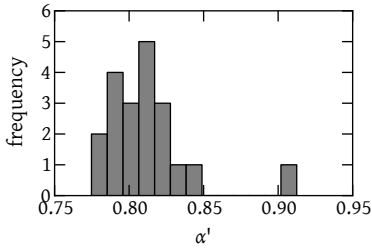


Figure 8.5: Jackknife resampling analysis of the scaling exponent. By performing the regression analysis on reduced data sets that each exclude a single lifetime measurement, a histogram of values for  $\alpha$  is obtained.

The Pearson correlation coefficient  $R = 0.87$  indicates a predominantly linear relationship between  $U/6J$  and the logarithm of the lifetime. The residual scatter of the data in Figure 8.4 as well as the apparent systematic deviation of some data points from the expected exponential warrant further statistical analysis.

We first assess the sample bias due to outliers by performing a jackknife resampling analysis [213, 214] of the lifetime data. From the original parent set of  $n$  samples of the lifetime,  $n$  new sets of size  $n - 1$  are generated by removing each single data point once. For each of the sets, the regression analysis is performed resulting in a distribution of values for  $\alpha$ , see Figure 8.5. The sample with the largest bias is the one at the largest  $U/6J$ . Removing this data point from the set results in a significant shift of the apparent scaling exponent to  $\alpha' = 0.91(11)$ . The remaining values for  $\alpha$  corresponding to excluding the other samples appear normally distributed with standard deviation of  $\sigma'_\alpha = 0.017$  which is much smaller than the error estimate obtained from the residuals of the regression. This analysis supports the assertion that the rightmost data point in Figure 8.4 is an outlier. The data point indeed corresponds to one of the largest lifetimes in both absolute and relative units and could therefore be influenced by other effects beyond those described here. Additionally, for large  $U/6J$  losses are expected to mask the observation of very long lifetimes.

The systematic deviation of the data for the two spin mixtures seems to indicate that the data show physics beyond the one-parameter exponential of Equation 8.2. Separate fits to the two spin mixtures yield values of  $\alpha_{-9/2, -5/2} = 0.75(10)$ ,  $C_{-9/2, -5/2} = 2.5(9)$  and  $\alpha_{-9/2, -7/2} = 1.00(14)$ ,  $C_{-9/2, -7/2} = 0.5(2)$ . The slight offset between the two spin mixtures could be due to the fact that the absolute values for  $U$  and  $J$  differ significantly between the  $-9/2, -5/2$  and the  $-9/2, -7/2$  mixture. Whilst the ratio between interaction energy and kinetic energy  $U/6J$ , which dominates the dynamics, lies in the same range, the absolute values also matter in an inhomogeneous system. For the  $(-9/2, -7/2)$  mixture the higher ratio of chemical potential to on-site interaction is expected to lead to a higher filling in the trap center and consequently to a higher equilibrium double occupancy  $N_{d0}$  than for the  $(-9/2, -5/2)$  mixture. It is conceiv-

able that this difference modifies the dynamics of doublon creation and doublon relaxation.

In additional measurements we have examined the dependence of the doublon lifetime on the additionally created double occupancy  $\Delta N_d$  and on the total atom number  $N$ . In the former case, we reduced the lattice modulation amplitude from 10% to 5%, resulting in  $\Delta N_d = 9\%$  instead of  $\Delta N_d = 18\%$ , while keeping all other parameters constant with  $U/6J = 4.5$ . The measured lifetimes agree within the error bars, they are  $\tau_{D,5\%} = 77(25) \times h/J$  and  $\tau_{D,10\%} = 58(10) \times h/J$ , respectively. In the latter case, we prepared two otherwise identical samples at  $U/6J = 3.4$  with  $N = 49(7) \times 10^3$  atoms and with  $N = 26(4) \times 10^3$  atoms, respectively, yielding  $\tau_{D,49k} = 11(2) \times h/J$  and  $\tau_{D,26k} = 19(2) \times h/J$ . Both tests show that, although there is a dependence on the total density and on the doublon density, these effects are small compared to the dominant scaling with  $U/6J$ .

In the following we argue that this exponential scaling of the doublon lifetime originates from a high order scattering process involving several single atoms as scattering partners. In the preparation of the non-equilibrium state by lattice modulation, we create holes as well as doublons in the bulk and thus drive the system into a compressible state. An isolated doublon has an energy  $U$ , which it must transfer to other excitations in order to decay. In the compressible state the most relevant excitations are metallic with a typical energy scale of only  $6J$ . Thus a doublon must scatter with several fermions. The number of scattering partners is on the order of  $n = U/6J$ . The matrix element  $M$  for the decay rate  $\Gamma$  may be estimated via perturbation theory

$$M \sim \frac{J}{6J} \times \frac{J}{2 \times 6J} \times \dots \times \frac{J}{n \times 6J} \quad (8.3)$$

$$\frac{h/J}{\tau_D} \propto \frac{\Gamma}{J} \propto M^2. \quad (8.4)$$

Using Stirling's formula, we then find the same scaling behavior as in Equation 8.2. Here  $\alpha$  is a parameter on the order of unity and depends at most logarithmically on  $U/6J$ .

### *A model for the doublon lifetime*

In our experiments, the doublons and holes are created at finite density by driving the system with optical lattice modulations. The relaxation of the system to equilibrium involves two phases with two very different time scales. The first timescale is associated with the relaxation of holes and doublons to a state of quasi-equilibrium without the decay of doublons. This fast relaxation to their metastable states takes place within the upper and lower Hubbard bands

respectively. The second timescale, which is the focus of this paper, is associated with the decay of doublons into kinetic excitations. We expect that the second timescale is much slower than the first.

Before constructing a model for doublon decay, we determine the dominant mechanism of decay. In the experiments, lattice modulation created 15-35% double occupancies. Assuming an initially half-filled system, this corresponds to a large additional density of holes created in the system. At these hole densities, the kinetic energy assisted decay scaling as  $\sim \exp(-U/J)$  is much faster than the spin fluctuation or doublon-doublon collision assisted decay which scale as  $\sim \exp(-U^2/J^2)$ . Further, the population of higher bands can be excluded, since  $U$  is always smaller than half the band gap. We also note that as the difference between  $U$  and the chemical potential is always positive, confinement assisted decay of doublons near the edge of the cloud is unlikely, as the accessible confinement energy is not very large, and the doublon tunneling rate is very small. Finally, a homogeneous compressible background is justified since most of the doublons are created in the central region of the trap, where the filling is highest, and decay at most within a few sites of where they are produced. The estimated travel distance for a random walk during the decay process is not more than  $\sqrt{\tau_{\text{D}}J/\hbar} \lesssim 10$  sites, which is less than the cloud radius.

We consider the decay of an isolated doublon moving in the homogeneous background of a compressible state of equilibrated single Fermions. The complete Hamiltonian of the system may be written as  $H = H_{\text{pf}} + H_{\text{d}} + H_{\text{fd}}$ , where  $H_{\text{pf}}$  describes the background fermions,  $H_{\text{d}}$  is the on-site energy of doublons and  $H_{\text{fd}}$  is the interaction of the doublon with the background fermions.

The strong Hubbard repulsion between the fermions leads to the concept of projection, where two fermions are forbidden from occupying the same site. In this case, the fermions can only hop in the presence of a hole on a neighboring site and are governed by the Hamiltonian

$$H_{\text{pf}} = -J \sum_{\langle ij \rangle, \sigma} (1 - n_{i\bar{\sigma}}) c_{i\sigma}^\dagger c_{j\sigma} (1 - n_{j\bar{\sigma}}), \quad (8.5)$$

where  $c_{i\sigma}^\dagger$  and  $c_{i\sigma}$  are the fermion creation and annihilation operators and  $n_{i,\sigma}$  is the number operator for fermions with spin  $\sigma$ . The spin opposite to  $\sigma$  is denoted by  $\bar{\sigma}$ . Expanding out this Hamiltonian we obtain  $H_{\text{pf}} = H_{\text{f}} + H_{\text{p}}$ , with

$$H_{\text{f}} = -J \sum_{\langle ij \rangle, \sigma} c_{i\sigma}^\dagger c_{j\sigma} - \mu \sum_{i,\sigma} c_{i\sigma}^\dagger c_{i\sigma}, \quad (8.6)$$

$$H_{\text{p}} = J \sum_{\langle ij \rangle, \sigma} (n_{i\bar{\sigma}} c_{i\sigma}^\dagger c_{j\sigma} + c_{i\sigma}^\dagger c_{j\sigma} n_{j\bar{\sigma}}), \quad (8.7)$$

where  $H_{\text{f}}$  describes the free Fermi sea and  $H_{\text{p}}$  describes the interaction induced by the projection and can be thought of as a process in which a fermion scatters

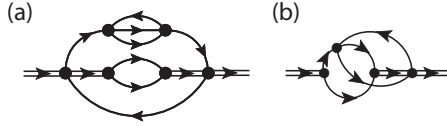


Figure 8.6: The double lines represent doubleton propagators, and the single lines fermion propagators. (a) Typical doubleton propagator diagram showing the creation of particle-hole pairs by both the doubleton and the projected fermions as well as annihilation of the doubleton into a pair of single fermions. (b) Typical example for a neglected diagram type.

off the Fermi sea and creates a particle-hole pair. We assume that the system is close to half filling with a chemical potential  $\mu = 0$ , but we confirmed that the result is not very sensitive to the precise value of the filling as shown by the shaded region in Figure 8.4. We neglect the term  $n_{i\bar{\sigma}}c_{i\sigma}^\dagger c_{j\bar{\sigma}} n_{j\bar{\sigma}}$  in  $H_p$  after ensuring that it leads to negligibly small corrections to the doubleton decay rate.

We now consider the propagation and decay of a doubleton in the background state of the projected Fermi sea. The on-site energy of the doubleton is  $H_d = U \sum_i d_i^\dagger d_i$ , where  $d^\dagger$  is a doubleton creation operator. The doubleton-fermion interaction  $H_{fd}$  is given by

$$H_{fd} = J \sum_{(ij)} \sum_{\sigma} (d_i^\dagger d_i + d_j^\dagger d_j + d_j^\dagger d_i) c_{i\sigma}^\dagger c_{j\sigma} + d_i (c_{i\downarrow}^\dagger c_{j\downarrow}^\dagger - c_{i\uparrow}^\dagger c_{j\uparrow}^\dagger) + \text{h.c.}, \quad (8.8)$$

where the terms describe: projecting out configurations with a doubleton and a fermion on the same site (first and second term), hopping of doubletons with back-flow of fermions (third term), and interconversion between a pair of single fermions and a doubleton (last term).

We now see that there are two different processes by which the doubleton can lose energy. It can create a large number of particle-hole pairs (through the first terms in  $H_{fd}$ ), each with an energy of on the order  $6J$ , or it can create a high energy particle-hole pair (through  $H_{fd}$ ), which is itself unstable and decays into a shower of particle-hole pairs (through the action of  $H_p$ ). The last process is the result of strong interaction between the fermions and must be taken into account in order to obtain an accurate estimate of the doubleton lifetime.

Our strategy for determining the doubleton lifetime is to compute the doubleton self-energy  $\Sigma(\omega)$  diagrammatically [199] and obtain the decay rate from  $\text{Im} \Sigma(U)$ , the imaginary part of the self-energy at  $\omega = U$ . We proceed by first obtaining the Green's function for the projected Fermi sea ( $H_f + H_p$ ) using a diagrammatic perturbation theory. Next, we use this Green's function in a resummation procedure to obtain  $\Sigma(\omega)$ . These steps can be treated as independent when the doubleton density is small, as the presence of the doubletons does not change the background fermion Green's functions. Throughout, we follow the

principle of maximizing the number of particle-hole pairs (see Figure 8.6a) at each order of perturbation theory. We do miss the class of diagrams in which interactions between fermions cannot be described by a fermion self-energy (see Figure 8.6b). We carry out our calculations in the zero temperature formalism. However, since we are looking at high energy processes ( $\omega \sim U$ ), finite temperatures will not have a large effect on the results as long as  $T \leq U$ .

Our theoretical analysis was constructed to capture the scaling parameter of the doublon lifetime at large  $U/6J$ , as it relies on generating a large number of particle-hole pairs. In this regime the theoretically computed value of the scaling exponent is  $\alpha_{\text{theo}} = 0.80$  close to half filling, which agrees well with the experimentally obtained value  $\alpha = 0.82(8)$ . The theory breaks down for small  $U/6J$ , leading to disagreement between experiment and theory in this regime (see Figure 8.4). Although the theory is not designed to predict the pre-exponential factor  $C$ , we find reasonable agreement between theory and experiment.

## *Conclusion*

The exponentially long lifetime of double occupancies has implications for the simulation of strongly correlated lattice models with ultracold atoms as it poses adiabaticity constraints on the sweep rates for the system parameters.

In addition, the long lifetime of the doublons also leads to the possibility of preparing and observing metastable states with finite density of doublons. An intriguing scenario is observing  $\eta$ -pairing of doublons and holes [215].

Finally, we point out that similar phenomena may be relevant to the issues of equilibration in the Bosonic Hubbard model. In recent experiments the equilibration of the density distribution of Bosonic atoms in a two dimensional optical lattice has been observed [151]. As the system relaxes towards equilibrium, the center of the trap heats up, which requires the increase in the number of doublons. The slow relaxation timescale observed in these experiments may reflect the *dual* problem to the one discussed in this chapter: slow rate of formation of doublons from a state containing only singly occupied sites and holes.



## 9 Outlook

The difficulty of describing the equilibrium state of a correlated condensed matter system is, for a large part, due to the complexity associated with handling the many-body wavefunction explicitly. Similar to the equilibrium, also the full non-equilibrium dynamics — as in the previous chapter — involve complex many-particle processes and are thus challenging to describe.

However, a full microscopically detailed description is frequently not required and it is more useful to work in terms of the macroscopically observable behavior rather than the particular wavefunction. The classical example of such an approach is the magnetic susceptibility  $\chi = \partial M / \partial H$ . It describes how a system changes its magnetization  $M$  when the magnetic field  $H$  changes. Here, the field is treated as a disturbance and the magnetization as the linear response. Within this linear response theory, the properties close to thermal equilibrium are described in terms of expectation values of observable quantities. The dynamics emerge as perturbative effects, leading to a significant reduction in analytical and numerical complexity.

If new quantum many-body phases are realized in experiments with ultracold atoms, the complete wavefunction will most probably not be observable. Equipping the experiments with probes that can be understood within the framework of linear response theory is therefore a major goal. Several probes to identify for example an antiferromagnetically ordered phase have been proposed. Superlattices, that rely on dynamically modifying the lattice potential to separate, bias, and merge lattice sites [216, 217], could provide access to spin correlations. Yet their applicability is limited to short-range effects. Noise correlations, where the atom shot noise in absorption images is detected [218, 219, 220, 19], can resolve long-range correlations but the signal is unfortunately very small. Finally, Bragg scattering [221] can provide access to magnetic order and to the dispersion relation. The latter approach is in close analogy to neutron scattering in solid state experiments and also a prime example for linear response but it needs access to the system under specific scattering angles.

This chapter provides an outlook on developing a new linear response probe for strongly correlated quantum gases in optical lattices. In the previous chapters, the double occupancy response of the system to a strong lattice modulation was observed in the regime of saturation. There, as a result of the modulation, the system's properties change drastically. For example, the number of holes increases, which in turn leads to a strong modification of the decay of double

occupancies. Since the system is highly excited, the view on the equilibrium state is obstructed.

We now explore the real-time build-up of double occupancies for short and weak lattice modulation close to equilibrium. If the system remains within linear response, the probe provides the link to numerical predictions on spin susceptibility and could be used as a sensitive thermometer in the lattice. The theoretical analysis and classification of this perturbation have stimulated different hypotheses [212, 211, 222, 172] but the question whether it can be treated within linear response theory has not been answered. It is also unclear experimentally whether the modulation strength can be reduced enough to remain in the regime of linear response.

The preparation of the system is according to the description in the previous chapters. We load about  $N = 50 \times 10^3$  atoms in a  $m_F = -9/2, -5/2$  mixture into the three-dimensional optical lattice with simple cubic symmetry and a depth between  $5E_r$  and  $10E_r$ . After letting the atoms thermalize for a short time, the depth of the three lattice beams  $V$  is modulated for a time period  $\tau$  with a modulation amplitude  $\delta V$ . The lattice depth is then quickly increased to  $30E_r$  in  $200\text{--}500\ \mu\text{s}$  to freeze further dynamics or decay of excitations. Subsequently, the double occupancy is determined using rf-spectroscopy.

The modulation leads to three kinds of dynamics of the double occupancy in the different regimes of modulation time.

In the top panel of Figure 9.1 the behavior on short timescales of a few modulation cycles is depicted. To obtain a good signal on these short timescales, the modulation amplitude of the potential depth is large,  $\delta V/V = 0.2$ . The system exhibits a non-dissipative oscillatory as well as linearly increasing response. The oscillations with the same frequency as the driving force can be viewed in analogy to a driven damped harmonic oscillator. Since  $1/\nu \approx 250\ \mu\text{s}$  is already comparable to the freezing time, the time resolution is limited and the absolute magnitude and phase of the oscillations are expected to be modified by the lattice freezing. However, the relative amplitudes and phases for different modulation frequencies can be extracted and compared reliably. The phase and amplitude behavior of the oscillations exhibit the typical resonance step and peak, respectively.

The underlying linear increase of the double occupancy signals dissipative dynamics and extends over some 20 modulation cycles (second panel in Figure 9.1). We extract the slope  $R = (\hbar/t)(\partial D/\partial \tau)$  by performing a linear regression on the data in this non-saturated regime. It is proportional to the energy dissipation rate and, within linear response, should be quadratic in the driving force.

The system exhibits saturation of the increase of the double occupancy only for long modulation times,  $\tau \gtrsim 40\hbar/U$ , as shown in the bottom panel in Figure 9.1. In the regime of saturation, the increasingly fast spontaneous decay



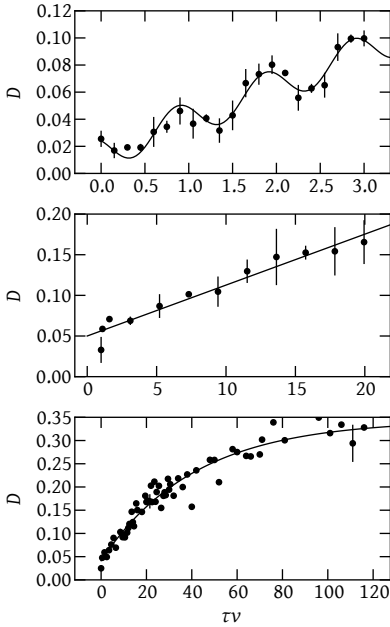


Figure 9.1: Three different regimes of the real-time dynamics of double occupancy build-up. In the three panels the fraction of atoms on doubly occupied sites is shown versus the modulation time for resonant modulation  $\nu = U/h$ . In the top panel a large modulation of  $\delta V/V = 0.2$  was chosen to show the coherent oscillations of the double occupancy on the time scale of the interaction energy  $U$ . The second panel demonstrates the linear increase of double occupancy for  $\delta V/V = 0.1$  and intermediate modulation times. In the bottom panel the saturation regime is depicted. All panels correspond to a Hubbard parameter of  $U/6t = 4.1$ , a lattice depth  $s = 7E_r$  and about  $N = 50 \times 10^3$  particles. The modulation frequency is close to  $U/h$ . Data points and errorbars are the mean and standard deviation of at least three realizations of the experiment for the same parameters.

of the excitations and the stimulated deexcitation by the modulation lead to a non-linearity and finally, for large times the rates of creation and decay cancel.

The dissipation rate for different modulation frequencies in the proximity of the  $\nu = U/h$  resonance is depicted in the top panel in Figure 9.2. Since, the modulation couples a singly occupied state with energy  $E$  to a doubly occupied state with energy  $E + h\nu$ , the dissipation rate should be proportional to the convolution of the density of states in the lower and upper Hubbard bands [171]. Their overlap is maximal at resonance where  $\nu = U/h$  and decreases until the bands do not overlap anymore. Approximating the density of states as rectangular, the dissipation rate should have triangular shape. Unfortunately, due to the scatter of the data points, the detailed shape can not yet be extracted from the data.

To analyze the scaling of the response with the modulation amplitude, we record many dissipation curves for different modulation frequencies and for different modulation amplitudes ranging from  $\delta V/V = 0.04$  to 0.15. For each modulation amplitude, the area under the spectral peak is integrated,  $A = \int R d\nu$ ,

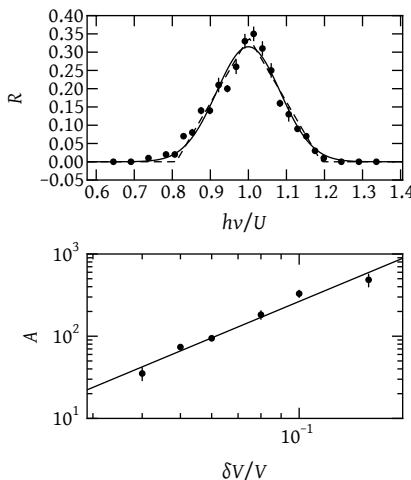


Figure 9.2: Top panel: spectrum of the double occupancy production rate  $R = (h/t)(\partial D/\partial \tau)$  for  $\delta V/V = 0.1$  and different modulation frequencies around the  $\nu = U/h$  resonance. The errorbars are the uncertainty estimate of the linear regressions. A triangular curve (dashed) as well as a Gaussian peak (solid) are fit to the data. For the bottom panel, several spectra for different modulation amplitudes have been recorded. The area under the peak is integrated,  $A = \int R dv$ , and plotted versus the modulation amplitude on a doubly logarithmic scale. Errorbars denote the uncertainty of the area integration.

and plotted against the modulation amplitude in the bottom panel of Figure 9.2. The integrated response  $A$  obeys a scaling law

$$A = A_0 \left( \frac{\delta V}{V} \right)^a \quad (9.1)$$

with  $A_0 = 27(13)$  kHz and  $a = 2.0(2)$ . The good agreement with  $A \propto (\delta V/V)^2$  indicates that lattice modulation leads to a linear response over a wide range of modulation strengths as long as the modulation time is not too long and no saturation is observed.

Equipped with this linear response probe, its dependence on certain parameters can now be explored. As lattice modulation only couples antiferromagnetic singlet bonds with configurations like  $\uparrow - \downarrow$  to double occupancies  $\uparrow\downarrow - 0$ , the doublon production rate directly reveals the singlet probability in the system. This singlet probability depends, among other parameters, sensitively on the temperature. In the Mott-insulating regime, where half the bonds are occupied by a singlet, the doublon production rate should therefore decrease with increasing temperature as the density decreases. Upon approaching the antiferromagnetically ordered state, it should increase further and signal the emergence of spin order [111].

Experimental effort is underway to create a lattice thermometer from this linear response probe and to characterize its dependence on other parameters like bandwidth, interaction energy, characteristic filling and confinement.

## Bibliography

- [1] P. Nozières and D. Pines. *The theory of quantum liquids* (Perseus Books, 1999)
- [2] J. R. Schrieffer. *Theory of superconductivity* (Perseus Books, 1999)
- [3] D. Jaksch, C. Bruder, J. I. Cirac, C. W. Gardiner, and P. Zoller. *Cold Bosonic Atoms in Optical Lattices*. Phys. Rev. Lett., **81**, 3108 (1998)
- [4] M. P. A. Fisher, P. B. Weichman, G. Grinstein, and D. S. Fisher. *Boson localization and the superfluid-insulator transition*. Phys. Rev. B, **40**, 546 (1989)
- [5] W. Hofstetter, J. I. Cirac, P. Zoller, E. Demler, and M. D. Lukin. *High-Temperature Superfluidity of Fermionic Atoms in Optical Lattices*. Phys. Rev. Lett., **89**, 220407 (2002)
- [6] R. Feynman. *Simulating physics with computers*. International Journal of Theoretical Physics, **21**, 467 (1982)
- [7] S. Lloyd. *Universal Quantum Simulators*. Science, **273**, 1073 (1996)
- [8] J. Hubbard. *Electron Correlations in Narrow Energy Bands*. Proc. R. Soc. A, **276**, 238 (1963)
- [9] N. W. Ashcroft and N. D. Mermin. *Solid State Physics* (Saunders College Publishing, Philadelphia, PA, 1976)
- [10] P. W. Anderson. *The Resonating Valence Bond State in  $\text{La}_2\text{CuO}_4$  and Superconductivity*. Science, **235**, 1196 (1987)
- [11] J. G. Bednorz and K. A. Müller. *Possible high  $T_c$  superconductivity in the  $\text{Ba-La-Cu-O}$  system*. Z. Phys. B, **64**, 189 (1986)
- [12] D. J. Scalapino. *The case for  $dx^2 - y^2$  pairing in the cuprate superconductors*. Phys. Rep., **250**, 329 (1995)
- [13] P. W. Anderson. *Superconductivity in High  $T_c$  Cuprates: The Cause is No Longer A Mystery*. Physica Scripta, **T102**, 10 (2002)
- [14] E. Lieb. *The Hubbard Model: Some Rigorous Results and Open Problems*. In *XIIIth International Congress on Mathematical Physics*, 392–412 (Int. Press, 1995)

- [15] M. Greiner, O. Mandel, T. Esslinger, T. W. Hänsch, and I. Bloch. *Quantum phase transition from a superfluid to a Mott insulator in a gas of ultracold atoms*. Nature, **415**, 39 (2002)
- [16] M. Köhl, H. Moritz, T. Stöferle, K. Günter, and T. Esslinger. *Fermionic Atoms in a Three Dimensional Optical Lattice: Observing Fermi Surfaces, Dynamics, and Interactions*. Phys. Rev. Lett., **94**, 080403 (2005)
- [17] T. Stöferle, H. Moritz, K. Günter, M. Köhl, and T. Esslinger. *Molecules of Fermionic Atoms in an Optical Lattice*. Phys. Rev. Lett., **96**, 030401 (2006)
- [18] M. Köhl, K. Günter, T. Stöferle, H. Moritz, and T. Esslinger. *Strongly interacting atoms and molecules in a 3D optical lattice*. J. Phys. B, **39**, S47 (2006)
- [19] T. Rom, T. Best, D. van Oosten, U. Schneider, S. Fölling, B. Paredes, and I. Bloch. *Free fermion antibunching in a degenerate atomic Fermi gas released from an optical lattice*. Nature, **444**, 733 (2006)
- [20] G. Modugno, F. Ferlaino, R. Heidemann, G. Roati, and M. Inguscio. *Production of a Fermi gas of atoms in an optical lattice*. Phys. Rev. A, **68**, 011601 (2003)
- [21] E. Ferlaino, E. De Mirandes, R. Heidemann, G. Roati, G. Modugno, and M. Inguscio. *Quasi-2D Bose-Fermi mixture in an optical lattice*. J. Phys. IV France, **1** (2003)
- [22] K. Günter, T. Stöferle, H. Moritz, M. Köhl, and T. Esslinger. *p-Wave Interactions in Low-Dimensional Fermionic Gases*. Phys. Rev. Lett., **95**, 230401 (2005)
- [23] K. Günter, T. Stöferle, H. Moritz, M. Köhl, and T. Esslinger. *Bose-Fermi Mixtures in a Three-Dimensional Optical Lattice*. Phys. Rev. Lett., **96**, 180402 (2006)
- [24] S. Ospelkaus, C. Ospelkaus, O. Wille, M. Succo, P. Ernst, K. Sengstock, and K. Bongs. *Localization of Bosonic Atoms by Fermionic Impurities in a Three-Dimensional Optical Lattice*. Phys. Rev. Lett., **96**, 180403 (2006)
- [25] C. Ospelkaus, S. Ospelkaus, L. Humbert, P. Ernst, K. Sengstock, and K. Bongs. *Ultracold Heteronuclear Molecules in a 3D Optical Lattice*. Phys. Rev. Lett., **97**, 120402 (2006)
- [26] T. Best, S. Will, U. Schneider, L. Hackermüller, D. van Oosten, I. Bloch, and D.-S. Lühmann. *Role of Interactions in  $^{87}\text{Rb}$ - $^{40}\text{K}$  Bose-Fermi Mixtures in a 3D Optical Lattice*. Phys. Rev. Lett., **102**, 030408 (2009)
- [27] J. K. Chin, D. E. Miller, Y. Liu, C. Stan, W. Setiawan, C. Sanner, K. Xu, and W. Ketterle. *Evidence for superfluidity of ultracold fermions in an optical*

- lattice*. Nature, **443**, 961 (2006)
- [28] A. Cavalleri, C. Tóth, C. W. Siders, J. A. Squier, F. Ráksi, P. Forget, and J. C. Kieffer. *Femtosecond Structural Dynamics in VO<sub>2</sub> during an Ultrafast Solid-Solid Phase Transition*. Phys. Rev. Lett., **87**, 237401 (2001)
- [29] L. Pezzè, L. Pitaevskii, A. Smerzi, S. Stringari, G. Modugno, E. de Mirandes, F. Ferlaino, H. Ott, G. Roati, and M. Inguscio. *Insulating Behavior of a Trapped Ideal Fermi Gas*. Phys. Rev. Lett., **93**, 120401 (2004)
- [30] H. Ott, E. de Mirandes, F. Ferlaino, G. Roati, G. Modugno, and M. Inguscio. *Collisionally Induced Transport in Periodic Potentials*. Phys. Rev. Lett., **92**, 160601 (2004)
- [31] S. Trebst, U. Schollwock, M. Troyer, and P. Zoller. *d-Wave Resonating Valence Bond States of Fermionic Atoms in Optical Lattices*. Phys. Rev. Lett., **96**, 250402 (2006)
- [32] B. Capogrosso Sansone, C. Trefzger, M. Lewenstein, P. Zoller, and G. Pupillo. *Quantum Phases of Cold Polar Molecules in 2D Optical Lattices*. Phys. Rev. Lett., **104**, 125301 (2010)
- [33] L. Pollet, J. D. Picon, H. P. Büchler, and M. Troyer. *Supersolid Phase with Cold Polar Molecules on a Triangular Lattice*. Phys. Rev. Lett., **104**, 125302 (2010)
- [34] B. Alvarez Fernández and J. A. Blanco. *The Hubbard model for the hydrogen molecule*. European Journal of Physics, **23**, 11 (2002)
- [35] G. Chiappe, E. Louis, E. SanFabian, and J. A. Verges. *Hubbard Hamiltonian for the hydrogen molecule*. Phys. Rev. B, **75**, 195104 (2007)
- [36] R. R. dos Santos. *Spin gap and superconductivity in the three-dimensional attractive Hubbard model*. Phys. Rev. B, **50**, 635 (1994)
- [37] R. Staudt, M. Dzierzawa, and A. Muramatsu. *Phase diagram of the three-dimensional Hubbard model at half filling*. Eur. Phys. J. B, **17**, 411 (2000)
- [38] E. Kozik, K. Van Houcke, E. Gull, L. Pollet, N. Prokof'ev, B. Svistunov, and M. Troyer. *Diagrammatic Monte Carlo for Correlated Fermions*. arxiv:0907.0863 (2009). 0907.0863
- [39] A. Georges, G. Kotliar, W. Krauth, and M. J. Rozenberg. *Dynamical mean-field theory of strongly correlated fermion systems and the limit of infinite dimensions*. Rev. Mod. Phys., **68**, 13 (1996)
- [40] P. A. Lee, N. Nagaosa, and X.-G. Wen. *Doping a Mott insulator: Physics of high-temperature superconductivity*. Rev. Mod. Phys., **78**, 17 (2006)

- [41] D. Jaksch and P. Zoller. *The cold atom Hubbard toolbox*. Ann. Phys., **315**, 52 (2005)
- [42] H. P. Büchler. *Microscopic Derivation of Hubbard Parameters for Cold Atomic Gases*. Phys. Rev. Lett., **104**, 090402 (2010)
- [43] W. Pauli. *The Connection Between Spin and Statistics*. Phys. Rev., **58**, 716 (1940)
- [44] A. J. Leggett. *Quantum Liquids (Bose Condensation and Cooper Pairing in Condensed-Matter Systems)* (Oxford University Press, 2006)
- [45] M. E. Peskin and D. V. Schroeder. *An Introduction to Quantum Field Theory* (Westview Press, 1995)
- [46] D. A. Butts and D. S. Rokhsar. *Trapped Fermi gases*. Phys. Rev. A, **55**, 4346 (1997)
- [47] Y. Castin. *Basic theory tools for degenerate Fermi gases*. In M. Inguscio, W. Ketterle, and C. Salomon (eds.), *Proceedings of the International School of Physics "Enrico Fermi"* (IOS Press, 2006)
- [48] L. D. Carr, G. V. Shlyapnikov, and Y. Castin. *Achieving a BCS Transition in an Atomic Fermi Gas*. Phys. Rev. Lett., **92**, 150404 (2004)
- [49] K. Huang. *Statistical Mechanics* (John Wiley and Sons, 1987), second edn.
- [50] V. S. Letokhov. *Narrowing of the Doppler Width in a Standing Wave*. Sov. J. Exp. Theor. Phys. Lett., **7**, 272 (1968)
- [51] R. H. Dicke. *The Effect of Collisions upon the Doppler Width of Spectral Lines*. Phys. Rev., **89**, 472 (1953)
- [52] C. S. Adams and E. Riis. *Laser cooling and trapping of neutral atoms*. Prog. Quant. Electr., **21**, 1 (1997)
- [53] R. Grimm and M. Weidemüller. *Optical dipole traps for neutral atoms*. Adv. At. Mol. Opt. Phys., **42**, 95 (1999)
- [54] I. Bloch. *Ultracold quantum gases in optical lattices*. Nat Phys, **1**, 23 (2005)
- [55] S. Chu, J. E. Bjorkholm, A. Ashkin, and A. Cable. *Experimental Observation of Optically Trapped Atoms*. Phys. Rev. Lett., **57**, 314 (1986)
- [56] M. D. Barrett, J. A. Sauer, and M. S. Chapman. *All-Optical Formation of an Atomic Bose-Einstein Condensate*. Phys. Rev. Lett., **87**, 010404 (2001)
- [57] S. R. Granade, M. E. Gehm, K. M. O'Hara, and J. E. Thomas. *All-Optical Production of a Degenerate Fermi Gas*. Phys. Rev. Lett., **88**, 120405 (2002)

- [58] J. Dalibard and C. Cohen Tannoudji. *Dressed-atom approach to atomic motion in laser light the dipole force revisited*. J. Opt. Soc. Am. B, **2**, 1707 (1985)
- [59] J. P. Gordon and A. Ashkin. *Motion of atoms in a radiation trap*. Phys. Rev. A, **21**, 1606 (1980)
- [60] F. Gerbier and Y. Castin. *Heating rates for an atom in a far-detuned optical lattice*. ArXiv e-prints (2010). 1002.5018
- [61] K. M. Jones, E. Tiesinga, P. D. Lett, and P. S. Julienne. *Ultracold photoassociation spectroscopy: Long-range molecules and atomic scattering*. Rev. Mod. Phys., **78**, 483 (2006)
- [62] J. D. Miller, R. A. Cline, and D. J. Heinzen. *Photoassociation spectrum of ultracold Rb atoms*. Phys. Rev. Lett., **71**, 2204 (1993)
- [63] N. Strohmaier. *Exploring the Hubbard model with ultracold fermionic atoms in an optical lattice*. Ph.D. thesis, ETH Zurich (2010)
- [64] U. Schneider, L. Hackermuller, S. Will, T. Best, I. Bloch, T. A. Costi, R. W. Helmes, D. Rasch, and A. Rosch. *Metallic and Insulating Phases of Repulsively Interacting Fermions in a 3D Optical Lattice*. Science, **322**, 1520 (2008)
- [65] V. L. Berezinskii. *Destruction of long-range order in one-dimensional and two-dimensional systems having a continuous symmetry group I. Classical systems*. Sov. Phys. JETP, **32**, 493 (1971)
- [66] J. M. Kosterlitz and D. J. Thouless. *Ordering, metastability and phase transitions in two-dimensional systems*. Journal of Physics C: Solid State Physics, **6**, 1181 (1973)
- [67] J. M. Kosterlitz. *The critical properties of the two-dimensional xy model*. Journal of Physics C: Solid State Physics, **7**, 1046 (1974)
- [68] Z. Hadzibabic, P. Kruger, M. Cheneau, B. Battelier, and J. Dalibard. *Berezinskii-Kosterlitz-Thouless crossover in a trapped atomic gas*. Nature, **441**, 1118 (2006)
- [69] V. Schweikhard, S. Tung, and E. A. Cornell. *Vortex Proliferation in the Berezinskii-Kosterlitz-Thouless Regime on a Two-Dimensional Lattice of Bose-Einstein Condensates*. Phys. Rev. Lett., **99**, 030401 (2007)
- [70] M. Greiner. *Ultracold quantum gases in three-dimensional optical lattice potentials*. Ph.D. thesis, LMU (2003)
- [71] H. Ott, E. de Mirandes, F. Ferlaino, G. Roati, V. Turck, G. Modugno, and M. Inguscio. *Radio Frequency Selective Addressing of Localized Atoms in a*

- Periodic Potential*. Phys. Rev. Lett., **93**, 120407 (2004)
- [72] V. Letokhov and V. Minogin. *Trapping and storage of atoms in a laser field*. Applied Physics A: Materials Science & Processing, **17**, 99 (1978)
- [73] G. Blanch. *Mathieu Functions*. In M. Abramowitz and I. A. Stegun (eds.), *Handbook of Mathematical Functions with Formulas, Graphs, and Mathematical Tables*, chap. 20 (Dover Publications, New York, 1972)
- [74] A. P. Mosk. *Atomic Gases at Negative Kinetic Temperature*. Phys. Rev. Lett., **95**, 040403 (2005)
- [75] W. Kohn. *Analytic Properties of Bloch Waves and Wannier Functions*. Phys. Rev., **115**, 809 (1959)
- [76] A. Daley. *Manipulation and Simulation of Cold Atoms in Optical Lattices*. Ph.D. thesis, Universität Innsbruck (2005)
- [77] M. Rigol and A. Muramatsu. *Quantum Monte Carlo study of confined fermions in one-dimensional optical lattices*. Phys. Rev. A, **69**, 053612 (2004)
- [78] M. Rigol and A. Muramatsu. *Confinement control by optical lattices*. Phys. Rev. A, **70**, 043627 (2004)
- [79] R. Jördens, L. Tarruell, D. Greif, T. Uehlinger, N. Strohmaier, H. Moritz, T. Esslinger, L. De Leo, C. Kollath, A. Georges, V. Scarola, L. Pollet, E. Burovski, E. Kozik, and M. Troyer. *Quantitative Determination of Temperature in the Approach to Magnetic Order of Ultracold Fermions in an Optical Lattice*. Phys. Rev. Lett., **104**, 180401 (2010)
- [80] M. Köhl. *Thermometry of fermionic atoms in an optical lattice*. Phys. Rev. A, **73**, 031601 (2006)
- [81] H. Feshbach. *Unified theory of nuclear reactions*. Ann. Phys., **5**, 357 (1958)
- [82] E. Tiesinga, B. J. Verhaar, and H. T. C. Stoof. *Threshold and resonance phenomena in ultracold ground-state collisions*. Phys. Rev. A, **47**, 4114 (1993)
- [83] A. J. Moerdijk, B. J. Verhaar, and A. Axelsson. *Resonances in ultracold collisions of  $^6\text{Li}$ ,  $^7\text{Li}$ , and  $^{23}\text{Na}$* . Phys. Rev. A, **51**, 4852 (1995)
- [84] C. Chin. *A simple model of Feshbach molecules*. arXiv:cond-mat/0506313v2, 5 (2005)
- [85] C. Chin, R. Grimm, P. Julienne, and E. Tiesinga. *Feshbach resonances in ultracold gases*. Rev. Mod. Phys., **82**, 1225 (2010)
- [86] S. Giorgini, L. P. Pitaevskii, and S. Stringari. *Theory of ultracold atomic Fermi gases*. Rev. Mod. Phys., **80**, 1215 (2008)



- [87] S. Ospelkaus, K.-K. Ni, D. Wang, M. H. G. de Miranda, B. Neyenhuis, G. Quemener, P. S. Julienne, J. L. Bohn, D. S. Jin, and J. Ye. *Quantum-State Controlled Chemical Reactions of Ultracold Potassium-Rubidium Molecules*. *Science*, **327**, 853 (2010)
- [88] J. J. Sakurai. *Modern Quantum Mechanics Revised Edition* (Addison-Wesley Publishing Company, 1994)
- [89] B. Gao. *Quantum-defect theory of atomic collisions and molecular vibration spectra*. *Phys. Rev. A*, **58**, 4222 (1998)
- [90] R. B. Diener and T.-L. Ho. *The Condition for Universality at Resonance and Direct Measurement of Pair Wavefunctions Using rf Spectroscopy*. arXiv:cond-mat/0405174v2 (2004)
- [91] H. Wang, A. N. Nikolov, J. R. Ensher, P. L. Gould, E. E. Eyler, W. C. Stwalley, J. P. Burke, J. L. Bohn, C. H. Greene, E. Tiesinga, C. J. Williams, and P. S. Julienne. *Ground-state scattering lengths for potassium isotopes determined by double-resonance photoassociative spectroscopy of ultracold  $^{39}\text{K}$* . *Phys. Rev. A*, **62**, 052704 (2000)
- [92] J. Dalibard. *Collisional dynamics of ultra-cold atomic gases*. In M. Inguscio, S. Stringari, and C. Wieman (eds.), *Proceedings of the International School of Physics "Enrico Fermi"* (IOS Press, 1998)
- [93] S. Inouye, M. R. Andrews, J. Stenger, H.-J. Miesner, D. M. Stamper Kurn, and W. Ketterle. *Observation of Feshbach resonances in a Bose-Einstein condensate*. *Nature*, **392**, 151 (1998)
- [94] T. V. Tscherbul, T. Calarco, I. Lesanovsky, R. V. Krems, A. Dalgarno, and J. Schmiedmayer. *rf-field-induced Feshbach resonances*. *Phys. Rev. A*, **81**, 050701 (2010)
- [95] P. O. Fedichev, Y. Kagan, G. V. Shlyapnikov, and J. T. M. Walraven. *Influence of Nearly Resonant Light on the Scattering Length in Low-Temperature Atomic Gases*. *Phys. Rev. Lett.*, **77**, 2913 (1996)
- [96] M. Theis, G. Thalhammer, K. Winkler, M. Hellwig, G. Ruff, R. Grimm, and J. H. Denschlag. *Tuning the Scattering Length with an Optically Induced Feshbach Resonance*. *Phys. Rev. Lett.*, **93**, 123001 (2004)
- [97] M. Bartenstein, A. Altmeyer, S. Riedl, S. Jochim, C. Chin, J. H. Denschlag, and R. Grimm. *Crossover from a Molecular Bose-Einstein Condensate to a Degenerate Fermi Gas*. *Phys. Rev. Lett.*, **92**, 120401 (2004)
- [98] T. Bourdel, L. Khaykovich, J. Cubizolles, J. Zhang, F. Chevy, M. Teichmann, L. Tarruell, S. J. J. M. F. Kokkelmans, and C. Salomon. *Ex-*

- perimental Study of the BEC-BCS Crossover Region in Lithium 6.* Phys. Rev. Lett., **93**, 050401 (2004)
- [99] M. W. Zwierlein, J. R. Abo Shaeer, A. Schirotzek, C. H. Schunck, and W. Ketterle. *Vortices and superfluidity in a strongly interacting Fermi gas.* Nature, **435**, 1047 (2005)
- [100] Q. Chen, Y. He, and K. Chien, Chih-Chun and Levin. *Theory of Radio Frequency Spectroscopy Experiments in Ultracold Fermi Gases and Their Relation to Photoemission Experiments in the Cuprates.* 0810.1940 (2008)
- [101] G. F. Gribakin and V. V. Flambaum. *Calculation of the scattering length in atomic collisions using the semiclassical approximation.* Phys. Rev. A, **48**, 546 (1993)
- [102] M. H. Szymanska, K. Goral, T. Köhler, and K. Burnett. *Conventional character of the BCS-BEC crossover in ultracold gases of  $^{40}\text{K}$ .* Phys. Rev. A, **72**, 013610 (2005)
- [103] E. L. Bolda, E. Tiesinga, and P. S. Julienne. *Effective-scattering-length model of ultracold atomic collisions and Feshbach resonances in tight harmonic traps.* Phys. Rev. A, **66**, 013403 (2002)
- [104] G. Bruun, Y. Castin, R. Dum, and K. Burnett. *BCS theory for trapped ultracold fermions.* Eur. Phys. J. D, **7**, 433 (1999)
- [105] M. Holland, S. J. J. M. F. Kokkelmans, M. L. Chiofalo, and R. Walser. *Resonance Superfluidity in a Quantum Degenerate Fermi Gas.* Phys. Rev. Lett., **87**, 120406 (2001)
- [106] T.-L. Ho. *Universal Thermodynamics of Degenerate Quantum Gases in the Unitarity Limit.* Phys. Rev. Lett., **92**, 090402 (2004)
- [107] D. S. Petrov, C. Salomon, and G. V. Shlyapnikov. *Weakly Bound Dimers of Fermionic Atoms.* Phys. Rev. Lett., **93**, 090404 (2004)
- [108] B. Gao. *Binding energy and scattering length for diatomic systems.* J. Phys. B, **37**, 4273 (2004)
- [109] E. Tiesinga, C. J. Williams, F. H. Mies, and P. S. Julienne. *Interacting atoms under strong quantum confinement.* Phys. Rev. A, **61**, 063416 (2000)
- [110] T. Busch, B.-G. Englert, K. Rzazewski, and M. Wilkens. *Two Cold Atoms in a Harmonic Trap.* Found. Phys., **28**, 549 (1998)
- [111] F. Werner, O. Parcollet, A. Georges, and S. R. Hassan. *Interaction-Induced Adiabatic Cooling and Antiferromagnetism of Cold Fermions in Optical Lattices.* Phys. Rev. Lett., **95**, 056401 (2005)

- [112] A. Georges. *Ultra-Cold Fermi Gases*. In M. Inguscio, W. Ketterle, and C. Salomon (eds.), *Proceedings of the International School of Physics "Enrico Fermi"*, 477–533 (IOS Press, 2007)
- [113] J. Oitmaa, C. Hamer, and W. Zheng. *Series expansion methods for strongly interacting lattice models* (Cambridge University Press, Cambridge, 2006)
- [114] J. A. Henderson, J. Oitmaa, and M. C. B. Ashley. *High-temperature expansion for the single-band Hubbard model*. *Phys. Rev. B*, **46**, 6328 (1992)
- [115] D. F. B. ten Haaf and J. M. J. van Leeuwen. *High-temperature series expansions for the Hubbard model*. *Phys. Rev. B*, **46**, 6313 (1992)
- [116] V. W. Scarola, L. Pollet, J. Oitmaa, and M. Troyer. *Discerning Incompressible and Compressible Phases of Cold Atoms in Optical Lattices*. *Phys. Rev. Lett.*, **102**, 135302 (2009)
- [117] H. Moritz, T. Stöferle, M. Köhl, and T. Esslinger. *Exciting Collective Oscillations in a Trapped 1D Gas*. *Phys. Rev. Lett.*, **91**, 250402 (2003)
- [118] T. Stöferle, H. Moritz, C. Schori, M. Köhl, and T. Esslinger. *Transition from a Strongly Interacting 1D Superfluid to a Mott Insulator*. *Phys. Rev. Lett.*, **92**, 130403 (2004)
- [119] C. Schori, T. Stöferle, H. Moritz, M. Köhl, and T. Esslinger. *Excitations of a Superfluid in a Three-Dimensional Optical Lattice*. *Phys. Rev. Lett.*, **93**, 240402 (2004)
- [120] T. Stöferle. *Exploring Atomic Quantum Gases in Optical Lattices*. Ph.D. thesis, ETH Zurich (2005)
- [121] H. Moritz. *One-dimensional Atomic Gases*. Ph.D. thesis, ETH Zurich (2006)
- [122] K. J. Günter. *Interacting Fermi gases and Bose-Fermi mixtures in optical lattices*. Ph.D. thesis, ETH Zurich (2007)
- [123] H. Moritz, T. Stöferle, K. Günter, M. Köhl, and T. Esslinger. *Confinement Induced Molecules in a 1D Fermi Gas*. *Phys. Rev. Lett.*, **94**, 210401 (2005)
- [124] L. Ricci, M. Weidemüller, T. Esslinger, A. Hemmerich, C. Zimmermann, V. Vuletic, W. König, and T. W. Hänsch. *A compact grating-stabilized diode laser system for atomic physics*. *Opt. Comm.*, **117**, 541 (1995)
- [125] G. C. Bjorklund, M. D. Levenson, W. Lenth, and C. Ortiz. *Frequency modulation (FM) spectroscopy*. *Appl. Phys. B*, **32**, 145 (1983)
- [126] U. Schünemann, H. Engler, R. Grimm, M. Weidemüller, and M. Zielonkowski. *Simple scheme for tunable frequency offset locking of two lasers*.

- Rev. Sci. Instrum., **70**, 242 (1999)
- [127] T. Hänsch and A. Schawlow. *Cooling of gases by laser radiation*. Optics Communications, **13**, 68 (1975)
- [128] E. L. Raab, M. Prentiss, A. Cable, S. Chu, and D. E. Pritchard. *Trapping of Neutral Sodium Atoms with Radiation Pressure*. Phys. Rev. Lett., **59**, 2631 (1987)
- [129] W. D. Phillips. *Nobel Lecture: Laser cooling and trapping of neutral atoms*. Rev. Mod. Phys., **70**, 721 (1998)
- [130] H. J. Metcalf and P. v. d. Straten. *Laser Cooling and Trapping* (Springer, 1999)
- [131] N. Bendali, H. T. Duong, and J. L. Vialle. *High-resolution laser spectroscopy on the  $D_1$  and  $D_2$  lines of  $^{39,40,41}\text{K}$  using RF modulated laser light*. J. Phys. B, **14**, 4231 (1981)
- [132] P. D. Lett, R. N. Watts, C. I. Westbrook, W. D. Phillips, P. L. Gould, and H. J. Metcalf. *Observation of Atoms Laser Cooled below the Doppler Limit*. Phys. Rev. Lett., **61**, 169 (1988)
- [133] M. Greiner, I. Bloch, T. W. Hänsch, and T. Esslinger. *Magnetic transport of trapped cold atoms over a large distance*. Phys. Rev. A, **63**, 031401 (2001)
- [134] T. Esslinger, I. Bloch, and T. W. Hänsch. *Bose-Einstein condensation in a quadrupole-Ioffe-configuration trap*. Phys. Rev. A, **58**, R2664 (1998)
- [135] K. B. Davis, M.-O. Mewes, M. A. Joffé, M. R. Andrews, and W. Ketterle. *Evaporative Cooling of Sodium Atoms*. Phys. Rev. Lett., **74**, 5202 (1995)
- [136] W. Petrich, M. H. Anderson, J. R. Ensher, and E. A. Cornell. *Stable, Tightly Confining Magnetic Trap for Evaporative Cooling of Neutral Atoms*. Phys. Rev. Lett., **74**, 3352 (1995)
- [137] R. Jördens. *A Radio Frequency Source for the Preparation of Quantum States*. Diploma thesis, ETH Zurich (2006)
- [138] C. Zener. *Non-Adiabatic Crossing of Energy Levels*. Proc. R. Soc. Lond. A, **137**, 696 (1932)
- [139] C. A. Regal and D. S. Jin. *Measurement of Positive and Negative Scattering Lengths in a Fermi Gas of Atoms*. Phys. Rev. Lett., **90**, 230404 (2003)
- [140] C. A. Regal, M. Greiner, and D. S. Jin. *Observation of Resonance Condensation of Fermionic Atom Pairs*. Phys. Rev. Lett., **92**, 040403 (2004)

- [141] N. Strohmaier, D. Greif, R. Jördens, L. Tarruell, H. Moritz, T. Esslinger, R. Sensarma, D. Pekker, E. Altman, and E. Demler. *Observation of Elastic Doublon Decay in the Fermi-Hubbard Model*. Phys. Rev. Lett., **104**, 080401 (2010)
- [142] M. Gustavsson, E. Haller, M. J. Mark, J. G. Danzl, G. Rojas Kopeinig, and H.-C. Nagerl. *Control of Interaction-Induced Dephasing of Bloch Oscillations*. Phys. Rev. Lett., **100**, 080404 (2008)
- [143] M. B. Gray, D. A. Shaddock, C. C. Harb, and H.-A. Bachor. *Photodetector designs for low-noise, broadband, and high-power applications*. Rev. Sci. Instrum., **69**, 3755 (1998)
- [144] P. C. D. Hobbs. *Building Electro-Optical Systems: Making It All Work* (Wiley-Interscience, 2000), 1 edn.
- [145] O. Morsch and M. Oberthaler. *Dynamics of Bose-Einstein condensates in optical lattices*. Rev. Mod. Phys., **78**, 179 (2006)
- [146] S. Friebel, C. D'Andrea, J. Walz, M. Weitz, and T. W. Hänsch. *CO<sub>2</sub>-laser optical lattice with cold rubidium atoms*. Phys. Rev. A, **57**, R20 (1998)
- [147] P. L. Gould, G. A. Ruff, and D. E. Pritchard. *Diffraction of atoms by light: The near-resonant Kapitza-Dirac effect*. Phys. Rev. Lett., **56**, 827 (1986)
- [148] V. Ruuska and P. Törmä. *Quantum transport of non-interacting Fermi gas in an optical lattice combined with harmonic trapping*. New J. Phys., **6**, 59 (2004)
- [149] N. Strohmaier, Y. Takasu, K. Günter, R. Jördens, M. Köhl, H. Moritz, and T. Esslinger. *Interaction-Controlled Transport of an Ultracold Fermi Gas*. Phys. Rev. Lett., **99**, 220601 (2007)
- [150] C. D. Fertig, K. M. O'Hara, J. H. Huckans, S. L. Rolston, W. D. Phillips, and J. V. Porto. *Strongly Inhibited Transport of a Degenerate 1D Bose Gas in a Lattice*. Phys. Rev. Lett., **94**, 120403 (2005)
- [151] C.-L. Hung, X. Zhang, N. Gemelke, and C. Chin. *Slow Mass Transport and Statistical Evolution of an Atomic Gas across the Superfluid-Mott-Insulator Transition*. Phys. Rev. Lett., **104**, 160403 (2010)
- [152] U. Schneider, L. Hackermüller, J. P. Ronzheimer, S. Will, S. Braun, T. Best, I. Bloch, E. Demler, S. Mandt, D. Rasch, and A. Rosch. *Breakdown of diffusion: From collisional hydrodynamics to a continuous quantum walk in a homogeneous Hubbard model*. ArXiv e-prints (2010). 1005.3545
- [153] D. A. Steck. *Rubidium 87 D Line Data* (2010). <http://steck.us/alkalidata/>

- [154] G. Reinaudi, T. Lahaye, Z. Wang, and D. Guéry Odelin. *Strong saturation absorption imaging of dense clouds of ultracold atoms*. *Opt. Lett.*, **32**, 3143 (2007)
- [155] H. Wang, P. L. Gould, and W. C. Stwalley. *Long-range interaction of the  $^{39}\text{K}(4s)+^{39}\text{K}(4p)$  asymptote by photoassociative spectroscopy. I. The  $0_g^-$  pure long-range state and the long-range potential constants*. *The Journal of Chemical Physics*, **106**, 7899 (1997)
- [156] T. G. Tiecke. *Potassium Properties* (2010). <http://staff.science.uva.nl/~tgtiecke/PotassiumProperties.pdf>
- [157] C. Regal. *Experimental realization of BCS-BEC crossover physics with a Fermi gas of atoms*. Ph.D. thesis, University of Colorado (2005)
- [158] T. Loftus, C. A. Regal, C. Ticknor, J. L. Bohn, and D. S. Jin. *Resonant Control of Elastic Collisions in an Optically Trapped Fermi Gas of Atoms*. *Phys. Rev. Lett.*, **88**, 173201 (2002)
- [159] C. A. Regal, C. Ticknor, J. L. Bohn, and D. S. Jin. *Creation of ultracold molecules from a Fermi gas of atoms*. *Nature*, **424**, 47 (2003)
- [160] C. A. Regal, M. Greiner, and D. S. Jin. *Lifetime of Molecule-Atom Mixtures near a Feshbach Resonance in K*. *Phys. Rev. Lett.*, **92**, 083201 (2004)
- [161] C. A. Regal, C. Ticknor, J. L. Bohn, and D. S. Jin. *Tuning p-Wave Interactions in an Ultracold Fermi Gas of Atoms*. *Phys. Rev. Lett.*, **90**, 053201 (2003)
- [162] B. DeMarco. *Quantum Behavior of an Atomic Fermi Gas*. Ph.D. thesis, University of Colorado (2001)
- [163] E. Hodby, S. T. Thompson, C. A. Regal, M. Greiner, A. C. Wilson, D. S. Jin, E. A. Cornell, and C. E. Wieman. *Production Efficiency of Ultracold Feshbach Molecules in Bosonic and Fermionic Systems*. *Phys. Rev. Lett.*, **94**, 120402 (2005)
- [164] R. Jördens, N. Strohmaier, K. Günter, H. Moritz, and T. Esslinger. *A Mott insulator of fermionic atoms in an optical lattice*. *Nature (London)*, **455**, 204 (2008)
- [165] N. F. Mott. *Metal Insulator Transitions* (Taylor and Francis, London, 1990)
- [166] M. Imada, A. Fujimori, and Y. Tokura. *Metal-insulator transitions*. *Rev. Mod. Phys.*, **70**, 1039 (1998)
- [167] M. Rigol, A. Muramatsu, G. G. Batrouni, and R. T. Scalettar. *Local Quantum Criticality in Confined Fermions on Optical Lattices*. *Phys. Rev. Lett.*, **91**, 130403 (2003)

- [168] F. Gebhard. *The Mott metal-insulator transition – models and methods* (Springer, New York, 1997)
- [169] F. Gerbier, S. Fölling, A. Widera, and I. Bloch. *Visibility of a Bose-condensed gas released from an optical lattice at finite temperatures*. arXiv:cond-mat/0701420v1 (2007)
- [170] F. Gerbier, S. Fölling, A. Widera, O. Mandel, and I. Bloch. *Probing Number Squeezing of Ultracold Atoms across the Superfluid-Mott Insulator Transition*. Phys. Rev. Lett., **96**, 090401 (2006)
- [171] W. F. Brinkman and T. M. Rice. *Single-Particle Excitations in Magnetic Insulators*. Phys. Rev. B, **2**, 1324 (1970)
- [172] C. Kollath, A. Iucci, I. P. McCulloch, and T. Giamarchi. *Modulation spectroscopy with ultracold fermions in an optical lattice*. Phys. Rev. A, **74**, 041604 (2006)
- [173] S. D. Huber, B. Theiler, E. Altman, and G. Blatter. *Amplitude Mode in the Quantum Phase Model*. Phys. Rev. Lett., **100**, 050404 (2008)
- [174] S. Trotzky, L. Pollet, F. Gerbier, U. Schnorrberger, I. Bloch, N. V. Prokof'ev, B. Svistunov, and M. Troyer. *Suppression of the critical temperature for superfluidity near the Mott transition: validating a quantum simulator*. ArXiv e-prints (2009). 0905.4882
- [175] D. M. Weld, P. Medley, H. Miyake, D. Hucul, D. Pritchard, and W. Ketterle. *Spin Gradient Thermometry for Ultracold Atoms in Optical Lattices*. Phys. Rev. Lett., **103**, 245301 (2009)
- [176] C. Kittel. *Physical Theory of Ferromagnetic Domains*. Rev. Mod. Phys., **21**, 541 (1949)
- [177] L. De Leo, C. Kollath, A. Georges, M. Ferrero, and O. Parcollet. *Trapping and Cooling Fermionic Atoms into Mott and Néel States*. Phys. Rev. Lett., **101**, 210403 (2008)
- [178] P. Werner, A. Comanac, L. de'Medici, M. Troyer, and A. J. Millis. *Continuous-Time Solver for Quantum Impurity Models*. Phys. Rev. Lett., **97**, 076405 (2006)
- [179] C. Hung, X. Zhang, N. Gemelke, and C. Chin. *Slow Mass Transport and Statistical Evolution of An Atomic Gas Across the Superfluid-Mott Insulator Transition*. 1003.0855 (2010)
- [180] L. M. Milne Thomson. *Elliptic Integrals*. In M. Abramowitz and I. A. Stegun (eds.), *Handbook of Mathematical Functions with Formulas, Graphs, and Mathematical Tables*, chap. 17 (Dover Publications, New York, 1972)

- [181] A. W. Sandvik. *Critical Temperature and the Transition from Quantum to Classical Order Parameter Fluctuations in the Three-Dimensional Heisenberg Antiferromagnet*. Phys. Rev. Lett., **80**, 5196 (1998)
- [182] S. Wessel. *Critical entropy of quantum Heisenberg magnets on simple-cubic lattices*. Phys. Rev. B, **81**, 052405 (2010)
- [183] E. Burovski, E. Kozik, N. Prokof'ev, B. Svistunov, and M. Troyer. *Critical Temperature Curve in BEC-BCS Crossover*. Phys. Rev. Lett., **101**, 090402 (2008)
- [184] A. Koetsier, R. A. Duine, I. Bloch, and H. T. C. Stoof. *Achieving the Néel state in an optical lattice*. Phys. Rev. A, **77**, 023623 (2008)
- [185] W. Ketterle and M. W. Zwierlein. *Making, probing and understanding ultracold Fermi gases*. In M. Inguscio, W. Ketterle, and C. Salomon (eds.), *Proceedings of the International School of Physics "Enrico Fermi"*, vol. 31, 247–422 (IOS Press, 2008)
- [186] E. G. Moon, P. Nikolic, and S. Sachdev. *Superfluid-Insulator Transitions of the Fermi Gas with Near-Unitary Interactions in a Periodic Potential*. Phys. Rev. Lett., **99**, 230403 (2007)
- [187] A. M. Rey, B. L. Hu, E. Calzetta, A. Roura, and C. W. Clark. *Nonequilibrium dynamics of optical-lattice-loaded Bose-Einstein-condensate atoms: Beyond the Hartree-Fock-Bogoliubov approximation*. Phys. Rev. A, **69**, 033610 (2004)
- [188] J. Gea Banacloche, A. M. Rey, G. Pupillo, C. J. Williams, and C. W. Clark. *Mean-field treatment of the damping of the oscillations of a one-dimensional Bose gas in an optical lattice*. Phys. Rev. A, **73**, 013605 (2006)
- [189] M. Rigol, V. Rousseau, R. T. Scalettar, and R. R. P. Singh. *Collective Oscillations of Strongly Correlated One-Dimensional Bosons on a Lattice*. Phys. Rev. Lett., **95**, 110402 (2005)
- [190] E. Altman, A. Polkovnikov, E. Demler, B. I. Halperin, and M. D. Lukin. *Superfluid-Insulator Transition in a Moving System of Interacting Bosons*. Phys. Rev. Lett., **95**, 020402 (2005)
- [191] R. Micnas, J. Ranninger, and S. Robaszkiewicz. *Superconductivity in narrow-band systems with local nonretarded attractive interactions*. Rev. Mod. Phys., **62**, 113 (1990)
- [192] H. Zhai and T.-L. Ho. *Superfluid-Insulator Transition of Strongly Interacting Fermi Gases in Optical Lattices*. Phys. Rev. Lett., **99**, 100402 (2007)
- [193] M. Snoek and W. Hofstetter. *Two-dimensional dynamics of ultracold atoms in optical lattices*. Phys. Rev. A, **76**, 051603 (2007)



- [194] C. Hooley and J. Quintanilla. *Single-Atom Density of States of an Optical Lattice*. Phys. Rev. Lett., **93**, 080404 (2004)
- [195] G. Orso, L. P. Pitaevskii, and S. Stringari. *Umklapp Collisions and Center-of-Mass Oscillations of a Trapped Fermi Gas*. Phys. Rev. Lett., **93**, 020404 (2004)
- [196] M. Wouters and G. Orso. *Two-body problem in periodic potentials*. Phys. Rev. A, **73**, 012707 (2006)
- [197] M. Keller, W. Metzner, and U. Schollwöck. *Dynamical Mean-Field Theory for Pairing and Spin Gap in the Attractive Hubbard Model*. Phys. Rev. Lett., **86**, 4612 (2001)
- [198] M. Wouters, J. Tempere, and J. T. Devreese. *Path integral formulation of the tunneling dynamics of a superfluid Fermi gas in an optical potential*. Phys. Rev. A, **70**, 013616 (2004)
- [199] R. Sensarma, D. Pekker, E. Altman, E. Demler, N. Strohmaier, D. Greif, R. Jördens, L. Tarruell, H. Moritz, and T. Esslinger. *Lifetime of double occupancies in the Fermi-Hubbard model*. ArXiv e-prints (2010). 1001.3881
- [200] E. H. Lieb and W. Liniger. *Exact Analysis of an Interacting Bose Gas. I. The General Solution and the Ground State*. Phys. Rev., **130**, 1605 (1963)
- [201] U. Schollwöck. *The density-matrix renormalization group*. Reviews of Modern Physics, **77**, 259 (2005)
- [202] M. Rigol, V. Dunjko, and M. Olshanii. *Thermalization and its mechanism for generic isolated quantum systems*. Nature, **452**, 854 (2008)
- [203] T. Kinoshita, T. Wenger, and D. S. Weiss. *A quantum Newton's cradle*. Nature, **440**, 900 (2006)
- [204] I. Bloch, J. Dalibard, and W. Zwerger. *Many-body physics with ultracold gases*. Rev. Mod. Phys., **80**, 885 (2008)
- [205] V. Perebeinos and P. Avouris. *Phonon and Electronic Nonradiative Decay Mechanisms of Excitons in Carbon Nanotubes*. Phys. Rev. Lett., **101**, 057401 (2008)
- [206] G. M. Müller, J. Walowski, M. Djordjevic, G.-X. Miao, A. Gupta, A. V. Ramos, K. Gehrke, V. Moshnyaga, K. Samwer, J. Schmalhorst, A. Thomas, A. Hutten, G. Reiss, J. S. Moodera, and M. Munzenberg. *Spin polarization in half-metals probed by femtosecond spin excitation*. Nature Materials, **8**, 56 (2009)

- [207] G. E. Brown and W. Weise. *Pion scattering and isobars in nuclei*. Phys. Rep., **22**, 279 (1975)
- [208] D. J. Hilton, R. P. Prasankumar, S. Fourmaux, A. Cavalleri, D. Brassard, M. A. El Khakani, J. C. Kieffer, A. J. Taylor, and R. D. Averitt. *Enhanced Photosusceptibility near  $T_c$  for the Light-Induced Insulator-to-Metal Phase Transition in Vanadium Dioxide*. Phys. Rev. Lett., **99**, 226401 (2007)
- [209] R. D. Averitt and A. J. Taylor. *Ultrafast optical and far-infrared quasiparticle dynamics in correlated electron materials*. J. Phys.: Condens. Matter, **14**, R1357 (2002)
- [210] K. Winkler, G. Thalhammer, F. Lang, R. Grimm, J. Hecker Denschlag, A. J. Daley, A. Kantian, H. P. Büchler, and P. Zoller. *Repulsively bound atom pairs in an optical lattice*. Nature, **441**, 853 (2006)
- [211] R. Sensarma, D. Pekker, M. D. Lukin, and E. Demler. *Modulation Spectroscopy and Dynamics of Double Occupancies in a Fermionic Mott Insulator*. Phys. Rev. Lett., **103**, 035303 (2009)
- [212] F. Hassler and S. D. Huber. *Coherent pumping of a Mott insulator: Fermi golden rule versus Rabi oscillations*. Phys. Rev. A, **79**, 021607 (2009)
- [213] R. G. Miller. *The jackknife - a review*. Biometrika, **61**, 1 (1974)
- [214] B. Efron. *Bootstrap Methods: Another Look at the Jackknife*. Ann. Statist., **7**, 1 (1979)
- [215] A. Rosch, D. Rasch, B. Binz, and M. Vojta. *Metastable Superfluidity of Repulsive Fermionic Atoms in Optical Lattices*. Phys. Rev. Lett., **101**, 265301 (2008)
- [216] S. Trotzky, P. Cheinet, S. Fölling, M. Feld, U. Schnorrberger, A. M. Rey, A. Polkovnikov, E. A. Demler, M. D. Lukin, and I. Bloch. *Time-Resolved Observation and Control of Superexchange Interactions with Ultracold Atoms in Optical Lattices*. Science, **319**, 295 (2008)
- [217] P. J. Lee, M. Anderlini, B. L. Brown, J. Sebby Strabley, W. D. Phillips, and J. V. Porto. *Sublattice Addressing and Spin-Dependent Motion of Atoms in a Double-Well Lattice*. Phys. Rev. Lett., **99**, 020402 (2007)
- [218] E. Altman, E. Demler, and M. D. Lukin. *Probing many-body states of ultracold atoms via noise correlations*. Phys. Rev. A, **70**, 013603 (2004)
- [219] G. M. Bruun, O. F. Syljuåsen, K. G. L. Pedersen, B. M. Andersen, E. Demler, and A. S. Sørensen. *Antiferromagnetic noise correlations in optical lattices*. Phys. Rev. A, **80**, 033622 (2009)

- [220] S. Fölling, F. Gerbier, A. Widera, O. Mandel, T. Gericke, and I. Bloch. *Spatial quantum noise interferometry in expanding ultracold atom clouds*. *Nature*, **434**, 481 (2005)
- [221] T. A. Corcovilos, S. K. Baur, J. M. Hitchcock, E. J. Mueller, and R. G. Hulet. *Detecting antiferromagnetism of atoms in an optical lattice via optical Bragg scattering*. *Phys. Rev. A*, **81**, 013415 (2010)
- [222] F. Hassler, A. Rüegg, M. Sigrist, and G. Blatter. *Dynamical Unbinding Transition in a Periodically Driven Mott Insulator*. *Phys. Rev. Lett.*, **104**, 220402 (2010)



## *Acknowledgments*

Many people have contributed their share to the completion of my thesis.

First of all, the special flair in Tilman Esslinger's group has been very advantageous in many aspects and I am indebted to him for letting me benefit from his style of encouraging creative collaborative work.

All of my experiments were a joint effort of the entire lattice team. I owe my knowledge about the machine and many great hours in the lab to Niels Strohmaier who shared my time as a Ph. D. student and to our predecessors on the apparatus, Henning Moritz, Kenneth Günter, Thilo Stöferle, Yosuke Takasu, and Michael Köhl. The current generation, Daniel Greif, Leticia Tarruell, and Thomas Uehlinger, has been advancing the experiment with great activity and enthusiasm and will certainly continue to do so successfully.

The other two experimental teams were a big source of fruitful discussion and always helpfully providing insight, advice, and material where needed. Among them are the first-generation atom-laser lineup which also hosted my work as diploma student with Tobias Donner, Toni Öttl, Stephan Ritter, Thomas Bourdel and Christine Guerlin as well as the promising current "quantum wonderland" team with Ferdinand Brennecke, Kristian Baumann, Rafael Mottl, and Silvan Leinss and finally Jakob Meineke, Torben Müller, Bruno Zimmermann, and Jean-Philippe Brantut who are steering the ambitious and powerful Lithium setup.

A special thanks goes to the hundred unnamed semester and master students that contributed to the various experiments and especially to the new SOLACE setup.

I am also grateful to Veronica Bürgisser and Alexander Frank, not only for relieving me of so much tedious and difficult administrative and electronics work but also for being a courageous part of the group and for doing much more than expected.

I have shared many pleasant hours with people from the entire group, Tilman, Veronica, Alexander, the old and new postdocs, the Ph. D., master, and semester students. I will certainly remember the effective and open discussions, the many victories and few defeats in various sports competitions, many great hikes and conferences, good jokes, pleasant lab and office time, as well as all the fun during meals, group meetings, cakes and apéros.

I would also like to mention the stimulating and successful collaborations, especially within the QSIT initiative and with many theorists, in particular Lorenzo De Leo, Corinna Kollath, Antoine Georges, Vito Scarola, Lode Pollet,

Evgeni Burovski, Evgeny Kozik, Matthias Troyer, Rajdeep Sensarma, David Pekker, Ehud Altman, Eugene Demler, Sebastian Huber, Fabian Hassler, Andreas Rüegg, Hans-Peter Büchler, Gianni Blatter, and Thierry Giamarchi.

A final thanks goes to all my family and especially my parents, who supported me throughout my studies and Ph. D. work.

# Robert Jördens — curriculum vitae

## Personal

Born December 8, 1981  
German citizen  
ETH Zürich, HPF D23  
8093 Zürich, Switzerland  
Phone: +41 44 63 37543, +41 76 4680783  
E-mail: jordens@phys.ethz.ch

## Education

1988 – 1992 Primary school: Schlossbachschule Röttgen, Bonn, Germany  
1992 – 2001 High school: Collegium Josephinum, Bonn, Germany  
2001 – 2003 Undergraduate studies in Physics: ETH Zürich, Switzerland  
2003 – 2004 ERASMUS scholarship: Universidad Complutense de Madrid, Spain  
2004 – 2006 Graduate studies in Physics: ETH Zürich  
2006 – 2006 Diploma thesis under the supervision of Prof. Dr. T. Esslinger:  
*A Radio Frequency Source for the Preparation of Quantum States.* ETH Zürich  
2006 – 2010 Ph.D. thesis under the supervision of Prof. Dr. T. Esslinger:  
*Metallic and Mott-insulating phases in fermionic quantum gases.* ETH Zürich

## Publications

1. *Interaction-Controlled Transport of an Ultracold Fermi Gas.* N. Strohmaier, Y. Takasu, K. Günter, R. Jördens, M. Köhl, H. Moritz, and T. Esslinger. *Phys. Rev. Lett.*, **99**, 220601 (2007)
2. *A Mott insulator of fermionic atoms in an optical lattice.* R. Jördens, N. Strohmaier, K. Günter, H. Moritz, and T. Esslinger. *Nature (London)*, **455**, 204 (2008)
3. *Observation of Elastic Doublon Decay in the Fermi-Hubbard Model.* N. Strohmaier, D. Greif, R. Jördens, L. Tarruell, H. Moritz, T. Esslinger, R. Sensarma, D. Pekker, E. Altman, and E. Demler. *Phys. Rev. Lett.*, **104**, 080401 (2010)
4. *Quantitative Determination of Temperature in the Approach to Magnetic Order of Ultracold Fermions in an Optical Lattice.* R. Jördens, L. Tarruell, D. Greif, T. Uehlinger, N. Strohmaier, H. Moritz, T. Esslinger, L. De Leo,

- C. Kollath, A. Georges, V. Scarola, L. Pollet, E. Burovski, E. Kozik, and M. Troyer. *Phys. Rev. Lett.*, **104**, 180401 (2010)
5. *Lifetime of double occupancies in the Fermi-Hubbard model.* R. Sensarma, D. Pekker, E. Altman, E. Demler, N. Strohmaier, D. Greif, R. Jördens, L. Tarruell, H. Moritz, and T. Esslinger. *ArXiv e-prints* (2010). 1001.3881

### *Invited conference talks*

1. International Conference on Quantum Engineering, Monte Verità, Switzerland, 2009.
2. Quantum Science and Technology (QSIT) Meeting, Arosa, Switzerland, 2010.

### *Invited seminar talks*

1. optETH Doctoral Student Symposium, Zürich, Switzerland, 2008
2. Max-Planck-Institut für Quantenoptik, Quantum Many Body Systems Division Group Seminar, Munich, Germany, 2010.
3. AMP Colloquium, Zürich, Switzerland, 2010
4. University of Cambridge AMOP Seminar, Cambridge, United Kingdom, 2010
5. National University of Singapore CQT Seminar, Singapore, 2010
6. University of Kyoto Quantum Optics Seminar, Kyoto, Japan, 2010
7. University of Tokyo AMO Seminar, Tokyo, Japan, 2010
8. JILA Seminar, University of Colorado, Boulder, CO, US, 2010
9. NIST Ion Storage Seminar, Boulder, CO, US, 2010
10. Special JQI Seminar, University of Maryland, College Park, MD, US, 2010